2020•2021

Faculteit Industriële ingenieurswetenschappen

master in de industriële wetenschappen: nucleaire technologie

Masterthesis

Aerosol formation from liquid impingement in liquid metal cooled nuclear reactor systems

PROMOTOR :

Prof. dr. Sonja SCHREURS

PROMOTOR :

Dr. Kris ROSSEEL

COPROMOTOR :

ir. ing. Christophe CORAZZA

Kirsten Weygers

Scriptie ingediend tot het behalen van de graad van master in de industriële wetenschappen: nucleaire technologie, afstudeerrichting milieu

Confidentieel

Gezamenlijke opleiding UHasselt en KU Leuven

2020•2021

Faculteit Industriële ingenieurswetenschappen

master in de industriële wetenschappen: nucleaire technologie

Masterthesis

Aerosol formation from liquid impingement in liquid metal cooled nuclear reactor systems

PROMOTOR :

Prof. dr. Sonja SCHREURS

PROMOTOR :

Dr. Kris ROSSEEL

COPROMOTOR :

ir. ing. Christophe CORAZZA

Kirsten Weygers

Scriptie ingediend tot het behalen van de graad van master in de industriële wetenschappen: nucleaire technologie, afstudeerrichting milieu

Confidentieel

UHASSELT

KU LEUVEN

Acknowledgements

During the period I spent working on my master thesis research, I could rely on the help of some people I would like to express my gratitude to.

First of all, I wish to express my sincere appreciation to my internal promotor prof. dr. Sonja Schreurs for the guidance. Thanks to your effort, professional tips and insightful feedback, I was able to complete this research thesis within the given time frame. Whenever I had a question, you always made time to video-call, which I really appreciated.

I would also like to thank my promotors dr. Kris Rosseel and ir. ing. Christophe Corazza for the learning opportunities and for all the effort. Not one questions asked was a question too many. Your immense experience has encouraged me to perform the thesis research and to attempt to unravel the causes of the technical difficulties.

Furthermore, I would like to thank Yunus Aksoy for lending the high-speed camera and for helping with the recordings.

At last, I would like to thank family and friend and in particular my parents and my boyfriend Ruben to encourage and support me through this final part of my master.

Table of contents

List of tables

List of Figures

List of symbols and abbreviations

Symbol	Unit	Description
a	m/s^2	Acceleration
A	m^2	Area
F_b	N	Buoyant force
ρ	kg/m^3	Density
d	m	Diameter
C_d	Dimensionless	Drag coefficient
η	Pa·s	Dynamic viscosity
F_z	N	Gravity force
ϲ	s	Impact time
v	m/s	Impact velocity
l	m	Length
r	m	Radius
Re	Dimensionless	Reynolds number
σ	N/m	Surface tension
We	Dimensionless	Weber number

Abbreviation	Description
ADS	Accelerator driven system
BR1	Belgian reactor 1
BWR	Boiling water reactor
CMOS	Complementary metal-oxide semiconductor
CPC	Condensation particle counter
DMA	Differential mobility analyzer
fps	Frames per second
FT	Falling time
LBE	Lead bismuth eutectic
LWR	Light water reactor
MDC	Micro dispensing controller
MFC	Multi functional controller
MYRRHA	Multi-purpose hYbrid Research Reactor
NL	Needle lfit
OPC	Optical particle counter
OT	Open time
PM	Particle matter
PSD	Particle size distribution
RT	Rising time
SFR	Sodium fast reactor
SMPS	Scanning mobility particle sizer

Abstract

Lead-bismuth eutectic (LBE) is chosen as coolant for the future MYRRHA reactor. Aerosols formed in nuclear reactors during operations can jeopardize human health and plant operations in case of accidents. Aerosol models are available for water, - and sodium based reactors, but not for LBE. Therefore, this thesis presents a pilot study on the most important aerosol formation mechanism in MYRRHA: impingement of LBE droplets on surfaces.

A 'SPLAT setup' is built in which LBE droplets are dispensed and impinge on liquid and solid surfaces. Impingement is characterized with a high-speed camera; the resulting aerosol particle size distribution (PSD) was determined with a wide range aerosol detector. Liquid impingement is studied for large (Ø: 1.5 – 3 mm) and small droplets (Ø < 1.5 mm) with velocities between 1.82 – 2.53 m/s. Recordings of the liquid surface show splashing, which increases with increasing droplet diameter and impact velocity. Dry solid surface impingement shows droplet spreading. Successive LBE droplets (Ø: 2.90 ± 0.02 mm), impacting a liquid surface generate aerosol particles with diameters < 250 nm. The PSD maximum is located at 100 nm. On a dry solid surface, diameters up to 100 nm are recorded, with the PSD peak at 28 nm.

The results of this thesis show that liquid impingement of LBE droplets can pose a safety hazard as significant amounts of sub µm aerosol particles are generated. While most splashing is observed with the liquid surface, dry solid surface impingement generates the smallest aerosols.

Abstract in Dutch

Lood bismut eutecticum (LBE) is gekozen als koelmiddel voor de toekomstige MYRRHA reactor. Aerosols die tijdens de exploitatie van de reactor gevormd worden, kunnen de menselijke gezondheid en de werking van de reactor bedreigen. Voor water,- en natrium reactoren zijn aerosolmodellen beschikbaar, maar niet voor LBE. Daarom omvat deze thesis een pilootstudie naar een van de belangrijkste aerosol bronnen in MYRRHA: inslag van LBE druppels op een oppervlak.

In de SPLAT setup worden LBE druppels gevormd die inslaan op een vast of vloeibaar oppervlak. De druppelinslag werd bestudeerd met een hogesnelheidscamera en de gevormde aerosol deeltjesverdeling (PSD) met een breed bereik aerosol detector. De inslag werd bestudeerd voor grote (Ø: 1.5 – 3 mm) en kleine LBE druppels (Ø < 1.5 mm) met snelheden tussen 1.82 – 2.53 m/s. Opnames van het vloeibaar oppervlak tonen toenemende spatvorming met toenemende druppelgrootte en valsnelheid. Inslag op een vast oppervlak resulteert in uitspreiding van de druppel. Impact van opeenvolgende druppels (Ø: 2.90 mm) op een vloeibaar oppervlak vormt aerosolen met diameter < 250 nm, met de PSD piek bij 100 nm. Impact op een vast oppervlak genereert deeltjes tot 100 nm diameter, met de PSD piek bij 28 nm.

De resultaten van deze thesis tonen aan dat de inslag van LBE druppels op een oppervlak een veiligheidsrisico kan omvatten wegens de vorming van substantiële hoeveelheden van sub µm aerosoldeeltjes. Terwijl ‘spatten’ voornamelijk werd waargenomen tijdens de inslag op een vloeibaar oppervlak, genereert de inslag op een vast oppervlak de kleinste aerosols.

1 INTRODUCTION

1.1 Context

SCK CEN is the Belgian nuclear research center situated in Mol. It is a global leader in the field of nuclear research, services and education. SCK CEN focuses on different topics in nuclear physics, namely: medical and industrial applications of radiation; nuclear safety and radiation protection; nuclear decommissioning and nuclear reprocessing [1].

This master thesis is performed in the Chemistry and Conditioning Program (CCP) unit of the Advanced Nuclear Safety (ANS) institute of SCK CEN. The topic 'Aerosol formation from liquid impingement in liquid metal cooled nuclear reactor systems' is part of the MYRRHA project.

MYRRHA stands for Multi-purpose hYbrid Research Reactor for High-tech Applications. It is a novel type of fast nuclear research reactor which is scheduled to start operating in 2036 at SCK CEN in Mol, Belgium. MYRRHA is a unique reactor in that it consists of a high-energy – high-current proton accelerator coupled to a sub-critical core, which is cooled with a liquid metal coolant. The high-energy protons generate fast neutrons through spallation of the coolant to sustain the nuclear chain reaction in the core. Unlike classical reactors, the reactor core is not cooled with water but with a liquid metal mixture of lead and bismuth named lead-bismuth eutectic (LBE) [1]–[3]. Despite the advantages of this cooling agent, some drawbacks remain. One of these drawbacks is the formation of aerosols by the LBE coolant in MYRRHA.

Before finishing the construction of MYRRHA, SCK CEN wants to identify the LBE aerosol source terms that could occur in the reactor. The formation and subsequent behavior of these aerosol particles need to be evaluated, as plant operations and public health may be affected by their presence inside the reactor. This study characterizes one of the most important LBE aerosol source term mechanisms in future lead-bismuth cooled reactor systems as MYRRHA; LBE aerosol formation by liquid impingement [2], [3].

1.2 Problem statement

LBE will be chosen as one of the possible coolants for future gen IV nuclear systems. This LBE coolant, which will be used in MYRRHA, can cause formation of aerosols during reactor operation. Aerosols and more specifically LBE-aerosols entail harmful effects on human health due to their characteristics. On top of health effects, LBE aerosols jeopardize plant operations. The risks related to LBE aerosols are further explained in chapter 2.4.

Experience using LBE in experimental installations at SCK CEN has shown that LBE aerosols are formed when gas interacts with LBE (called 'entrainment') during operation of the installation. LBE aerosol particle deposition was observed on valves, filters and openings, illustrated in Figure 1 [4], [5].

Figure 1: Presence of LBE aerosol particles in an experimental installation at the SCK CEN which uses LBE. From left to right: deposition on viewports, on filters, and in piping systems.

Aerosols have been studied extensively in water based nuclear systems. Modelling tools for assessing the impact of aerosols in various accident scenarios are available [2], [6]. Also for Sodium reactors reports, data and modelling tools are available [7]. But for LBE, quasi nothing regarding aerosols exists as these aerosol formation mechanisms, aerosol behavior and splashing forms characteristics have not yet been investigated [4].

Therefore, SCK CEN started a research program to study the formation and dynamic behavior of LBE aerosols. The aim is to obtain the relevant aerosol source terms that can be used to assess the risks related to radioactive release of these particles, for example during leakages or nuclear accidents. This is important to perform a hazard analysis for employees and public health under accident conditions involving LBE related aerosols and will allow modifying the reactor's design to mitigate these hazards if needed [5].

In light water reactors (LWR) and Sodium Fast reactors (SFR) aerosols can be formed along various pathways, such as coolant evaporation, fission gas release under accident conditions, chemical reactions (e.g. reaction of sodium with air) and formation of aerosols due to interactions of solids or gasses with the coolant. Coolant evaporation and fission product release will only occur under accident conditions and will not be considered here. Under normal operation conditions, 5 types of aerosol generation mechanisms are identified in LWR and SFR systems, referred to as 'entrainment source terms'. Namely liquid impingement, bubble burst, wave undercut, roll wave and bulge disintegration [2], [3]. These 5 aerosol formation mechanisms are also expected to occur when using LBE as coolant in MYRRHA.

From a confidential safety study performed at SCK CEN, one of the most important LBE aerosol source term mechanisms for MYRRHA was identified to be liquid coolant impingement. This thesis will therefore focus on this mechanism, namely: on characterizing liquid impingement of impacting LBE droplets on different surfaces under conditions expected as in MYRRHA and on characterizing the resulting aerosol particle size distribution.

The study is unique in that the results will be the first obtained on LBE liquid impingement within the framework of LBE aerosol formation. The results and conclusions obtained in this thesis work will be used as a starting point for further studies regarding the LBE aerosol's dynamic behavior inside MYRRHA. This will aid in assessing the impact and risks of LBE aerosols for plant operation and for employees and public health during accidents in MYRRHA.

This work is subdivided into 6 chapters. Chapter 2 discusses and compares the MYRRHA reactor with existing reactor designs. Furthermore, the advantages and disadvantages of LBE as cooling agent and the aerosol formation mechanisms are discussed. This theoretical chapter is followed by the description of the design of the SPLAT setup in chapter 3. Chapter 4 provides information about the applied methods and materials in the ex-situ and in-situ experiments. The results of the generated droplets with the dispenser, the appeared technical difficulties, the results of the high-speed camera experiments and the aerosol particle size distributions are discussed in chapter 5. Finally, the thesis ends with the drawn conclusions.

2 THEORETICAL BACKGROUND

This chapter starts with an overview of the generations of nuclear reactors to frame the MYRRHA project. Hereafter, the MYRRHA reactor and the role of LBE within MYRRHA are explained in section 2.2 and 2.3. The next section discusses the drawbacks of using LBE. Section 2.5 explains aerosol formation and splashing. In the last section of chapter 2, the relevant parameters within the framework of liquid impingement are addressed.

2.1 Nuclear reactor generations

Nuclear reactor designs are categorized by 'generations'; generation I, II, III, III+, IV, illustrated in Figure 2. The generations differ mainly in cost-effectiveness, safety, security, nonproliferation features, grid appropriateness, licensability, and management of the fuel cycle [8].

The first man-made nuclear reactor was the Chicago Pile 1, built by Enrico Fermi in 1942 as part of the Manhattan program. The reactor consisted of 40 ton natural uranium and 385 ton graphite as moderator. The core was not cooled, nor was there a containment. Generation I reactors, built in the early 50's, were the first to produce civilian nuclear power. They are referred to as 'early prototypic reactors'. A prime example is the BR1 reactor at the SCK CEN which started operating in 1956. Generation II reactors are also known as commercial reactors, designed to increase safety and decrease risks associated with accidents. Examples are the pressurized water reactors (PWR) and boiling water reactors (BWR); both types are referred to as light water reactors (LWR). Generation II reactors use active safety features involving electrical or mechanical operations that can be initiated by the reactor's operators. The first commercial and generation II reactor built in Belgium was the BR3 reactor at SCK CEN in Mol. BR3 started operating in 1962 and was shut down in 1987. It is currently used as pilot project to achieve information about dismantling [9]. To advance safety, a new generation of advanced light-water generation III reactors were conceived. These generation III designs incorporate passive safety systems into the reactor structure. Additionally, generation III+ reactor offer significant improvements in safety certified by NRC 1990 [8]. MYRRHA belongs to the generation IV nuclear reactor designs, which are required to be highly economical, to provide elevated safety, to produce minimal waste and to be proliferation resistant [10].

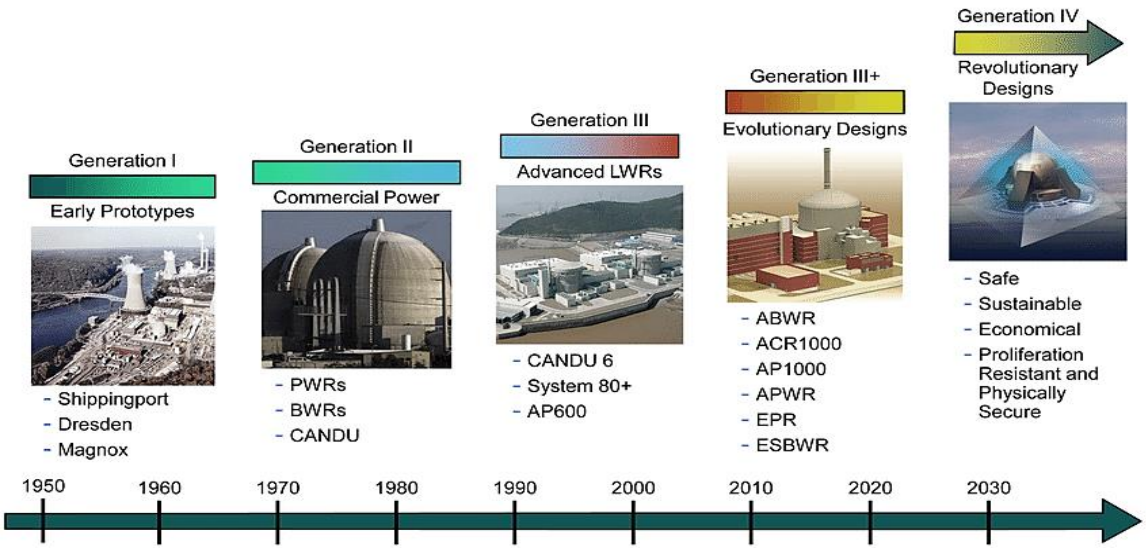

Figure 2: Nuclear reactor generations [10].

The generation IV forum identifies 6 'next generation' reactor concepts: gas(-cooled) fast reactors (GFS), lead(-cooled) fast reactors (LFR), molten salt reactor (MSR), sodium(-cooled) fast reactor (SFR), supercritical water(-cooled) reactor (SCWR) and very high temperature reactor (VHTR) [10].

2.2 The MYRRHA reactor

The Belgian Federal Government gave in 2018 approval for the MYRRHA project, to be built at the SCK CEN site in Mol. MYRRHA is a novel research reactor that will be used for the study of new nuclear fuel, the production of medical radioisotopes, fundamental physics research and research on nuclear waste and fusion. It will replace the current BR2 reactor, which is situated at the nuclear site of the SCK CEN since 1962. BR2 has a capacity of 125 MW and is mainly used for the production of medical radioisotopes for diagnostics, cancer therapy and neutron trans-mutation doped silicon for industrial purposes and material research [11], [12].

MYRRHA distinguishes itself from other classical reactors as it is the first full scale implementation of an Accelerator Driven System (ADS). In this concept, a sub-critical core is coupled to a high-power accelerator that acts as an external neutron source. The core of the MYRRHA reactor is designed to be sub-critical, and as such it does not contain enough fissile material to maintain the neutron chain reactions. Hence, the reactor core must continuously be fed by neutrons which are generated by bombarding a liquid metal spallation target with a high-current (~mA) of high-energy (600 MeV) protons, delivered by the accelerator. This results in the generation of high-energy neutrons through a nuclear spallation reaction that will sustain the fission chain reaction [8], [12], [13].

A second novelty is that the reactor is cooled by a low moderating liquid metal coolant (LBE), which also acts as the spallation target. Due to the high-energy spectrum of the neutrons produced by spallation, MYRRHA's design is referred to as 'fast' reactor. This fast reactor design does not require a moderator but requires fuel rich in fissile material [8], [12], [13]. The LBE coolant only operates as spallation target in the reactor's subcritical regime. MYRRHA can also work with a critical core, without accelerator [11], [14].

These novelties provide many benefits. For instance, the use of the accelerator will allow transmutation of long-lived actinides, thereby considerably reducing the volume and lifetime of the reactor's radioactive waste. A second advantage of the accelerator is that the nuclear core reactions are safe to control: if the accelerator is turned off, the chain reaction stops [11], [12].

MYRRHA will be constructed in 3 phases. The construction of the particle accelerator started in 2018 and should be finished in 2026. SCK CEN is planning to start building the reactor itself in 2026; the reactor in combination with the particle accelerator will then start operating in 2036 [12].

2.3 Lead-bismuth eutectic as cooling agent in MYRRHA

MYRRHA's cooling agent is Lead-Bismuth eutectic. An eutectic signifies a homogeneous mixture that melts at a single temperature that is lower than the melting temperatures of the constituents. The melting temperatures of pure lead and pure bismuth are 600.6 K and 544.4 K, while LBE melts at 397.7 K [2]. Due to this low melting temperature, LBE is favorable for many ADS-systems as it allows to decrease the operational temperatures, which results in lower corrosion rates of structural steels and facilitates maintenance. Besides its low melting temperature, LBE has –in comparison to other cooling agents such as Sodium, – significantly higher boiling temperatures ($T_{b\ LBE}$ 1944.15 K). This means that the reactor can operate under normal pressure conditions without the risk of over pressure due to coolant boiling. Furthermore, because of the high density ($\rho_{\ LBE\ 413.15\ K}$ 10,548 kg/m^3), high cooling capacities can be reached in a compact volume.

LBE consists of 44.5 % lead and 55.5 % bismuth. Heavy elements such as lead and bismuth have a low moderation ($\sigma_{abs\ LBE} = 0.0014$ barn) with the result that the neutrons are not thermalized but retain a significant energy, sufficient to facilitate fission of otherwise non-fissile elements [4]. Furthermore, LBE does not show the violent reaction with water and oxygen or air as Sodium does. Moreover, lead and bismuth are also excellent radiation shields, blocking gamma radiation. Due to these reasons, LBE is a suitable candidate as coolant in fast reactors such as MYRRHA. Besides the use of LBE as a coolant, LBE is also used for neutron generation as it acts as spallation target in the accelerator [4].

2.4 Drawbacks of LBE for MYRRHA

Despite the advantages of LBE as coolant, disadvantages remain, such as corrosion of structural materials, formation of oxides and the creation of aerosols. In addition, the use of LBE poses risks to human health.

2.4.1 OXIDE FORMATION

During normal operation, a major contamination source for an ADS will be **hydrogen** from the accelerator and impurities coming from corrosion of structural steels or from spallation reactions in the target (LBE). **Spallation reactions** create a whole plethora of radioactive isotopes, ranging over almost the whole periodic system and thereby leading to activation of the coolant. Besides their radiological hazards, these impurities can also react with dissolved oxygen and therefore pose a problem for long term operation with regards to e.g. pipe clogging [4].

Corrosion and oxide formation from other impurities are also issues that need to be tackled. Both are connected with the solubility of most elements in LBE, including steel alloying elements (such as Fe, Ni, Cr) and oxygen [4]. Dissolution of steel alloying elements in LBE may lead to local changes in structure and properties of structural materials, which may result in reduced performance or malfunctioning of reactor components. This would result in more repair work leading to increased shut-down periods [8]. A further issue is oxide formation when LBE comes into contact with air or oxygen containing gas [15], as oxygen readily dissolves in LBE. During any restart, maintenance or repair, oxygen will be the largest contamination source for lead alloy systems. When oxygen dissolves in LBE, it will react with dissolved impurities to form stable oxides or stay in LBE as dissolved oxygen. This process can continue until the oxygen solubility limit is reached and the coolant itself starts to oxidize, causing lead monoxide (PbO) to precipitate. As the formed oxides are solid in the temperature range foreseen in MYRRHA, they are difficult to remove.

Corrosion is being tackled by lowering the operational temperatures and the development of corrosion resistant alloys or coatings. Beside the use of inert cover gas to minimize oxygen dissolution, active oxygen control methods are being researched and implemented to mitigate the effects of oxide formation or coolant oxidation (at too high dissolved oxygen contents) and steel corrosion (at too low dissolved oxygen contents) by adjusting the dissolved oxygen content [4].

2.4.2 AEROSOL FORMATION

A less familiar drawback may be the formation of **LBE aerosols**, further discussed in the next section 2.5. LBE aerosols will be formed inside the MYRRHA reactor wherever a gas flow comes in contact with a liquid (e.g. LBE) or solid (e.g. deposits) or due to nucleation and growth of particles from an oversaturated LBE vapor. Due to the various formation mechanisms involved, aerosol particle sizes ranging from about 50 nm (freshly formed nuclei) to well over 100 µm (due to entrainment or coagulation) are expected [4]. On top of the effects of corrosion and oxides, the aerosol particles also jeopardize plant operations since they can form deposits, as shown in Figure 1, and potentially block critical orifices [3].

Furthermore, the lead and bismuth nuclides present in the radioactive coolant pose potential radiological risks. Bismuth has a low toxicity to humans but forms the alpha emitting Polonium-210 by beta decay [5], [6], [11], shown in decay formula 1 below.

$$^{210}_{83}Bi \rightarrow {}^{210}_{84}Po + {}^{0}_{-1}\beta \quad (1)$$

Additionally, due to the spallation reaction of the coolant, many other radioactive isotopes are formed inside the LBE pool. The formed LBE aerosols could therefore act as carriers of hazardous radionuclides, such as polonium. If radioactive material can escape from a nuclear reactor during accidents or leakages it shall do this in the form of aerosols. Thus, LBE aerosols could be potential source terms for release of lead, polonium-210 or other radioactive elements to the environment.

Besides the disadvantages for the nuclear reactor, the aerosol particles entail health effects for the human body. The particles have small dimensions and are therefore able to penetrate deep into the human body [4]. Particles with a diameter of 10 microns or less, ($\leq PM_{10}$) can penetrate and deposit deep inside the lungs. The even more health-damaging particles are those with a diameter of 2.5 microns or less, ($\leq PM_{2.5}$). $PM_{2.5}$ can penetrate the lung barrier and enter the blood system. Chronic exposure to particles contributes to the risk of developing cardiovascular and respiratory diseases, as well as of lung cancer [16].

Moreover, the lead-containing aerosols entail a significant risk of lead poisoning [7], [8]. Heavy metal poisoning is the accumulation of heavy metals in toxic amounts in the soft tissues of the body. Lead can enter the human body through inhalation, ingestion or absorption. The heavy metal is distributed to the brain, liver, kidney and bones. Lead poisoning occurs when lead builds up in the body. The symptoms differ depending on the amount and where the buildup occurs and vary depending on the age of the individual. Overexposure to lead may cause high blood pressure, kidney diseases, anemia, brain damage and damage to reproductive organs. Other symptoms include fever, headaches, fatigue, vomiting, incoordination, hallucinations, seizures and altered consciousness [4], [11].

2.5 Aerosol formation from liquid impingement

2.5.1 LBE AEROSOL SOURCE TERMS

LBE aerosols are already proven to be present in experimental reactors as could be deduced from Figure 1. Concerning the discussed risks related to LBE aerosols in previous section 2.4, it is necessary –from a safety point of view– to analyze the formation and transportation characteristics of these liquid metal aerosols formed in MYRRHA.

Aerosols can be formed in nuclear reactors during normal operations due to interactions of solids or gasses with the coolant or under accident conditions because of e.g. coolant evaporation, fission gas release or chemical reactions. This thesis focuses on aerosol formation under normal operating conditions. The mechanism of interest is aerosol formation due interaction of the coolant with the gas flowing through the reactor cover gas space.

Aerosols are created when the liquid phase is entrained in the gas phase. This takes place on the gas-liquid interface and is influenced by the exchange of mass, momentum and energy between the liquid film and the gas stream [18]. The state-of-the-art report on nuclear aerosols (2009) written by the Nuclear Energy Agency and the Committee on the Safety of Nuclear Installations indicates that in light water reactors (LWR) and Sodium fast reactors (SFR) 5 types of gas entrainment mechanisms, referred to as ‘source terms’ occur under normal operations. Figure 3 illustrates these entrainment source terms, namely: liquid impingement, bubble burst, wave undercut, roll wave and bulge disintegration [2], [3]. Similar aerosol generation mechanisms can be expected for MYRRHA under normal operation.

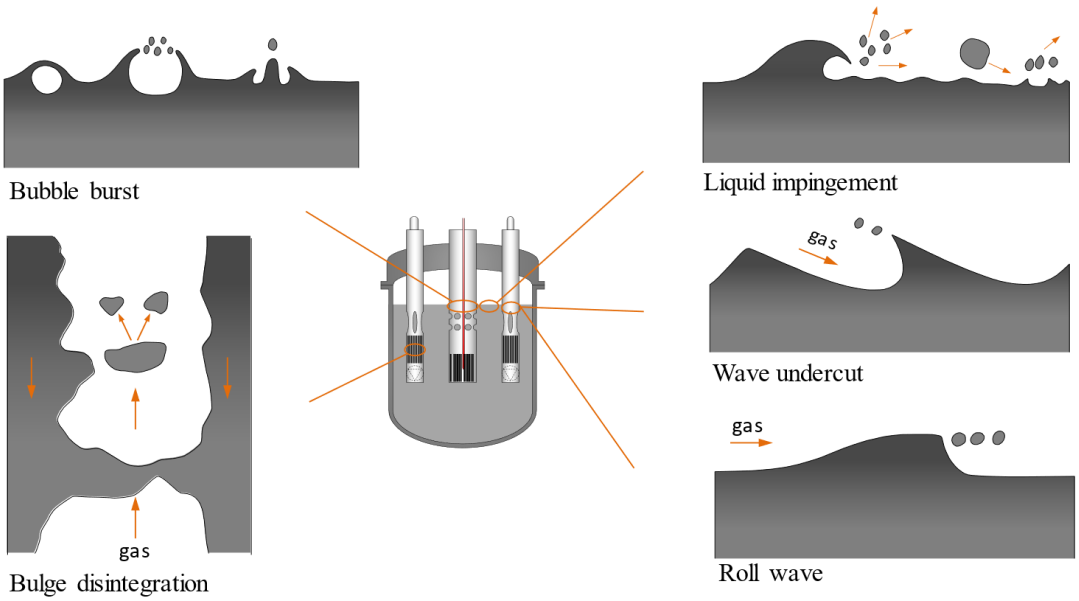

Figure 3 Entrainment source term mechanisms in LWR and SFR [19].

Liquid impingement occurs when a liquid droplet collides on a liquid, wet solid or dry solid surface. Due to splashing, the droplet breaks up after the collision with the surface. Secondary droplets are formed and ejected and may be entrained in the gas phase above the surface.

Bubble burst occurs at the liquid surface of a coolant pool when bubbles injected into the liquid rise to the surface and collapse. Bubbles can be generated by gas injection into the liquid pool for example during gas bubbling for oxygen conditioning or when fission gas is released from fuel elements under accident conditions. Bubbles will rise from the pool to the surface and secondary droplets generated from the burst create aerosols above the liquid pool [20].

Under certain conditions i.e., near pumping systems, extreme deformation on the gas-liquid interface can occur, resulting in the formation of waves, which can break up into several liquid droplets. **Wave undercut** and **roll wave** source terms are examples of this phenomenon, occurring near pumps creating turbulence [18]. **Bulge disintegration** occurs when large volumes of gas travel upwards surrounded by a 'wall' liquid. Because of the motion between the downwards moving liquid and the rising gas, droplets are created and dragged upwards.

A confidential safety study performed at SCK CEN identified the various source terms relevant for MYRRHA. Of these, the most important LBE aerosol source term mechanisms for MYRRHA deemed to be liquid coolant impingement. This thesis will therefore focus on this mechanism and more specifically on characterizing liquid impingement of impacting LBE droplets on different surfaces under conditions expected as in MYRRHA and determine the resulting aerosol particle size distribution.

2.5.2 SPLASHING

Splashing provokes aerosol formation when droplets impact on a surface (liquid impingement). When a leak would occur in pipes containing LBE, droplets would be created whose form and size will depend on the size and shape of the leak and of the LBE pressure at the leak. High pressure leaks can lead to a spray of LBE droplets, resulting in µl-droplets. Another possible event to happen is when fuel rods are taken out of the LBE pool in MYRRHA. During this event, large LBE droplets will splash back into the LBE pool from the dripping fuel rod.

For these reasons, the surfaces to analyze are determined to be a liquid surface and a dry solid surface. Splashing on both surfaces is elaborated in following paragraphs. This study also specifically analyses two impinging droplet types; small, sub-mm droplets and large droplets, with a diameter of order of millimeters, to cater for the expected droplet sizes in MYRRHA.

There are several possible splashing outcomes when a droplet impinges on a surface. Examples are prompt splash, crown splash, receding breakup, rebound, partial rebound of deposition [21]. Only prompt and crown splash are considered in this study as they are the only ones that create aerosols, as illustrated in Figure 4 [21]. During prompt splash, a drop breakup occurs immediately after impact as the liquid droplet spreads out over the surface. Droplets are directly released from the breakup of the tip of the advancing spread-out liquid film, also called the lamella. During crown splash, the lamella deforms and rises from the surface, forming a high crown-like structure which breaks up into fine droplets [22].

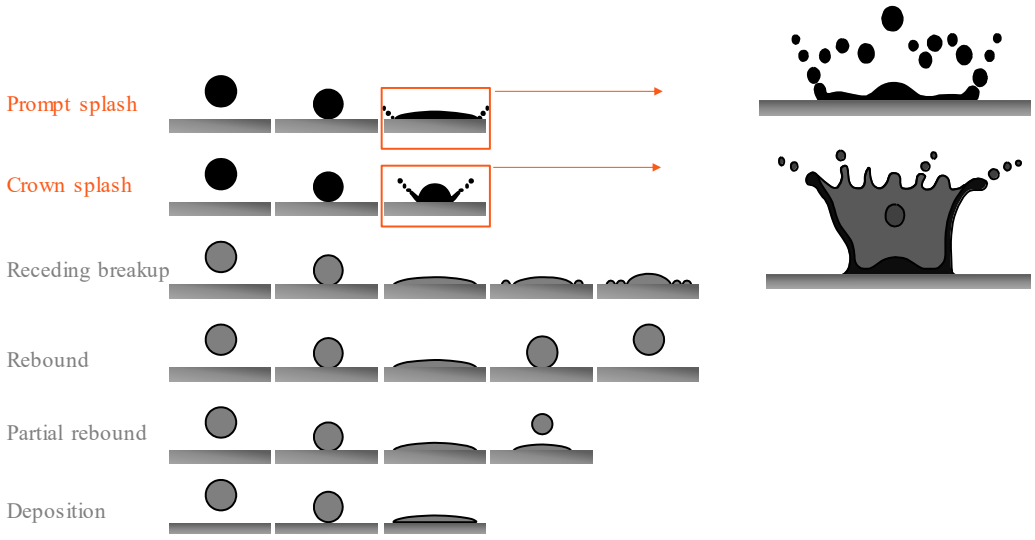

Figure 4: Splashing forms due to liquid impingement.

Impingement and splashing forms have been researched for a whole plethora of liquids. The findings and outcomes are summed in the following sections, since they are also expected to occur with LBE.

2.5.2.1 Affecting parameters

From Figure 4, it can be derived that the 2 splashing phenomena (prompt and crown splash) create secondary droplets and thus lead to the generation of aerosols. Whether a droplet will splash, spread or rebound depends on properties of the droplet, the surface and the fluid through which the droplet moves [23].

For example, the shape of a droplet will be determined by liquid properties, by the initial conditions upon release and the interaction of the droplet with its surroundings. While most calculations within the framework of aerosol formation assume a spherical falling droplet, the shape can vary widely from spherical to deformed to oscillating. The shape of a droplet moving through a fluid can change due to aerodynamic forces and oscillations. The latter can be caused by friction between the droplet surface and the surrounding fluid [23]. Furthermore, the droplet diameter is known to have major impact on impingement outcomes. Larger drops will generate higher impact energy and thus yield splashing. Moreover, droplet surface tension, density and viscosity also need to be considered.

The impacting surface can be a liquid, a wet solid surface or a dry solid surface. Liquid surfaces are assumed to be deep compared to the impacting droplet's size, i.e. the depth of the pool is an order of magnitude larger than the droplet's size. In this case, the bottom nor the walls of the tank influence the liquid, in contrast with a wet solid surface, which consist of a thin layer of liquid. For dry solid surfaces, roughness and elasticity are important parameters to determine the behavior of the impacting droplet. In this work, a polished smooth dry solid surface is used. Next to the surface type, the elasticity of the surface could affect the impingement outcomes [23], [24]. Lastly, the temperature of the solid surface can cause different splashing outcomes, as in case of e.g. a cold solid surface, the droplet may solidify upon impact.

Furthermore, the surrounding fluid affects droplet impacting. Dry solid surface impingement is mostly expected to generate a spreading droplet instead of a splashing droplet, further discussed in 2.5.2.2. However, Xu Lei et al (2005) wondered how it is possible to observe splashing on a dry smooth surface. As the liquid momentum at the surface points horizontally outwards and as there is no layer of fluid to push against, then how does the expanding liquid layer gain a momentum in the vertical direction? In their experiments with ethanol, they proved that the presence of a surrounding gas is essential for a crown splash to occur on a dry smooth surface. It was observed that reducing the air pressure could reduce the crown splash completely. In e.g. industrial applications of surface coatings, a vacuum atmosphere or a gas with a low molecular weight is used to control splashing [29]. In our case, this parameter is not considered, as we will be working in an inert gas atmosphere of ambient pressure.

2.5.2.2 Dry solid surface impingement

Liquid impingement with a dry solid surface is expected to result in droplet bouncing, spreading or splashing, as illustrated in Figure 5 [23], with spreading expected to be the dominant mechanism.

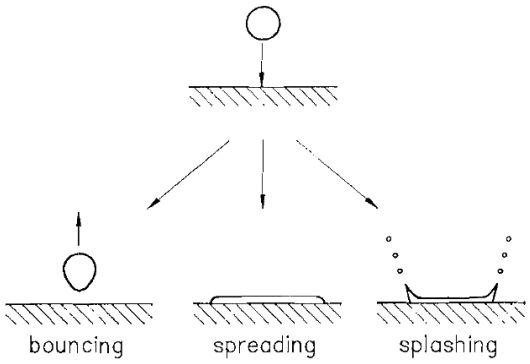

Figure 5: Impact of a droplet on a solid surface: bouncing, spreading, splashing [23].

During the impact of a droplet with a solid surface, a contact zone with a certain radius will be formed on the surface by the contact between the lower part of the droplet and the upper part of the surface. The liquid spreads out over the solid surface. The smooth movement of the liquid over the surface results in the formation of a thin disc-shaped liquid film bordered by a thicker rim [25]. The disc shaped spread-out is called a lamella. Figure 6 shows an actual spread out LBE droplet on a dry solid surface. Around the lamella, ejected secondary droplets can be observed.

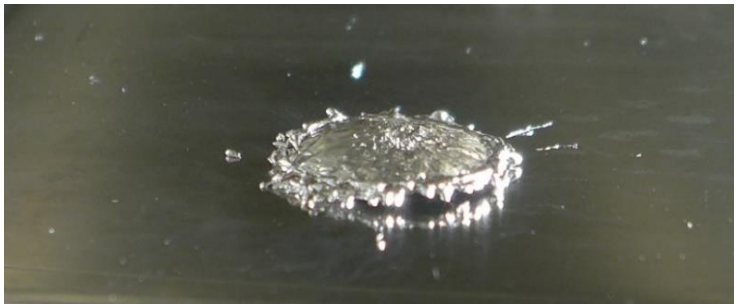

Figure 6: lamella on a dry solid surface.

The lamella reaches its maximum radius when the kinetic energy is transformed to surface energy. Afterwards, the lamella is known to shrink due to capillary forces and to expand due to kinetic energy [26]. The amount of contractions and expansions depends on the impact energy [27]. Eventually the droplet reaches an equilibrium shape.

In some instances, the recoil of the lamella can make the liquid film separate from the surface, i.e. “lift-off”. At high impact energies, the lift-off motion can cause splashing because droplets break apart from the lamella. The lamella of viscous liquids is in several previous studies observed to lift away from the surface, ‘gliding’ on a sheet of air. Instead of the whole lamella lifting off the surface, it is also possible that only the tip of the lamella rises.

This phenomenon is defined by viscosity and air pressure, according to Thoroddsen et al (2010) [22]. But, recent theories still have not found the exact mechanisms behind the lamella lift-off. During impingement on rough surfaces, it is stated that a droplet impacting a solid surface entraps an air bubble under its center under atmospheric conditions. When the droplet makes contact with the surface, the air exits from underneath the spreading droplet by creating a thin air film. The lift-off is in this case explained by 'the floating of the lamella on the thin air layer' [22].

As can be deduced from Figure 6, disturbances can be seen at the rim of the lamella, called 'fingers' or 'radial arms'. At high impact velocities, these fingers break up into droplets and hereby converting spreading into splashing [23]. The finger-pattern itself depends on the surface properties as the wettability of the surface and the texture [22].

2.5.2.3 Liquid surface impingement

Liquid impingement of a droplet with a liquid surface is mostly expected to generate splashing, but could also result in spreading. During spreading, the droplet disappears in the liquid pool with practically no secondary droplet formation.

In the case of splashing, the liquid surface is disturbed [22]. Impingement studies with other liquids than LBE illustrated that the impacting droplet forms a crater in the liquid surface, followed by the formation of a liquid column which rises out of the center of the crater. The rising liquid column is called a crown, illustrated in Figure 4**.** This crown-shaped splashing form can exceed the original level of the liquid surface. The maximum height to which a crown can rise is a function of the impact energy. If the crown is unstable, small droplet can separate from its rim causing splashing. When these secondary droplets reenter the surface liquid, they bounce or spread since their impact velocity is small. The crown is mainly composed of target liquid but also contains droplet liquid. In the last stage, the cavity and the crown decreases. The crown thickens and the crater collapses. A central rebound column is formed out of the middle of the collapsed cavity. The bouncing is stated to be dependent on the droplet diameter, the impact velocity and the surface tension, which are encapsulated in the Weber number as elaborated in the next section. Bouncing and spreading are expected to occur at low impact energies (i.e. low Weber numbers), while splashing is expected at larger Weber numbers [23] [28]. The threshold from spreading to splashing is determined for water. The boundary is not sharp, nor certain. Increasing the impact velocity and droplet diameter increase the chances of splashing [29].

2.5.3 WEBER NUMBER

The previous sections indicate that other parameters next to the droplet size, impacting surface, and surrounding fluid properties have a major impact on impingement outcomes, namely: the impact energy and the impact velocity of the droplet. In sum, results of water within the framework of aerosol formation show that high impact energies yield splashing. This indicates the importance of the kinetic droplet energy.

The parameter used to quantify the impact energy is the Weber number [24], [30], [31]. This dimensionless quantity describes the ratio between the inertial forces of the liquid to the surface tension as shown in formula (2), with (ρ) the LBE density in [kg/m^3], (v) the impact velocity of the droplet in [m/s], (d) the droplet diameter in [m] and (σ) the surface tension in [N/m].

$$We = \frac{\rho\, v^2\, d}{\sigma} \tag{2}$$

The impact velocity (v) and the diameter (d) are to be determined in this study. Afterwards, the Weber number for the impinging droplets can be determined. The final aim is correlating LBE droplets with certain Weber numbers to their resulting splashing forms and aerosol characteristics, as is already documented for water impingement phenomena [26], [27], [32], [33].

The density of LBE at 160 °C is 10,522 kg/m³ and the surface tension is 0.41 N/m [34]. For a similar sized drop with a given velocity, the Weber number for an LBE droplet will then be ± 1.87 times that of a water droplet [35]. Several experiments with water and other fluids prove that the higher the value of the Weber number, the larger the droplet deformations during impact [24], [32]. As will be shown further on, for a similar droplet size, an LBE droplet will also have a greater impact velocity than a water droplet. All these observations already indicate that splashing and the secondary droplet formation may occur more readily in LBE than in water.

2.5.3.1 Impact velocity

As can be seen in equation (2), the impact velocity is required to calculate the Weber number. The impact velocities can be derived from high-speed camera recordings, which are mainly used to characterize falling droplets and their impact mechanism. To determine which type of high-speed camera is required to record the fast-falling droplets, the impact velocities are first estimated with following equations. Afterwards, the actual impact velocities and Weber numbers are determined after MATLAB processing of the recorded high-speed camera footage. This will allow to make predictions of which splashing forms and which aerosol characteristics LBE droplets with a certain Weber number can generate.

Calculations of the velocity of a droplet starts by considering the forces acting on the droplet. A droplet falling in a gravity field in a medium is accelerated by the gravitational force which is counteracted by buoyancy (due to the density difference between medium and droplet) and a drag or resistance force (related to the relative velocity of the droplet with respect to the medium).

The general resistance force (F_r) on a spherical object of radius r [m] is described as in equation (3): with (C_d) drag coefficient, (ρ_m) density of the medium in [kg/m^3], (v) the velocity of the medium in comparison to the object in [m/s] and with (A) the projected surface area of the object in [m^2].

$$F_r = C_d \, \frac{1}{2} \, \rho_m \, v^2 A \tag{3}$$

A falling object at high velocity experiences a resistance force upwards. When the total force becomes zero, the droplet reaches a constant velocity called the terminal velocity. At this point the resistance force (F_r) of the medium on the object is equal to the gravity force (F_z) minus the buoyant force (F_b).

$$F_z - F_b = F_r$$

$$\leftrightarrow m \, . \, g \; - \; \frac{m}{\rho} \, \rho_m \, g = C_d \, \frac{1}{2} \, \rho_m \, v^2 A$$

From this the velocity of the droplet can be calculated as

$$v = \sqrt{\left(\frac{2 \, m \, g \, (\rho \; - \; \rho_{m)}}{C_d \, A \, \rho \, \rho_m} \right)}$$

With $V = \frac{m}{\rho}$

With $V_{sphere} = \frac{4}{3} \pi r^3 = \frac{1}{6} \pi d^3$

With $A_{Projected\ area} = \pi r^2 = \frac{1}{4} \pi d^2$

$$\leftrightarrow v = \sqrt{\left(g \; \frac{4}{3} d \; \frac{(\rho_{LBE} - \rho_m)}{\rho_m \, C_d} \right)} \tag{4}$$

This equation (4) represents the terminal velocity, i.e. the maximum velocity a falling sphere can reach in a medium with (g) gravitational acceleration 9.81 m/s², (d) diameter in [m], (ρ_{LBE}) density of LBE in [kg/m^3], (ρ_m) density of the medium (argon) in [kg/m^3] and (C_d) the drag coefficient [24], [36].

2.5.3.2 Drag coefficient

To calculate the droplet's terminal velocity, the drag coefficient (C_d) from equation (4) is required. C_d is influenced by fluid flow phenomena; shape resistance and friction resistance. The shape resistance occurs when an object flows through a medium. Turbulence occurs behind the object at considerable flow velocities. The pressure in this turbulent zone is smaller than the pressure before the falling droplet. Because of this pressure difference, a force arises opposite to the direction of the movement. For this reason, the shape drag is also called the pressure drag. The other frictional force is described by the Reynolds number, illustrated in formula (5) with (ρ) the density of the medium in [kg/m^3], (v) the velocity of the medium in [m/s], (l) the length of the object in [m], (η) the dynamical viscosity of the medium in [Pa·s]. The Reynolds number (Re) is a dimensionless parameter from flow theory, used to determine whether a flow is turbulent or laminar.

$$Re = \frac{\rho\, v\, l}{\eta} \tag{5}$$

The influence of both shape and friction drag is described as the drag coefficient C_d. For low Reynolds numbers i.e. for laminar flow, the drag coefficient for a sphere is derived from the Stokes law. For higher Reynolds numbers, the drag coefficient is derived from empirical formulas [24], which are based on the Stokes law, the Oseen law or the Goldstein law:

$$C_d = \frac{24}{Re} \text{ (Stokes)} \tag{6}$$

$$C_d = \frac{24}{Re}\left(1 + \frac{3}{16}Re\right) \text{ (Oseen)} \tag{7}$$

$$C_d = \frac{24}{Re}\left(1 + \frac{3}{16}Re - \frac{19}{1280}Re^2 + \frac{71}{20480}Re^3 - \frac{30719}{34406400}Re^4 + \cdots\right) \text{ (Goldstein)} \tag{8}$$

In this work we use the formula derived by Yang et al [24], based on the Oseen law, as this allows calculating the drag coefficient for Reynolds numbers up to 2.10^5:

$$\mathrm{C_d} = \frac{24}{Re}\left(1 + \frac{3}{16}Re\right)^{0.635} cos^3\alpha + 0.468\, sin^2\alpha \tag{9}$$

$$\text{with } \alpha = \left(1 - e^{-3.24x^2 + 8x^4 - 6.5x^5}\right)\frac{\pi}{2}$$

$$\text{and } x = \frac{ln(1 + Re)}{10}$$

As previously stated, the drag coefficient combines the friction drag and the shape or pressure drag. It is assumed that the first part of equation (9) indicates the friction drag C_f and the second part represents the pressure drag C_p [24], [36]*:*

$$C_d = C_f + C_p$$

$$\text{With } C_f = \frac{24}{Re}\left(1 + \frac{3}{16}Re\right)^{0,635} cos^3\alpha = C_{f0}\, cos^2\alpha \tag{10}$$

$$\text{And } C_p = 0.468\, sin^2\alpha \tag{11}$$

$$\leftrightarrow C_d = C_{fo}\, cos^2\alpha + 0.468\, sin^2\alpha \tag{12}$$

The equations are assuming that the falling object has a spherical shape. As already discussed, this is not always the case.

2.5.3.3 Impact time

As the impact of a droplet on a surface is a complex event, it is difficult to predict what time scale to expect. As a first estimate, the impact time during which an elastic colliding droplet is in contact with a surface is used as described by formula (13) with (ρ) the LBE density in [kg/m^3], (r) the droplet's radius in [m], (σ) the surface tension in N/m [30].

$$\tau = \left(\frac{\rho\, r^3}{\sigma}\right)^{1/2} \tag{13}$$

The impact time (s) is thus not affected by impact velocity but by droplet radius.

3 THE SPLAT SETUP

3.1 SPLAT setup design

As discussed in chapter 2, when a leak would occur in LBE piping systems inside MYRRHA or in one of the LBE carrying auxiliary system, LBE droplets will be released. The relevant surfaces to analyze are a liquid LBE surface and a dry smooth solid surface. Furthermore, two impinging droplet types are studies; small (sub-mm sized) droplets and large (> mm sized) droplets to cater for the expected droplet sizes in MYRRHA.

To determine the characteristics of formed LBE aerosols, a specific 'liquid impingement setup' was designed and built at SCK CEN. The 'SPLAT setup' is designed to study the impact of LBE droplets on the surfaces and their formed aerosols within a gas tight chamber, which allows mimicking the gas conditions prevailing in MYRRHYA.

To generate droplets in a well-controlled fashion, it was decided to implement a dispenser in the SPLAT setup. To characterize the impact, a high-speed camera was considered to allow visualization of the phenomenon and to quantify the impact velocity. The requirements for this high-speed camera are based on the results of a parametric survey as discussed in the following section 3.2. In addition, to quantify the LBE aerosols arising from the liquid impingement, a scanning mobility particle sizer (SMPS) and an optical particle detector (OPC) are used. A schematic overview of the SPLAT setup is shown in Figure 7.

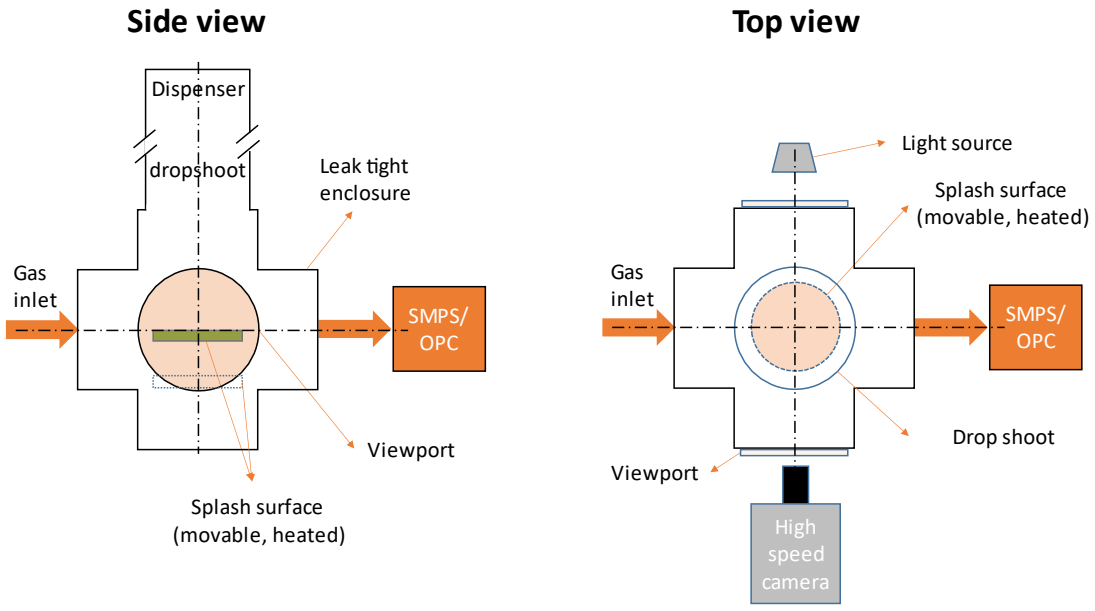

Figure 7: Schematic overview of the SPLAT setup.

The setup starts at the top with the droplet dispenser, inserted in a home-made enclosure. A close-up of the leak tight SPLAT impact chamber is illustrated in Figure 8. The droplet dispenser is connected through a vertical drop shoot to the impact chamber of the setup. As drop shoot, a simple pipe is used with a length of 1 m up to 5 m, which is the maximum relevant height foreseen in the reactor and its auxiliary systems [12]. It is also possible to perform experiments without drop shoot. Then, the distance between the dispenser outlet and impacting surface is 40 cm.

The enclosure consists of a 6 way ISO-K 200 cross-piece [37]. The top flange is used for the drop shoot. Of the side flanges, 2 are capped by viewports and 2 are capped by gas inlet, - and outlet parts. The latter flanges are related to the gas flow system and are capped by conical flanges to avoid turbulence when injecting or extracting gas into or out of the chamber through these flanges.

The left cone is connected to a mass flow controller which ensures the creation of a desired constant gas flow in the chamber. The right cone is connected to the SMPS, the OPC detector and to the vent through a custom designed 3-way splitter. Inside the chamber, the bottom flange houses the impact surface, adaptable in height with a laboratory jack. The surface is perfectly aligned to the center of the chamber to ensure the generated droplet hits the surface in its middle and to maximize the camera field of view. The bottom flange is computer controlled and can be moved up and down to open or close the setup, to change the impact surface or to clean the chamber.

Figure 8 also shows 2 angled half-nipples at the top of the chamber. The right one accommodates a second vent system. The vent flow is sent through an impact filter followed by a HEPA filter before a central gas –exit system. The other nipple is used to flush the chamber with argon or nitrogen gas to create an inert atmosphere. It is also possible to create a vacuum atmosphere in the setup.

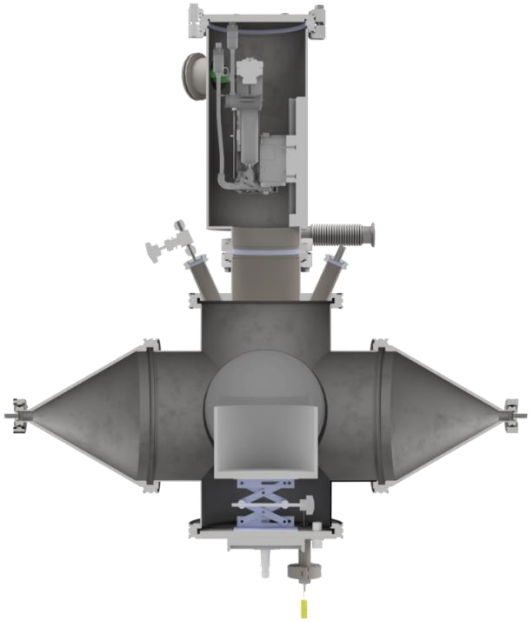

Figure 8: Cross section of the SPLAT 6-way cross-piece with the dispenser at the top.

3.2 Parametric survey

Prior to building the SPLAT-setup, an experimental parametric survey was performed to estimate what to expect of liquid LBE impingement with respect to impact velocities and impact time. This is important in order to determine which camera specifications were required to ensure capturing the falling droplet and the impact on the surface with sufficient resolution.

To get an idea of the time frames in which the impingement occurs, the impact velocity of LBE droplets of 0.5 and 1.5 mm diameter were estimated for the fall heights relevant for the SPLAT setup. From this, the Weber number and impact times were calculated. These results will allow to make predictions of what framerates are required and how long the camera needs to record. In addition, these parameters are also calculated for water droplets. This way, this section provides an overview of the expectations of LBE compared to water, for which many references are available.

3.2.1 IMPACT VELOCITY

The velocities for LBE and water droplets of 0.5 mm and 1.5 mm diameter as a function of the fall height were calculated through equation (4) and equation (12) in section 2.5.3.1 and 2.5.3.2. The results are illustrated in the graphs in Figure 9 and Figure 10.

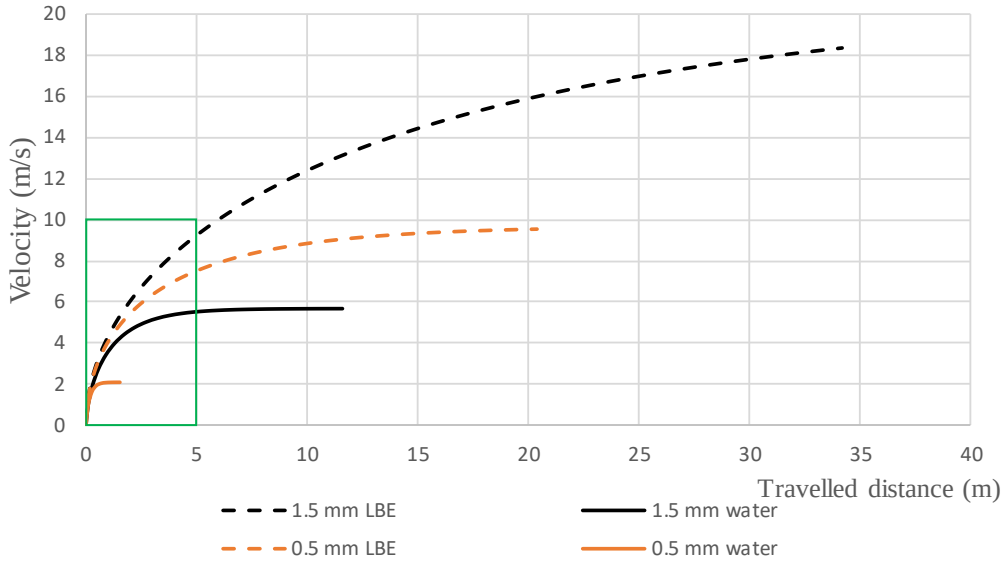

Figure 9: Estimated velocities of falling LBE and water droplets of 0.5 mm and 1.5 mm diameter in function of the travelled droplet distance.

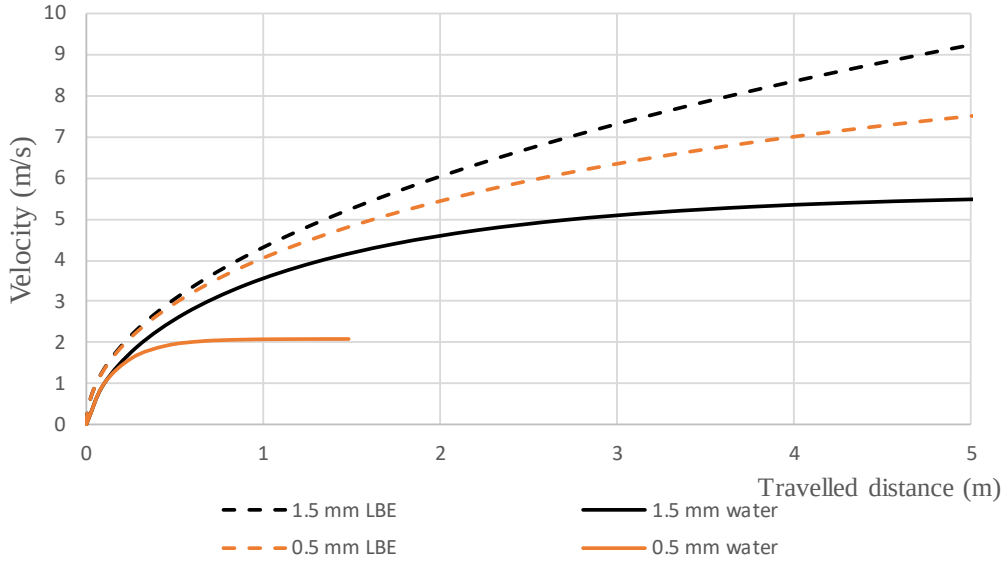

Figure 10: Estimated velocities of LBE and water droplets of 0.5 and 1.5 mm diameter, impacting from 0 - 5 m height.

Figure 9 illustrates the relation between the velocities of similar sized water and LBE droplets as a function of the fall height. The dotted lines illustrate the velocities of falling LBE droplets and the solid lines show the velocity for similar falling water droplets.

The droplet velocities are iteratively calculated by first choosing a random initial velocity. For this initial velocity the Reynolds number and the auxiliary parameters x and α, and the drag coefficients Cf_0, C_d are calculated as explained in section 2.5.3.1 and 2.5.3.2. An initial velocity $v_0 = 0$ was chosen as starting point.

After all parameters are calculated, the acceleration for step *i* can be calculated and from that the velocity for step *i*+1 is calculated using formula (15):

$$a(t_i) = \frac{1}{m_0}\left(g(\rho_0 - \rho_m)\frac{1}{6}\,\pi\,d^3 - \frac{1}{8}\pi\,d^2\rho_m\,{v_i}^2\,Cd\,(v_i)\right)$$
$$\text{With } a(t) = \frac{dv(t)}{dt} \approx \frac{v_i - v_{i-1}}{\Delta t} \leftrightarrow v_{i+1} = a_i\,\Delta t + v_i \qquad (15)$$

Figure 9 illustrates that the velocities of falling water and LBE droplets increase with increasing distance travelled and with increasing droplet size. When comparing LBE droplets with water droplets, it can be seen that the LBE droplets (dotted lines) reach higher velocities than water droplets (solid lines) at a given travel distance. This can be explained by the higher density of LBE. The velocity values reach a plateau after a certain fall height: this is the 'terminal velocity' of a falling droplet. At the terminal velocity, the downward gravity force of the droplet is equal to the upwards buoyancy and drag forces. LBE droplets of 1.5 mm diameter start levelling out when falling from ± 33 m height. LBE drops with 0.5 mm diameter reach their terminal velocity of ± 9.6 m/s at ± 16 m distance travelled. Water droplets of 0.5 and 1.5 mm diameter have lower terminal velocities of 2 m/s and 5.6 m/s, which is reached after a travel distance of ± 1 m and ± 10 m, respectively.

In brief, these findings illustrate the influence of fluid density, fall height and droplet size on the velocity of a falling droplet.

The heights to consider in MYRRHA are a few cm up to maximum 5 m. The green box in the graph of Figure 9 delimits the considered travel distances in this study. Figure 10 zooms into the velocities of LBE and water droplets, impacting from a height of 40 cm up to 5 m to offer a clearer view. It is clear that for MYRRA a typical droplet will never reach its terminal velocity. In the study presented in this thesis, the impingement experiments are performed at only 40 cm height. The impact velocity at this travel distance is estimated to be ± 2.65 m/s for an LBE droplet of 0.5 mm diameter and ± 2.73 m/s for an LBE droplet of 1.5 mm diameter.

Through iteration, the exact impact velocities for LBE and water droplets, falling from a height of 40 cm, 1 m and 5 m are determined and listed in Table 1 and in Table 2.

Table 1: Impact velocities of LBE droplets with 0.5 and 1.5 mm diameter at 40 cm, 1 m and 5 m height.

Impact velocities of LBE droplets (m/s)		
	Droplet diameter (mm)	
Distance travelled (m)	**0.5**	**1.5**
0.40	2.65	2.73
1.00	4.05	4.31
5.00	7.50	9.24

Table 2: Impact velocities of water droplets with 0.5 and 1.5 mm diameter at 40 cm, 1 m and 5 m height.

Impact velocities of water droplets (m/s)		
	Droplet diameter (mm)	
Distance travelled (m)	**0.5**	**1.5**
0.40	1.81	2.54
1.00	2.05	3.70
5.00	2.08	5.52

When comparing Table 1 and Table 2, it is clear that the impact velocities increase with increasing fall height and with increasing droplet diameter and that LBE droplets reach higher terminal velocities than water droplets. The difference is due to the higher density of LBE compared to water. For LBE, the travel distance is the dominant parameter.

This impacting velocity plays a key role in the impact of droplets on a surface: as the impact energy increases, also the amount of splashing increases.

3.2.2 WEBER NUMBER

Table 3 and Table 4 illustrate the Weber number for LBE and water droplets, calculated with the above-discussed impact velocities.

Table 3: Weber number estimations for LBE at 140 °C.

Weber numbers for LBE droplets							
	Diameter (mm)						
Velocity (m/s)	**0.1**	**0.5**	**1**	**1.5**	**2**	**2.5**	**3**
1	2.55E+00	1.27E+01	2.55E+01	3.82E+01	5.10E+01	6.37E+01	7.65E+01
2	1.02E+01	5.10E+01	1.02E+02	1.53E+02	2.04E+02	2.55E+02	3.06E+02
3	2.29E+01	1.15E+02	2.29E+02	3.44E+02	4.59E+02	5.73E+02	6.88E+02
4	4.08E+01	2.04E+02	4.08E+02	6.12E+02	8.16E+02	1.02E+03	1.22E+03

Table 4: Weber number estimations for water at 20 °C.

Weber numbers for water droplets							
	Diameter (mm)						
Velocity (m/s)	**0.1**	**0.5**	**1**	**1.5**	**2**	**2.5**	**3**
1	1.43E+00	7.14E+00	1.43E+01	2.14E+01	2.86E+01	3.57E+01	4.29E+01
2	5.71E+00	2.86E+01	5.71E+01	8.57E+01	1.14E+02	1.43E+02	1.71E+02
3	1.29E+01	6.43E+01	1.29E+02	1.93E+02	2.57E+02	3.21E+02	3.86E+02
4	2.29E+01	1.14E+02	2.29E+02	3.43E+02	4.57E+02	5.71E+02	6.86E+02

The Weber number for the first value of Table 3 is calculated for an LBE droplet with a temperature of 140 °C as in equation (2) from section 2.5.3.1:

$$We = \frac{\rho\, v^2 d}{\sigma}$$

$$\leftrightarrow We = \frac{10{,}548\,.\,1^2\,.\,0.1\,10^{-3}}{0.41} = 2.55$$

From the results of Table 1, it can be seen that LBE droplets falling over a distance of 40 cm are estimated to impact the surface at a speed of order 2.7 m/s. Therefore, the row displaying the Weber number at a velocity of 3 m/s in Table 3 is expected to be the closest to the actual results of the high-speed camera experiments. When comparing LBE and water, the Weber number for LBE is almost 80 % higher than for similar water droplets, falling under similar conditions.

In brief: in view of this theoretical study, LBE is expected to yield more extensive splashing than water during liquid impingement because of the liquid metal's high density and impact velocities. It is expected that, owing to this, LBE droplet impingement will generate more secondary (ejected) droplets and thus more aerosols than water droplets. To prove this statement, there is need for experimental LBE liquid impingement values.

3.2.3 IMPACT TIME

Table 5 shows the impact times in ms for LBE droplets at 140 °C for several droplet radii from 0.1 up to 4 mm as calculated with equation (13). Table 6 also shows the impact times but for water droplets instead of for LBE droplets.

Table 5: Impact times of LBE droplets with varying size

Radius (mm)	**0.1**	**0.5**	**1**	**1.5**	**2**
Impact time (ms)	0.4	1.2	2.2	3.3	4.6

Table 6: Impact times of water droplets with varying size

Radius (mm)	**0.1**	**0.5**	**1**	**1.5**	**2**
Impact time (ms)	0.3	0.9	1.6	2.5	3.5

The time during which a droplet is in contact with the surface is observed to be about 35% higher for LBE droplets than for water. Table 5 and Table 6 illustrate the short time frames in which the droplet is in contact with the surface. To record the splashing phenomenon, a camera device which can record these short impact time frames is required. From the impact velocities, calculated in with equation (15), the time between release and impact can be calculated. For a fall height of 40 cm, a drop reaches the point of impact after 0.28 seconds, which is orders of magnitude larger than the impact time. The frame rate is usually chosen is such a way that it is 10 x higher than the time frame of the phenomenon, so that the phenomenon can be recorded in enough detail. A complication is that ‘long recording times’ (i.e. several times the impact time) will be required to record sufficient time before and after the impact.

3.3 SPLAT setup components

The results of the experimental parametric survey enable to specifically determine which specifications are required for the high-speed camera and other SPLAT setup components to study liquid impingement and aerosol formation of LBE. This section elaborates on section 3.1 and section 3.2 and provides a description of the parts of the SPLAT setup.

3.3.1 DISPENSER

As shown in Figure 9 and Figure 10 above, the SPLAT setup starts with a non-contact piezo dispenser (Vermes Micro dispensing GmbH, Holzkirchen, Germany), functioning as a droplet generator. Micro dispensing systems are used for car electronics, for car door coverings, in the LED industry to dispense silver adhesives to chips, to dispense conductive paste onto thermocouples and so on [38].

The micro dispenser components are shown in the exploded view in Figure 11.

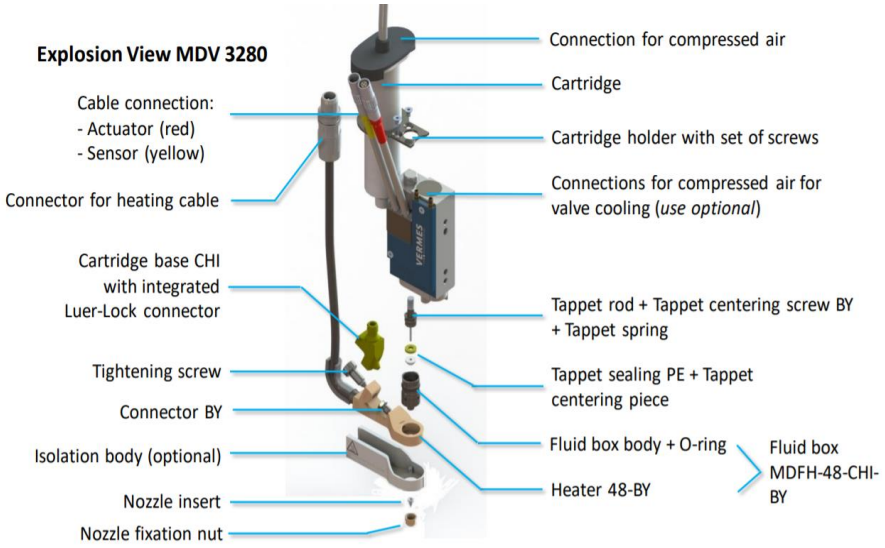

Figure 11: Exploded view of the Vermes micro dispenser's parts [39].

LBE is applied to the system by filling the dispenser's cartridge inside the cartridge holder. The cartridge is connected to the cartridge base, which are both heated with the multi-functional controller (MFC) to ensure hotmelt dispensing. The cartridge top is closed with a compressed air adaptor. The applied supply pressure moves the fluid in the cartridge downwards in direction of the cartridge base [39].

The blue box in Figure 11 is the valve body. It accommodates the electronics module, the piezo actuator system, the adjust screw and the tappet, which is located in the fluid box body. The valve is connected with the micro dispensing controller (MDC). An inside view of the valve is illustrated Figure 12. It can be seen that the fluid box body is inserted in the bottom opening of the valve.

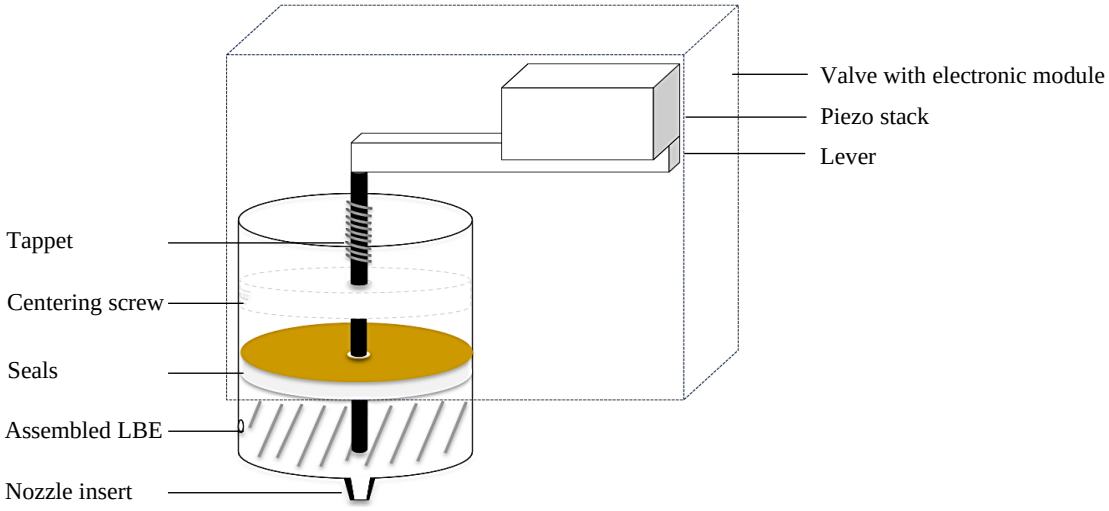

Figure 12: Overview of the fluid box body in the valve.

Imagine the dispenser's fluid box body as 'two halves'. The upper halve of the fluid box body consists of a tappet with a tappet rod and a tappet spring. This upper part of the fluid box body is inserted at the bottom of the valve to ensure the connection with the piezo through a lever; the piezo moves the lever, and thus the tappet back and forth inside the fluid box body [40]. The fluid box body's upper part is divided from the lower part through tappet seals.

The lower halve of the fluid box body is inserted in a mounting body, heated with the MFC to ensure hotmelt dispensing. In the lower part of the fluid box body, the LBE assembles to be dispensed by the downward motion of the tappet. Lastly, the conical shaped nozzle insert is foreseen at the bottom end of the fluid box body. The nozzle openings used in this study are 150 µm and 1000 µm.

3.3.1.1 Piezo technology

The used micro dispensing system is based on non-contact piezo technology. Non-contact dispensing is sometimes referred to as "jetting" because it involves ejecting liquid. Piezo technology points out to the dispenser's piezo actuator which is composed of two stacks of ceramic disks of crystalline material. When an electrical signal is applied to the valve, a mechanical deformation is provoked due to expansion or contraction of the ceramic [41]–[43]. When applied to the Vermes micro dispenser, this results in the movement of the tappet. The piezo is electronically driven by the MDC. Because the tappet is surrounded by a spring, the movement of the piezo is transferred to the spring by the lever. The movement of the tappet results in the movement of the liquid through the fluid chamber. During contraction of the piezo ceramic, the lever moves upwards, forcing the tappet to move in the same direction. LBE is forced to flow from the cartridge to the cartridge base. Hereafter, LBE is sucked from the cartridge base to the fluid box through the upward tappet movement. During the expansion of the piezo, the lever moves down. The tappet moves downward, 'pushing' the assembled fluid through the nozzle insert opening. The tappet movements are part of the dispensing parameters [43].

As already mentioned, the dispenser is controlled with 2 control units. The MFC is applied to control the temperatures of the cartridge, the fluid box and the valve. The MFC ensures hotmelt dispensing with maximum temperatures of 180 °C. The MDC is connected to the valve. It controls the piezo actuator and thus the tappet.

3.3.1.2 Dispensing parameters

The dispensing parameters to install in the MDC are listed and described in Table 7.

Table 7: Micro dispensing parameters.

Parameter	Unit	Range	Description
Rising time (RT)	ms	0.24 – 300 ms	During RT, LBE is sucked by the up moving tappet
Open time (OT)	ms	0 – 3000 ms	During OT, the valve remains open. LBE can run through the fluid channel under cartridge pressure.
Falling time (FT)	ms	0.08 – 300 ms	FT indicates the closing motion of the tappet in which LBE is forced to move from the lower halve of the fluid box body through the nozzle opening.
Delay	ms	0.1 – 1000 ms	Delay indicates the time in between two cycles.
Number of pulses		1 – infinite	Number of pulses are the number of dispensing cycles
Needle lift (NL)	%	0 – 100 %	NL means the stroke of the tappet
Supply pressure	bar	0 – 7 bar	The pressure assures a continuous flow of the liquid through the micro dispensing system.
Nozzle temperature	°C	1 – 180 °C	Temperature of the nozzle opening inside the mounting body
Cartridge temperature	°C	1 – 180 °C	Temperature of the cartridge inside the cartridge holder

All parameters affect the droplet that is being dispensed [39]. However, this study is only interested in droplets with a specific size. Therefore, the latter parameters "NL", "supply pressure", "nozzle temperature" and "cartridge temperature" were kept constant because not all parameters are required to obtain the desired outcome. Two types of LBE droplets are desired: namely small (µl) droplets and large (ml) droplets, both within millimeter diameter range.

3.3.2 HIGH-SPEED CAMERA

To obtain records of the liquid impingement phenomenon, a Photron SA3 (Photron Deutschland GmbH, Reutlingen, Germany) high-speed camera is used. The camera is chosen for its frame rate, based on the estimated impact velocities and impact times in section 3.2. The camera is positioned in front of the viewport of the SPLAT setup. From the recordings of the splashing of LBE droplets, qualitative information (i.e., droplet shape and splashing forms) and quantitative information (impact velocity and droplet size) can be derived. The height of the impacting surface inside the chamber is raised to align the surface with the camera's lens. At the opposite viewport, a LED light is foreseen.

Figure 13 illustrates the main camera components, namely: the camera's lens; the CMOS sensor which converts incoming photons to a digital value; the image signal processor and the interface input/output.

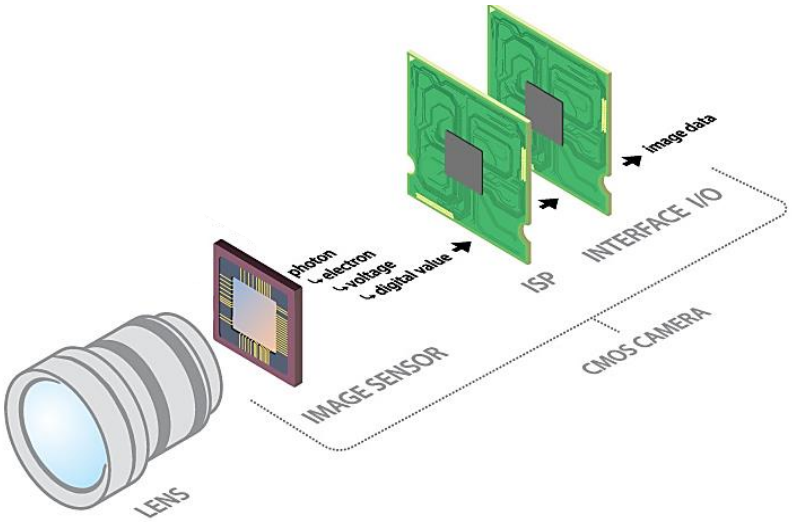

Figure 13: CMOS high-speed camera components [44].

First, the incoming light is absorbed by the camera's lens and focused onto the sensor by a lens focusing mechanism which moves the lens closer or further from the sensor [45].

The applied high-speed camera is equipped with a Complementary Metal-Oxide Semiconductor (CMOS) – type sensor [46]. The CMOS sensor consists of an array of pixels, made of light sensitive elements, micro lenses and micro electronical components. The CMOS converts the charge, created by the incoming light photons onto the sensor's photosensitive pixels, to a voltage (through the photodiode at the pixel site).

The signal is multiplied using an amplifier and converted into a digital value using an analogue to digital convertor (ADC). The CMOS chip contains an ADC for each pixel column, which allows higher frame rates compared to standard sensor chip-types which only have 1 ADC for all pixels [44], [45], [47]–[49].

The resolution of the camera refers to the details of the image and is expressed in terms of pixels. The highest number of pixels for the high-speed camera used in this study is 1024 x 1024. The frame rate indicates the amount of video frames per second being captured, expressed in frames per second (fps). At full resolution, the Photron provides 1000 fps. A high resolution means more pixels per image, so more pixels per frame rate. A higher frame rate therefore implies a reduction in resolution and vica-versa [46], [47], [50]. To record the impacting LBE droplets, a compromise between sufficient details and significant frames per seconds is thus required. The required frame rate is thus dependent on the velocity of the falling droplet.

3.3.3 SCANNING MOBILITY PARTICLE SIZER AND OPTICAL PARTICLE COUNTER

After a flow of well-controlled droplets have impacted the surface in the impact chamber of the SPLAT setup, aerosols are formed due to liquid impingement. The aerosol particle size and amount (referred to as 'aerosol particle size distribution' or PSD) resulting from the impact will be analyzed using a Scanning mobility particle sizer (SMPS) and an Optical Particle Counter (OPC). The results of both complementary detectors will be merged to cover the entire size range due to the large range of particle size that are is expected (50 nm -100 µm). The mass flow controller at the left conical- shaped side of the SPLAT chamber generates a continuous laminar flow rate. The flow forces the generated aerosols to move towards the detector openings at the opposite cone.

3.3.3.1 Scanning Mobility Particle Sizer

The smallest aerosol particles are counted using a GRIMM SMPS condensation particle counter type 5416 with Vienna Rieschl type DMA electrostatic classifier (GRIMM Aerosol Technic Ainring GmbH, Ainring, Germany).

The working principle is based on the mobility of charged particles in an electric field. When the aerosol particles enter the SMPS, the particles are forced to pass an impactor filter to filter the oversized particles. The particles which are not filtered out are able to pass through a bipolar neutralizer. This neutralizer is a radioactive Am-241 source with an activity of 3,7 MBq and generates positive and negative ionized aerosol particles [51]. The charged particles then enter a Differential Mobility Analyzer (DMA) which classifies the charged particles in fixed size bins, based on their electrical mobility. The classified particles then pass from the outlet of the DMA towards the SMPS' internal condensation particle counter (CPC).

The SMPS' DMA is illustrated in Figure 14. It consists of a cylinder of two electrodes. The outer electrode is kept at ground potential while the center electrode has a high negative voltage. The difference in voltage between the center electrode rod and the tube generates an electric field. The main flow through the center of the DMA is particle-free 'sheath' air. The SMPS operates at a flow inlet rate of 0,3 L/min and a sheath flow rate of 3 L/min. The aerosol particle flow is injected between the center rod and the outer tube and drawn toward the bottom of the column of the DMA. The particles move downwards through the cylinder. Negative particles are pushed towards the outer wall. Particles with a positive charge move across the sheath air towards the central negative electrode.

Particles with a higher electrical mobility are drawn towards the inner rod at a faster rate than those with a lower electrical mobility. Since the particles flow toward the bottom of the DMA tube, the electrical mobility of a particle together with the strength of the electric field and the sheath air flow determines where the particle will impact the center electrode. There is an exit foreseen near the end of the central rod. Particles leave through the exit where they would normally impact the electrode. For a given voltage, only particles with a certain electrical mobility will exit through the slit [51]–[54]. Thus, in brief, a DMA is used to categorize aerosol particles based on electrical mobility since the voltage on the central electrode can be directly related to the electrical mobility of the particles exiting the DMA.

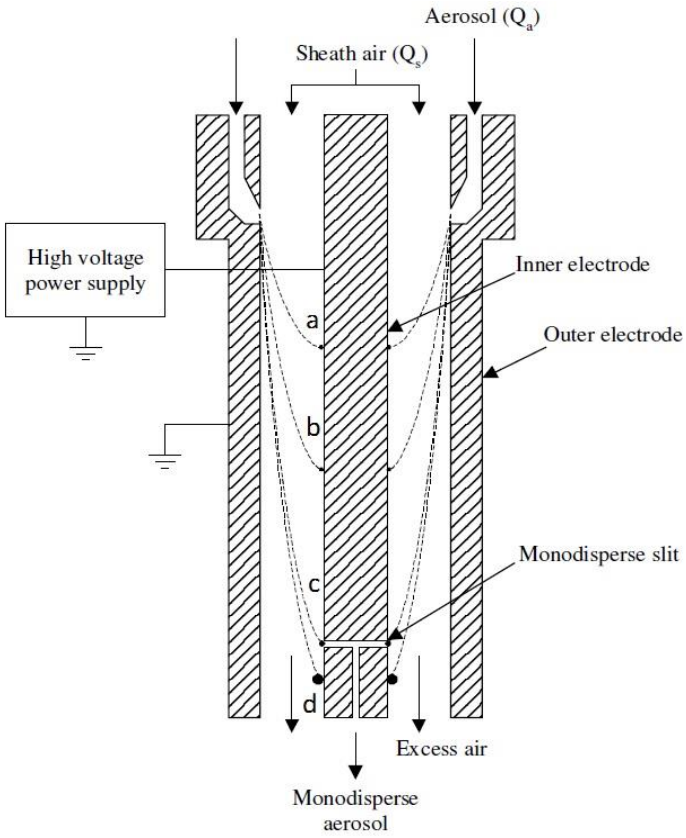

Figure 14: Schematic overview DMA [55].

This allows the SMPS to provide information about the amount of particles within the DMA pre-set size range [52], [54], [56], [57]. The classified charged particles are counted by the internal condensation particle counter (CPC) of the SMPS. The working principle is visualized in Figure 15.

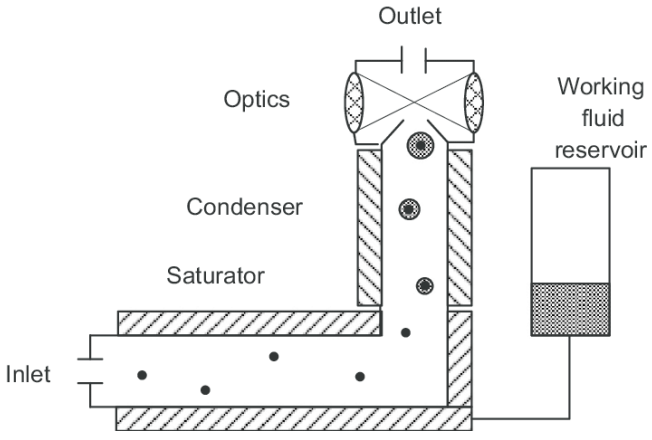

Figure 15: SMPS' CPC working principle [61].

To visualize the particles by the optical techniques of the CPC, the nanoparticles need to be enlarged. For this reason, size classified particles exiting the DMA are first enlarged by sending the flow through a heated saturator tube (Figure 15) where it is mixed with iso-butanol vapor. Hereafter, the particles pass a cooled condenser. This ensures growth by condensation of the iso-butanol vapor upon the surface of an existing particle. This increases the particles sizes so that they can be sensed by a photodetector as they pass through a laser beam. The optical detection is based on light scattering. The droplet enters the laser chamber and generates scattered light by passing the laser beam, which is collected at a scattering angle of 90 °C with a mirror onto a photodiode. The photodiode of the OPC detects and counts aerosol particles [52], [58]–[60].

3.3.3.2 Optical particle counter

A second detector used is a PALAS optical particle counter (OPC) (PALAS GmbH, Karlsruhe, Germany) to extend the counting range of the LBE aerosol particles with a diameter of 0.1 µm and up. The OPC contains a laser illuminated optical system which ensures single particle detection. An inlet flow, generated inside the SPLAT enclosure, arrives in the PALAS WELAS aerosol sensor. The particles pass through a Xenon light source. The passing particles create scattered light [62]. The scattered light signals are collected by a photosensitive detector: a photomultiplier. The photodetector electric signal is amplified. The amplitude of the detected scattering signal pulses is a function of the particle size. The scattered light pulses are converted to a corresponding size category, based on the pulse height. Since each scattered pulse corresponds to 1 particle, which is sorted to a size category; a particle concentration is obtained. In contrast to the SMPS, which is only able to count the particles within pre-set size ranges, the OPC can count and measure the size of aerosol particles with a minimum diameter of 0.1 µm [63], [64].

4 EXPERIMENTAL SETUP AND PROCEDURES

4.1 Droplet generation with a micro dispenser

To generate LBE droplets, the SPLAT setup is equipped with a Vermes MDS 300 (VERMES, HOLZKIRCHEN, GERMANY) micro dispensing system. The MDS is controlled with an MFC 3000 multi-functional controller and an MDC 3280 micro dispensing controller. The MFC 3000 is used to ensure hotmelt dispensing because LBE melts at 125 °C.

4.1.1 PREPARATIONS

4.1.1.1 Filling the dispenser cartridge

To fill the dispenser cartridges, the conditioning LBE tank at the SCK CEN is heated to 150 °C 48 h upfront. When the tank reaches the desired temperature, the cartridges are filled with clean LBE up to 80 % of their capacity. To avoid the expansion of the cartridges due to solidification of LBE, the cartridges are inserted in a custom-made stainless-steel holder. The inner diameter of the holders is the same as the outer diameter of a fitting cartridge. The cartridges rely on a rubber stopper to close them. The cartridges are filled by letting LBE flow from the tank's tap into the cartridge. When approximately 80 % of the cartridge is filled, the tap of the LBE tank is closed.

4.1.1.2 Dispenser commissioning

The cartridge is inserted in the cartridge holder and screwed into the CHI-HT cartridge base. Then, the cartridge base, hollow screw connector and lower part of the fluid box body are inserted in mounting body which is heated to ensure hotmelt dispensing.

The fluid box body is provided with a TTF tungsten carbide tappet rod. The tappet rod with tappet spring is fixed in a stainless-steel tappet centering screw. The tappet is provided with a PE tappet sealing and a PEEK tappet centering piece.

To generate droplets, a N11-150 (150 µm opening) and N11-1000 (1000 µm opening) nozzle are used. One of the nozzles is screwed onto the fluid box body. Regarding the 'troubleshooting' section, no supply pressure is applied to the compressed air adapter of the cartridge, nor to the valve. Figure 16 illustrates the exploded view of the components of the dispenser.

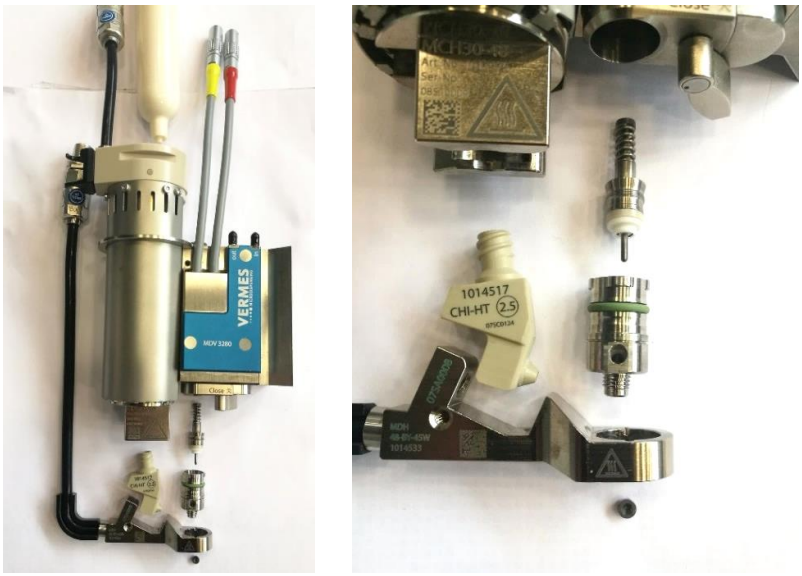

Figure 16: Dispenser commissioning components.

4.1.1.3 Initial adjust

Before dispensing or after every decommissioning, an adjust procedure is required to position the tappet inside the fluid box body correctly in relation to the nozzle. The adjustment procedure starts with a completely assembled dispenser and an empty cartridge. First, the cartridge and fluid box are heated to the same temperature as applied during the dispensing, namely 160 °C for the cartridge and 170 °C for the fluid box. After the temperatures are reached, the micro dispensing controller (MDC) is turned on. To adjust the tappet, the adjust screw on top of the valve is screwed counterclockwise with a torque until the screw cannot be rotated any further. Next, the adjust screw needs to be screwed completely open again. Hereafter the adjust screw is screwed inwards again until a value between 0 % and 1 % is reached. The tappet is now positioned correctly relative to the nozzle and a green light appears on the MDC. The adjustment is confirmed by pressing enter on the MDC display.

4.1.2 DISPENSING LBE DROPLETS

After the adjust procedure, the dispensing can start. First, the cartridge is inserted in the dispensing system and the MFC 3000 is turned on. The MFC 3000 consists of 4 channels. Depending on how the connections are connected, the channels can be used to heat or cool the components of the dispenser. In this setup; channel 1 is used as cartridge heater; channel 2 refers to the fluid box heater and channel 4 is the piezo cooler. Channel 1 is heated to 160 °C, channel 2 is set to 170 °C and channel 4 is cooled to 60 °C. After the channels have reached their temperatures, the MDC is switched on. No supply pressure is applied to the cartridge nor the valve. To dispense droplets, several parameters need to be installed as desired. The dispensing parameters are: open time, rising time, falling time, needle lift, delay, number of pulses, cartridge temperature and nozzle temperature.

4.1.2.1 Determination of droplet size

To analyze the correlation between the parameters and the generated droplet, the varying parameters are one by one set to their minimum and maximum, while the parameters needle lift, cartridge temperature, fluid box temperature and supply pressure are kept constant. The observations are written down. The parameters cartridge temperature and nozzle temperature are kept constant at 160 °C and at 170 °C, as well as the parameter needle lift at 70 % during the droplet diameter determination experiments.

Droplets are dispensed onto an aluminum tray positioned 5 cm under the nozzle. After dispensing with every parameter-set, the dispensed droplets are allowed to cool to room temperature and solidify. The solidified LBE droplets are then collected with tweezers and are weighed with an Alfa Mirage SD-200L analytical balance (ALFA MIRAGE, OSAKA, JAPAN). For every parameter-set, the weight of the dispensed droplet is noted.

To determine the dispenser's reproducibility or standard deviation, specific parameter-sets are dispensed eight times in succession. An average of the eight droplets weights and the standard deviation is determined.

4.1.3 CLEANING THE DISPENSER

Because LBE solidifies at room temperature, it is necessary to avoid cooling the dispenser system. But, if the nozzle needs to be changed or if the micro dispenser system is cooled down due to occurring dispensing problems, the cartridge base, the hollow connecting screw, the fluid box body, the tappet seals and the nozzle need to get cleaned to remove stuck LBE and LBE oxides. After cooling to room temperature, the dispenser is disassembled as much as possible. It is possible that due to the solidification and due to the oxides, the components are impossible to disassemble. This can be solved by heating the components using a heat gun set to 180 °C. until the stuck LBE flows out. The components can now be disassembled, using a suitable multi-functional tool of Vermes. Because oxides do not melt at 180 °C, LBE leftovers and oxides are removed from the components using LBE cleaner liquid, consisting of acetic acid, peroxide and water in a 1:1:1 ratio. Under a fume hood, a measuring cylinder is filled first with 20 ml demi water, followed by 20 ml 96 % acetic acid and 20 ml peroxide. The dispenser components are placed in a cup. The LBE cleaner is poured over them. The components are left to rest next 30 minutes. After 30 minutes, the components are flushed five times with demineralized water.

After flushing, the parts are further cleaned by hand using a nozzle insert cleaning tool, fluid box cleaners, cleaning rods and fluidic brushes of Vermes. The nozzle is cleaned by placing it on the nozzle insert cleaning holder. With a nozzle cleaning wire of the same diameter as the opening, the nozzle insert opening is removed from blocking parts. Lastly all parts are air dried. The parts may now be assembled again. Before starting dispensing, it is necessary to perform the adjust in 3.2.1.3 again since the nozzle, tappet and adjust screw were disassembled.

It is also possible to skip the time-consuming heating step by flushing the dispensing system while operating. For this purpose, a ADHESiQ PUR hotmelt cleaner is inserted in an empty cartridge. The cartridge temperature is increased to 180 °C with the MFC. In order to move the fluid through the system, a supply pressure of 1 bar is applied to the compressed air adapter. Hereafter the 'F1' button on the MDC is pressed to move the tappet upwards, to flush the dispenser. After flushing the complete dispenser, all parts are flushed with demi water after they are cooled to room temperature. The above-mentioned manual cleaning and dry steps were repeated.

4.2 Liquid impingement analysis

To determine the Weber numbers of dispensed impacting LBE droplets and to determine the impingement forms, a high-speed camera is implemented in the SPLAT setup.

4.2.1 HIGH-SPEED CAMERA COMMISSIONING

To record the liquid impingement phenomenon, a Photron fastcam SA3 (Photron Deutschland GmbH, Reutlingen, Germany) in combination with an AF micro NIKKOR 60 mm lens is used. The high-speed camera is positioned on the item undercarriage of the SPLAT setup in front of the viewport using a height adjustable tripod in combination with railings. The high-speed camera is positioned in line with the surface to impact in the gas tight intersection SPLAT chamber. At the opposite viewport, a LED light is fixed on the item undercarriage, aligned with the camera's lens. The dispenser is directly inserted in an inert enclosure on top of the SPLAT chamber without cartridge inserted. Figure 17 illustrates the experimental setup.

Figure 17: Experimental setup of the high-speed camera.

After all connections are checked, a solidified LBE cartridge is placed into the cartridge holder. The cartridge holder is closed off from the environment by screwing the compressed air adapter lid onto it. The compressed air hose is blocked with a fitting plug to create an under pressure. For the first series of experiments the 1000 µm nozzle was used. During the second experiment, a 150 µm nozzle insert is used. The high-speed camera is calibrated by imaging an object with well-known dimensions. The camera's installed frame rate is 15,000 fps. The applied resolution is 640 x 288. The shutter speed is 1/35000 sec. These settings provide 11,377 saved frames per 0.758 seconds.

4.2.2 IMPACTING SURFACES

The high-speed camera experiments are performed with two different surfaces. The liquid surface entails a 3 cm high round heated stainless steel tray filled to the top with LBE. To keep the LBE liquid, the surface is heated to 135 °C with a heating band. The temperature is measured with a type-K thermocouple. The temperature is maintained at the desired temperature by a PID controller. The liquid surface is raised to align it with the camera's lens using a laboratory jack. The other used impacting surface refers to a dry solid polished steel tray. Inside the tray, a polished plate is inserted perpendicular under the nozzle opening. The plate has the same height as the inner height of the inox tray. Otherwise, the high-speed camera would not have been able to perceive the surface. To align it with the camera's lens, a laboratory jack is placed underneath the tray as well. The dry solid surface is not heated. Figure 18 illustrates the impacting surfaces, which are inserted in the SPLAT chamber.

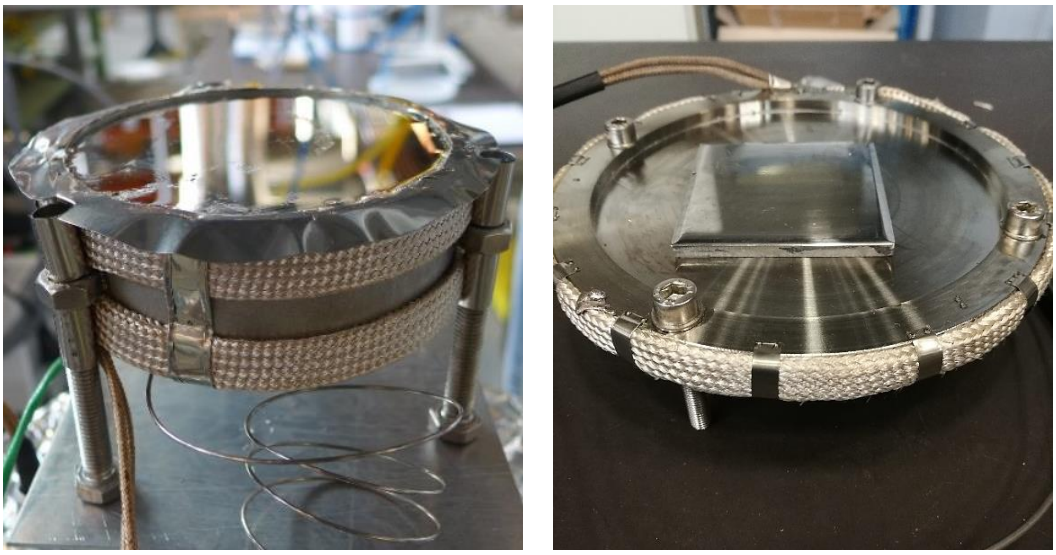

Figure 18: The impacting surfaces: liquid surface (left) and dry solid surface (right).

4.2.3 HIGH-SPEED CAMERA RECORDINGS

4.2.3.1 Liquid impingement with 1000 µm nozzle

To generate droplets, the MFC is switched on. The valve cooling channel 4 (depending on the connections) is set to 60 °C and the fluid box heater is set to 145 °C. After 10 minutes, the cartridge heater is set to 140 °C. After 20 minutes, the MDC is turned on. To decrease the leaking frequency, the cartridge temperature is lowered to 139 to 140 °C and the fluid box body temperature to 143 to 144 °C during the experiments. The installed dispensing parameters in the MDC are: 5 ms RT, 1 ms FT, 5 ms OT, 70 % needle lift, 100 ms delay and 4 number of pulses. Afterwards, the button 'trig' is pressed to dispense the required droplets. At the same time the 'trig' button is pushed, the camera is asked to record. By playing the recordings on the Photron software, the time frame of the phenomenon is selected and this time frame is saved. The surfaces were switched in between from liquid to dry solid.

To clean the dry solid surface in between the recordings, a cone of the SPLAT enclosure is removed. By the time the surface was cleaned from the solidified droplets on the surface by lowering the lower surface flange, a new leaking droplet arrived already. By opening the cone, the surface is easy to reach and thus rapidly cleaned. The surface is cleaned in between high-speed camera recordings by pushing off the impacted leaking droplets using a spoon and a piece of paper. Afterwards, the dispenser is requested to dispense. Simultaneously the camera is asked to record once again.

4.2.3.2 Liquid impingement with 150 µm nozzle

A 150 µm nozzle is used to analyze the impingement of smaller droplets. The dispensing parameters are: 1 ms RT, 0,6 ms FT, 1 ms OT, 70 % needle lift, 100 ms delay and 4 number of pulses. The cartridge was heated to 139°C and the fluid box to 143°C. Then, the impingement is recorded similarly to 4.2.3.1. At the end, the droplet diameters and velocities were processed using MATLAB.

4.3 Aerosol particle size distribution analysis

To determine the particle size distribution (PSD) of aerosols, generated by liquid LBE impingement, a SMPS and an OPC are implemented in the SPLAT setup.

4.3.1 SMPS AND OPC COMMISSIONING

To determine the PSD of the formed LBE aerosols, the SPLAT setup is flushed with an inert gas using a mass flow meter controller (Bronkhorst high tech b.v., Ruurlo, The Netherlands) with a maximum flow rate of 30 l/min. The mass flow controller was connected to the left cone of the SPLAT enclosure and provided with 2 bar argon gas.

The opposite right cone of the SPLAT setup is connected to the vent system, the inlet of the GRIMM SMPS condensation particle counter type 5416 with Vienna Rieschl type DMA electrostatic classifier (GRIMM Aerosol Technic Ainring GmbH, Ainring, Germany) and with the inlet of the PALAS OPC 2000 H with Palas welas aerosol sensor (Palas GmbH, Karlsruhe, Germany) with a 3 way-splitter.

To generate LBE droplets, the micro dispenser is positioned on top of the enclosure and equipped with a 1000 µm nozzle. The lid of the dispenser's chamber is closed, as well as all other flanges and lids of the setup.

The experiments are performed with a liquid and a dry solid surface. The liquid LBE surface is heated during the experiment to 135 °C. The dry solid surface is not heated.

4.3.2 PARTICLE SIZE DISTRIBUTION

Before starting the experiments, the SMPS device is switched on using the SMPS GRIMM nano 181 software to prepare the condensation and saturation of the device. After the SMPS has reached its temperatures, the enclosure is flushed with 2,6 l/min argon using the computer controlled mass flow controller.

Next, the dispenser's MDC is installed. The cartridge temperature is set to 139 °C and the fluid box temperature to 143 °C. The dispenser was requested to dispense an infinite number of LBE droplets, generated with 5 ms RT, 1 ms FT and 5 ms OT. During the impingement of the LBE droplets on the surface, the SMPS and the OPC are requested to measure the aerosol particle distribution using the device's software.

The results are gathered by the device's software in graphs.

5 RESULTS AND DISCUSSION

This chapter discusses the results of the experiments starting with the droplet generation results, which are discussed in section 5.1. Next section 5.2 deals with the technical difficulties that occurred, in order to facilitate further research. Liquid impingement (i.e. Weber numbers and splashing forms) of LBE droplets is studied in section 5.3. Finally, the PSD of the aerosols, resulting from the impact of LBE droplets is determined in section 5.4.

5.1 Dispensed LBE droplets results

5.1.1 CORRELATION OF DISPENSER PARAMETERS AND DISPENSED DROPLETS

Table 8 and Table 9 show the correlation of the dispenser parameters and the generated droplets. Only the varying parameters were inserted in in column 1 to 5 from Table 8. The cartridge temperature was kept constant at 160 °C, nozzle temperature at 170 °C, valve cooling at 60 °C and needle lift at 70 %. The last column of Table 8 shows the observations about the dispensed droplets. The bold outlined columns indicate the applied method to visualize the relationship between dispenser parameters and generated droplets, namely by setting all parameters one by one to their minimum, intermediate and maximum value. Table 8 shows the dispensed droplets when the dispenser was equipped with a 150 µm nozzle. Table 9 shows the results for a larger nozzle opening of 1000 µm.

The parameters in the first row of Table 8 were set at ‘random’ values to have a starting point to compare with. In the first row, the parameters rising time (RT), falling time (FT), open time (OT) and delay were therefore all set to 100 ms. Number of pulses is related to the Delay time, which is the time in between 2 dispensing cycles. Because most of the time only 1 droplet was instructed to dispense, the delay time had no influence. After dispensing using the first ‘random’ parameters in row one of Table 8, it was assumed that because the ‘number of pulses’ parameter was set to 1, only one droplet would be dispensed. Instead, two droplets were dispensed. A possible explanation can be that rising time or open time were set too high. A significant amount of liquid LBE was ‘assembled’ to dispense during the time in which the valve remained open. The dispensing volume was too much to dispense in a single droplet.

Row 2, 3 and 4 show the results of the varying values of RT while FT was kept constant at 100 ms and OT at 50 ms. When RT was set to its maximum value of 300 ms, 3 or 4 droplets were dispensed while when RT was set to its minimum value of 1 ms, only 2 small droplets were generated. It was expected that when increasing RT, the dispensing volume would increase and showing as large droplets being dispensed. It was not possible to see by the naked eye whether the droplets were larger than the previous. However, it was possible to see that more droplets were dispensed when RT was set to a high value in comparison with a low RT.

After experimenting with rising time, this parameter was set back to a constant value of 100 ms and FT was varied. When FT was set to its maximum of 300 ms, a flow rather than separated droplets were observed. This indicates that the falling time took too long to ‘cut’ separate droplets. The tappet moved ‘to slow’ downwards. During a falling time of 300 ms and a falling time of 150 ms no difference was observed. This can indicate that the falling time does not have a large influence or that the difference was not visible by the naked eye. When installing the downward motion of the tappet to 1 ms, only 1 droplet was dispensed. This indicates the ability of the tappet; being able to cut the fluid stream in droplets.

Table 8: Installed dispenser parameters and observations when dispensing was performed with a 150 µm nozzle. The bold outlined columns indicate the applied method, namely the parameters are set to a minimum, an intermediate and a maximum value.

RT (ms)	**FT (ms)**	**OT (ms)**	**Delay (ms)**	**Number of pulses**	**Observations dispensed outcome**
100	100	100	100	1	2 droplets in quick succession
300	100	50	100	1	3 or 4 droplets in succession
150	100	50	100	1	2 droplets in quick succession
1	100	50	100	1	2 very small droplets in quick succession
100	300	50	100	1	± 6 droplets in succession. Rather a flow
100	150	50	100	1	± 6 droplets in succession. Rather a flow
100	1	50	100	1	1 droplet
100	100	3000	100	1	Flow of uncountable droplets
100	100	1000	100	1	± 10 droplets in succession. Rather a flow
100	100	1	100	1	2 small droplets in succession
100	100	50	1000	2	2 times 2 dispensed droplets with time in between the 2 cycles
1	1	1	100	1	1 very small droplet
1	0,6	1	100	1	1 very small droplet
300	300	3000	100	1	Flow of uncountable droplets

Table 9: Installed dispenser parameters and observations when dispensing was performed with a 1000 µm nozzle. The bold outlined columns indicate the applied method, namely the parameters are set to a minimum, an intermediate and a maximum value.

RT (ms)	**FT (ms)**	**OT (ms)**	**Delay (ms)**	**Number of pulses**	**Observations dispensed outcome**
5	1	5	100	1	1 very small droplet
5	5	5	100	1	1 small droplet
5	10	5	100	1	1 droplet
50	2	50	100	1	1 droplet
70	2	50	100	1	1 droplet
50	5	50	100	1	1 droplet
50	2	70	100	1	1 droplet
100	100	100	100	1	Flow of uncountable droplets
50	15	50	100	1	1 droplet
100	4	100	100	1	1 very thick droplet

Next, OT was first set to its maximum value of 3000 ms. This parameter-set resulted in an LBE flow. It was not possible to observe separate dispensed LBE droplets. When OT was decreased to 1000 ms, separate droplets instead of a flow were observed. It was not possible to count the number of separate droplets. This suggests that by decreasing open time, the dispensing volume decreases. When OT was set to its minimum of 1 ms, 2 small separate droplets in succession were observed.

Afterwards, delay was increased to 10 x the initial value. Differences in the dispensed droplets could only be observed when simultaneously increasing the number of pulses to 2, since delay is the time in between dispensed cycles. Increasing delay means increasing the time in between dispensed cycles.

The last three rows show results when RT, FT and OT first were all set to 1 ms, then all to their minimum values and lastly to their maximum values. When RT, FT and OT were all set to one and when RT and OT were set to 1 ms and FT to 0,6 ms, no difference could be seen with the naked eye. When all parameters were set to their maximum, a flow of uncountable droplets was dispensed because the droplet volume would probably have been too high to dispense in just one droplet. Also falling time was presumably not able to cut droplets out of the high dispensing volume.

Table 9 shows observations about the dispensed droplets with a 1000 µm nozzle opening. Setting RT to 5 ms, FT to 1 ms and OT to 5 ms resulted in one very small droplet being dispensed. When FT was increased to 5 ms and then to 10 ms, droplet sizes appeared to increase with increasing FT.

Next, RT was set to 50 ms, FT to 2 ms and OT to 50 ms. This parameter-set led to the dispensing of one LBE droplet. When RT was increased from 50 ms to 70 ms while the other parameters were kept the same, again, one single droplet was dispensed. Afterwards RT was set back to 50 ms and FT was raised from 2 ms to 5 ms. The parameters generated one LBE droplet. Lastly one droplet was dispensed again by decreasing FT back to 2 ms and by increasing OT from 50 to 70 ms. No difference between these generated droplets could be observed by the naked eye.

Because it was not possible to observe differences in the dispensed droplets, the RT, OT and FT were all together set to 100 ms. Now, a flow was observed instead of separate droplets. The falling motion of the tappet was not able to cut droplets out of the voluminous liquid metal jet.

Afterwards RT and OT were set to 50 ms and FT was set to 15 ms. This parameter-set contributed the dispensing of one LBE droplet. When lastly increasing RT and OT to 100 ms and setting FT to 4 ms, one very thick droplet was dispensed.

5.1.2 DROPLET SIZE DETERMINATION

For every parameter-set of Table 8 and Table 9, the dispensed volume was weighed. The parameter data of Table 8 are copied to Table 10 and of the parameter-sets of Table 9 to Table 11 and the columns droplet weight, droplet volume and droplet diameter are added.

Table 10: LBE droplet sizes for every parameter-set, dispensed with a 150 µm nozzle.

RT (ms)	**FT (ms)**	**OT (ms)**	**$m_{droplet}$ (g)**	**$V_{droplet}$ (ml)**	**$d_{droplet}$ (mm)**
100	100	100	0.0110	0.00105 ± 0.00001	1.26 ± 0.02
300	100	50	/	/	/
150	100	50	0.0180	0.00171 ± 0.00001	1.48 ± 0.01
1	100	50	0.0093	0.00088 ± 0.00001	1.19 ± 0.02
100	300	50	/	/	/
100	150	50	/	/	/
100	1	50	0.0152	0.00145 ± 0.00001	1.40 ± 0.01
100	100	3000	/	/	/
100	100	1000	/	/	/
100	100	1	0.0112	0.00106 ± 0.00001	1.26 ± 0.02
100	100	50	0.0139	0.00132 ± 0.00001	1.36 ± 0.01
1	1	1	0.0007	0.00007 ± 0.00001	0.50 ± 0.10
1	0,6	1	0.0102	0.00097 ± 0.00001	1.23 ± 0.02
300	300	3000	/	/	/
				Min	0.50
				Max	1.48

Remark: the deviation on the droplet mass is constant (± 0.0001 g).
'/' indicates that no separate droplets could be observed and therefore the average weight could not be calculated.

Table 11: LBE droplet sizes for every parameter-set, dispensed with a 1000 µm nozzle.

RT (ms)	**FT (ms)**	**OT (ms)**	**$m_{droplet}$ (g)**	**$V_{droplet}$ (ml)**	**$d_{droplet}$ (mm)**
5	1	5	0.0203	0.00193 ± 0.00001	1.54 ± 0.02
5	5	5	0.0621	0.00590 ± 0.00001	1.83 ± 0.03
5	10	5	0.1026	0.00975 ± 0.00001	2.65 ± 0.04
50	2	50	0.4137	0.03933 ± 0.00004	4.22 ± 0.06
50	5	50	0.4357	0.04142 ± 0.00004	4.29 ± 0.06
70	2	50	0.4607	0.04379 ± 0.00004	4.37 ± 0.06
50	2	70	0.5251	0.04991 ± 0.00005	4.57 ± 0.06
100	100	100	/	/	/
50	15	50	0.4136	0.03931 ± 0.00005	4.22 ± 0.04
100	4	100	0.9596	0.09122 ± 0.00009	3.87 ± 0.05
				Min	1.83
				Max	4.57

Remark: The deviation on the droplet mass is constant (± 0.0001 g)
'/' indicates that no separate droplets could be observed and therefore the average weight could not be calculated.

For parameter-set that generated more than one droplet, the mass of the dispensed volume was divided by the amount of counted droplet to obtain the average mass of the droplets. As previously mentioned, sometimes it was not possible to count separate droplets. For these droplets, the average weight could not be calculated.

The droplet volume was calculated through the weight and the density of LBE. Equation (17) was used to determine the droplet volume.

$$V = \frac{m}{\rho_{LBE}} \tag{17}$$

The density of LBE [4] at 160 °C was calculated as following:

$$\rho_{LBE} = 11096 - 1.323\,T$$

$$\leftrightarrow \rho_{LBE} = 10{,}522 \text{ kg/m}^3$$

Lastly, the radius of the dispensed droplets was calculated by the volume of the dispensed liquid. Herefore, the equation (18) of the volume of a sphere was used, assuming the droplets have a spherical shape.

$$V_{sphere} = \frac{4}{3}\,\pi\,r^3 \tag{18}$$

Applying these equations to the first row or Table 3:

$V = \frac{m}{\rho_{LBE}} \leftrightarrow V = \frac{0.0110 \pm 0.0001\ g}{10.52 \pm 0.01\ \text{g}/cm^3}$ = 0.00105 ± 0.00001 cm^3

The uncertainty [65] was calculated using the formula below:

$$\delta_v = 0.00105\sqrt{(\frac{0.0001}{0.0110})^2 + (\frac{0.01}{10.52})^2} = 0.00001$$

The droplet diameter is obtained from its volume:

$$V = \frac{4}{3}\,\pi\,r^3$$

$$\leftrightarrow 0.00105 \pm 0.00001 = \frac{4}{3}\,\pi\,r^3$$

$$\leftrightarrow \text{r} = 0.06305 \pm 0.0008 \text{ cm and thus d} = 1.26 \pm 0.02 \text{ mm}$$

The uncertainty on the radius was calculated with:

$$\frac{0.00001}{0.00025} = 3\left(\frac{\delta_r}{0.0631}\right) \leftrightarrow \delta_r = 0.0008$$

The uncertainty on the diameter was calculated with:

$$\delta_v = 1.26\sqrt{(\frac{0.0008}{0.06305})^2} = 0.02$$

The LBE droplet dispensed with the parameter-set in row 1 of Table 10, namely; cartridge temperature 160 °C, nozzle temperature 170 °C, valve cooling 60 °C, needle lift 70%, RT 100 ms, FT 100 ms, OT 100 ms, delay 100 ms, number of pulses 1 has a diameter of 1,26 ± 0.02 mm.

All other diameters were calculated likewise. The smallest dispensed droplet with a 150 µm nozzle was generated by setting parameters RT, FT and OT to 1 ms. The droplet has a diameter of 0.50 ± 0.10 mm.

The largest separate dispensed droplet with a 150 µm nozzle was obtained by setting RT to 150 ms, FT to 100 ms, OT to 50 ms and has a diameter of 1.48 ± 0.01. This parameter-set generated two small droplets in succession. The weight of the total dispensed volume was determined. The weight reported is that averaged over the number of droplets, namely 2.

Parameter-set (1 ms RT, 0.6 ms FT and 1 ms OT) led to a droplet with 1.23 ± 0.02 mm diameter, much larger than expected using these small parameter values. It is unclear why the dispensed droplet was not smaller.

The observations made about the dispensed droplets in Table 8 can be supported by the droplet weights. It was assumed that increasing open time OT increased the dispensed droplet volume. Using RT = 150 ms generated droplets with a (separate) diameter of 1.48 ± 0.01 mm, while 1 ms RT led to a droplet with 1.19 ± 0.02 mm diameter. When the parameter FT was decreased, it could be observed that the tappet was able to create more separate droplets. But no uniform effect of the falling time on the droplet size can be made. For the other parameter-sets, the observations could not be correlated with the measured droplet sizes as the droplet diameters could not be determined.

Table 11 illustrates the dispensed droplet's weight, volume and diameter when dispensing with a 1000 µm nozzle, using the parameter data of Table 9. The same equations as above were used to calculate the size of the droplets. In the first three rows, the results of the droplet weight can be seen when varying FT from 1 ms to 5 ms and finally to 10 ms. The droplet diameter increases with increasing FT. Keeping RT and OT at 5 ms, while increasing FT from 2 ms to 5 ms leads to an increase in the droplet size. These results are contractionary to the previous. Also, when comparing the row displaying RT-FT-OT 50-5-50 to the penultimate row displaying 50-15-50, the diameter decreases 66 % with increasing FT.

The smallest generated droplet with a 1000 µm nozzle was dispensed by setting RT to 5 ms, OT to 5 ms and FT to 10 ms. The droplet has a size of 1.83 ± 0.03 mm.

The largest dispensed droplet was 4.57 ± 0.06 mm and was obtained by setting RT to 50 ms, OT to 2 ms and FT to 70 ms with a nozzle opening of 1000 µm.

The parameter-set with an RT, FT and OT of 100 ms generated an LBE flow instead of separate droplets. Therefore, no average weight could be calculated.

5.1.3 PRECISION OF THE DISPENSER

The precision of the dispenser is calculated to see whether it is possible to repeat precise parameter-sets for future experiments in this thesis. The precision of the dispenser device is a measure of how widely the droplet weight values are distributed around the average weight. It is determined from repeated dispensed droplets, obtained by using the same parameter-set. The spread is caused by accidental errors, characteristic for the dispenser device [65]. The standard deviation of the Vermes dispenser was determined by dispensing droplets using a parameter-set with high values (300 ms RT, 3000 ms OT, 300 ms FT) and a set with low values (1 ms RT, 1 ms OT, 1 ms FT). For every parameter-set, 8 droplets were dispensed in succession. The mass of every droplet is shown in Table 12.

Table 12: Precision of dispensed LBE droplets

RT - FT - OT	$m_{droplet}$ (g)	$V_{droplet}$ (ml)
1 - 1 - 1	0.0008	0.00008 ± 0.00001
	0.0008	0.00008 ± 0.00001
	0.0007	0.00007 ± 0.00001
	0.0007	0.00007 ± 0.00001
	0.0009	0.00009 ± 0.00001
	0.0005	0.00005 ± 0.00001
	0.0005	0.00005 ± 0.00001
	0.0007	0.00007 ± 0.00001
Average	0.0007	
stdev.s	0.0001	
CV	**14.3 %**	

Remark: The deviation on the droplet mass is constant (± 0.0001 g)

RT - FT - OT	$m_{droplet}$ (g)	$V_{droplet}$ (ml)
300 - 300 - 3000	0.5541	0.0527 ± 0.00005
	0.5590	0.0531 ± 0.00005
	0.5462	0.0519 ± 0.00005
	0.5522	0.0525 ± 0.00005
	0.5577	0.0530 ± 0.00005
	0.5604	0.0533 ± 0.00005
	0.5568	0.0529 ± 0.00005
	0.5531	0.0526 ± 0.00005
Average	0.5549	
stdev.s	0.0016	
CV	**0.29%**	

Remark: The deviation on the droplet mass is constant (± 0.0001 g)

The uncertainty of the volume in row 1 was calculated with:

$$\delta_v = 0.00008\sqrt{(\frac{0.0001}{0.0008})^2 + (\frac{0.01}{10.52})^2} = 0.00001$$

Precision is determined by a statistical method: the standard deviation, calculated by formula (19) [65].

$$s = \sqrt{\frac{\sum_{i-1}^{N}(x_i - \mu)^2}{N-1}} \tag{19}$$

The droplet, obtained by the smallest parameter-set (1 ms RT, 1 ms FT and 1 ms OT) resulted in a droplet with an average weight of 0.0007 ± 0.0001 g. This corresponds with a coefficient of variation (CV) of 14.1 % and indicates that the range of the analytical balance available was rather high for such small droplets. The CV decreases to 0.29 % when a parameter-set with higher parameter values is used [65].

5.2 Troubleshooting

Several technical difficulties occurred during the liquid impingement experiments with the high-speed camera. To determine the particle size distribution of aerosols formed by LBE droplet splashing, a properly functioning setup generating reproducible droplets is required. This was not the case; the obstacles encountered are discussed here to help solving these issues to facilitate further research.

5.2.1 CARTRIDGE EXPANSION

Before starting the dispensing cycle, the dispenser's cartridge needs to be filled with the desired dispensing fluid. As the cartridges are open at the bottom, a rubber stopper is used to seal the bottom during filling. The cartridge is filled with liquid LBE by opening the tap of the HELIOS3 LBE tank. After filling, the cartridges are left to cool to room temperature to solidify. After a day, the cartridge is ready to be inserted into the dispenser's cartridge holder.

However, due to expansion of the LBE during solidification, the walls of some of the cartridges were pushed outwards and thereby preventing the insertion into the dispenser's cartridge holder. This was overcome by fitting the cartridges in a home-made stainless-steel holder during filling and cooling. The inner diameter of the holder is the same as the outer diameter of a fitting dispenser cartridge. The holder is illustrated in Figure 19.

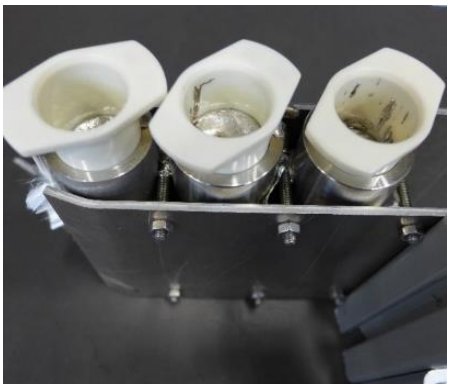

Figure 19: Cartridge holder.

5.2.2 BLOCKED FLUID BOX BODY COMPONENTS

Before dispensing, the device requires an adjust procedure. During the adjust, the tappet is positioned correctly relative to the nozzle. To perform the adjust, an LBE cartridge is placed into the cartridge holder of the dispenser and heated to 160 °C. After 20 minutes, the cartridge and fluid box were assumed to have reached their temperatures. To adjust the dispensing system, first the adjustment screw needs to be screwed completely open and then screwed inwards from value ‘’-40 %” to in between 0 % and 1 %. The value fluctuated up and down from -40 % to -38 % but did not go further towards 0 %. The adjustment screw felt completely fixed. For this reason, the dispenser's components (except for the valve) and the MDC were sent back to the company and spare parts were sent in return.

According to the error rapport of the company, the tappet was unable to move inside the fluid box body because it got blocked by solidified LBE. Figure 20 shows pictures of the stuck dispenser components.

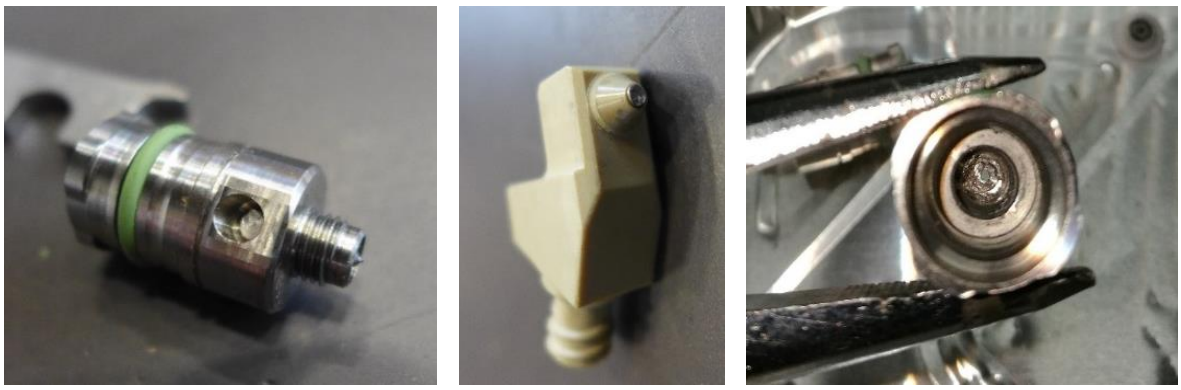

Figure 20: Dispenser parts blocked with solidified LBE. From left to right: LBE stuck in the opening of the lower part of the fluid box body; in the cartridge base; in the nozzle opening.

The company pointed out the necessity to clean the complete system from LBE after every cool down or switch off action. For this research work, dispensing was to be performed with 2 nozzle openings. Therefore, every time the nozzle needs to be replaced, the dispenser needs to be cooled and cleaned. This also means that the device requires an adjust after every cleaning process.

Knowing this, it was attempted to empty the dispenser components from LBE by reheating the assembled dispenser to 160 °C and forcing the tappet to open by pressing the 'F1' button on the MDC. It is still unclear why, but after waiting 1 hour still no LBE was dispensed. Therefore, the dispenser was cooled down and completely disassembled. It was possible to disassemble the large parts, but it was not possible to disassemble the nozzle, the sealing nor the tappet from the fluid box manually.

The first attempt to remedying this was to submerge the complete fluid box, cartridge base and hollow screw in LBE cleaner liquid. Even after submerging all parts a second time in 'fresh' cleaner liquid, it was still not possible to disassemble the parts. This meant that the cleaner was not able to handle great amounts of LBE or its associated deposits. After flushing the particles with demineralized water, the second attempt implied using a heat gun set at 180 °C to heat all deposits manually to liquefy the LBE. After some time, the stuck LBE dripped out. By pushing stuck LBE out using an ear stick, it was eventually possible to disassemble the dispenser. The components were submerged once again in the LBE cleaner to erase the remaining LBE particles and oxides from the components. This time, the cleaner was able to clean all remaining stuck LBE. Finally, the components were flushed with demineralized water and air-dried before re-assembly.

Considering the time-consuming manual cleaning procedure, it would be more convenient to flush the dispenser while assembled. Because the LBE cleaner cannot be heated, PUR hotmelt cleaner - recommended by Vermes - was purchased and found to be a suitable candidate. For this cleaning method, first the LBE cartridge needs to be taken out of the heated and assembled dispenser and switched with a PUR hotmelt cleaner cartridge. Since liquid LBE can flow freely out of the open end at the bottom of the cartridge, the latter needs to be cooled to 120 °C to solidify its content. During this procedure, the connection from cartridge to fluid box, i.e., the cartridge base solidified most of the time as well. Therefore, when the PUR hotmelt cleaner cartridge was inserted in the system and heated to 170 °C, the PUR cleaner could not flow through because of the blocked cartridge base. This meant the dispenser needed to be disassembled and cleaned anyway by the above-mentioned manual cleaning procedure. The latter method is therefore preferred. When the LBE cartridge is empty, it can easily be taken out of the cartridge holder using safety gloves and replaced by a PUR hotmelt cleaner cartridge. The cartridge was heated to 170 °C and compressed air (0.5 bar) was connected to the cartridge. After some waiting time, the 'F1' valve opening button on the MDC was pressed. The PUR hotmelt cleaner flowed through the system and dissolved the stuck LBE.

Cleaning can thus be done using PUR hotmelt cleaner only for empty LBE cartridges. In all other case, the manual cleaning procedure needs to be used.

5.2.3 LEAKING DISPENSER

The correlation between droplet diameter and dispenser parameter-settings (section 5.1) was analyzed while the dispensing system was assembled and placed ex-situ from the experimental SPLAT setup. During the ex-situ tests, the dispenser functioned as desired.

To determine the Weber number and splashing forms of the impinging droplets with a high-speed camera, the dispenser needs to be placed into its custom-made enclosure, located at the top of the SPLAT setup. From this stage on, the dispenser started to show leaking problems, which greatly hindered the remainder of the experiments. In this part we try to describe the steps undertaken to solve this problem.

To mount the dispenser on the SPLAT setup, the dispenser was turned off and cooled down and moved from the table to the top of the setup. After mounting, when the dispenser was instructed to dispense, no droplets were dispensed. According to the dispenser's manual, this problem could be caused by a broken sealing. To check this, the dispenser was left to cool down to room temperature, disassembled and cleaned using a heat gun instead and LBE cleaner instead of the PUR cleaner. After cleaning, the components were air-dried and the dispenser was assembled again. No damage to the components was observed.

Before testing the dispenser in the SPLAT setup a second time, the adjust procedure was performed on the ex-situ setup. The dispenser was then moved from the table to the top of the SPLAT setup again. This time, the cartridge was not cooled before moving it, thus the LBE was liquid. While the dispenser was moved from the table to the setup, the dispenser started leaking. The entire cartridge content leaked out. Hereafter, the dispenser was cooled and cleaned again. It was assumed that the leak is caused by the inability of the tappet to prevent the moving LBE from entering the dispensing chamber, due to the fluid motion. But it seems odd that the dispenser would not be able to bear movements since the dispenser is used on a fast-moving x-y stage in several industrial applications.

To avoid any fluid motion, the dispenser was assembled and inserted directly on top of the SPLAT setup. The dispenser was fitted with a 1000 µm nozzle opening. First, the MFC was turned on. The cartridge and fluid box heater were heated to 160 °C and the piezo was cooled to 60 °C. The supply pressure was turned on to 3 bar. The LBE started flowing out again. This indicated the presence of a leak or that the tappet was not closing properly. The tappet is controlled by the MDC, which is a 'normally open' system. This means that when the MDC is switched off, the tappet is in an upward position. Knowing this, the MDC was switched off and on to make the tappet move from up to down to stop the leakage. Contrary to the expectations, this did not happen. The dispenser continued leaking. This indicated that the tappet was not able to move inside the fluid box body. But, when the dispenser was instructed to dispense droplets, the requested droplets were dispensed in between the leaking droplets. This indicated that the tappet was able to move up and down and was not stuck. In view of these observations, it was assumed that the tappet was not able to completely close the nozzle or that the MDC signals were not received by the piezo.

To check the second assumption, all the dispenser's connections were checked. This trial and error showed that the compressed air connections of the dispenser were connected incorrectly. The gas supply was connected to the flow control valve. The output of the flow control valve was connected to the cartridge lid instead of to the compressed air adapters on the valve to cool the valve. Thus, this indicated that the 3 bar argon gas supply pressure was sent to the cartridge content. It was assumed that this forced the LBE to move towards the dispensing chamber. The tappet would not have been able to hold back the LBE flow, arriving at the nozzle opening with 3 bar pressure. But this explanation could not be correct as it turns out that the flow control valve requires 6 bar pressure to open. This means that no pressure arrived at the cartridge lid at all. Because of the incorrect connections, the valve was thus not cooled. The temperature of the valve was set to 60 °C using the MFC. When the valve would reach temperatures over 60 °C, the flow control valve gets a signal to open and the 6 bar argon gas then arrives at the flow control valve. But even without cooling, the piezo's temperature never exceeded 61 °C, as indicated by the MFC's display.

As the piezo can handle temperatures up to 80 °C, 61 °C could not pose a problem and cooling of the valve is not required for our application. For these 2 reasons, the wrongly connected connections cannot be the cause of the leaking problem.

LBE's high density is a second reason why the incorrect connections could not cause the leakage. LBE's viscosity is low (0.0030 Pa·s at 140 °C) and LBE's density is high (10,548 kg/m³ at 140 °C). According to the micro dispenser's manual, low viscosity fluids require 0.5 bar cartridge supply pressure. Due its high density, LBE will be able to move downwards by itself and thus not require any supply pressure to move downwards towards the nozzle fluid box body.

A further assumption was that the tappet was not able to seal the nozzle insert against the pressure, exerted by the LBE column in the LBE cartridge. To counteract this, the cartridge's gas supply connection was blocked using a plug to create an under pressure. The leaking continued but was observed to slow down in time. At last, the leakage stopped when the cartridge was only filled up to 20 %. When the MDC was now instructed to dispense a droplet, the dispenser seemed able to dispense the requested droplets. During the high-speed camera test, an under pressure was reached when the cartridge was 80 % empty. From the results it is observed that during these experiments, the droplet diameter decreased owing to the under pressure.

During the high-speed camera experiments, it seemed that the temperature had an influence on the leakage as well. To decrease the frequency with which droplets were released due to leakage, the cartridge base and fluid box body were lowered degree by degree. After some time, the leakage slowed down. Altogether, the cartridge temperature was lowered from 160 °C to 139 °C and the fluid box temperature was decreased from 170 °C to 143 °C. The leakage remained but the frequency lowered to a workable frequency. This may point to the influence of the liquid's viscosity, plotted in function on temperature in Figure 21.

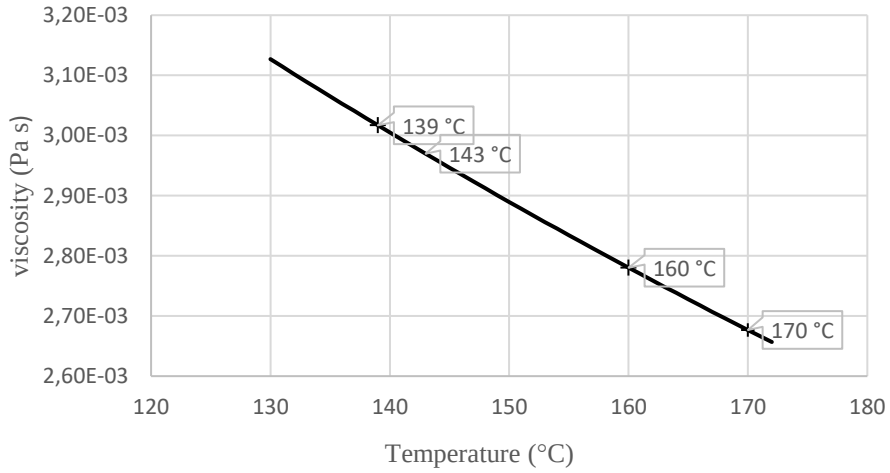

Figure 21: Viscosity of LBE in function of temperature.

The viscosity of LBE increases from 2.79E-03 Pa·s at 160 °C to 3.02E-03 Pa·s at 139 °C (cartridge temperatures) and from 2.68E-03 Pa·s to 2.97E-03 Pa·s (fluid box temperatures) [4]. Such small differences are not expected to significantly affect the viscosity of the liquid LBE.

As the leaking frequency was observed to be better controllable when the temperatures of the dispenser were lowered, the cartridge box and fluid box temperatures were lowered to 140 °C and to 145 °C. Furthermore, the 1000 µm nozzle was replaced with a 150 µm nozzle, as decreasing the nozzle diameter should show a favorable impact on the leaking if it was LBE weight related. When dispensing with a 150 µm nozzle, no leakage was observed from the start. During previous experiments with the 1000 µm nozzle insert, leakages already occurred while dispensing had not started yet.

When the MDC was now instructed to dispense droplets, the droplets were indeed dispensed. However, they were accompanied by a flow of residual LBE. The temperature of the cartridge was lowered to 138 °C and the fluid box to 140 °C to stop the leakage. At some point, the leakage stopped but no droplets could be dispensed. Since the nozzle has an opening of only 150 µm, it was assumed that the nozzle was blocked. To get rid of the blockage, the fluid box temperature was increased from 140 °C to 143 °C, to 145 °C and eventually to 150 °C. When the dispenser was instructed to dispense again, at some point an LBE flow developed all at once. It was assumed that the blockage was removed and that the assembled LBE poured out all at once. This blocking – unblocking process happened repeatedly.

When Vermes was contacted about the problem, they asked about the condition of the tappet. A microscope was used to see if micro cracks were present. These images are shown in Figure 22. Neither the 1000 µm, nor the 150 µm nozzle showed damage, according to our observations. The tappet tip seemed not greatly damaged at first. Some damage was observed in the middle of the tappet, near the location of the seals. However, according to the company, the small damages at the tip were causing the problem. The damaged tappet tip was in their view not able to ensure the tightness between nozzle and tappet. According to the company, the tappet was heavily used. The tappet was however used for only a limited amount of test. Therefore, it seems odd that the tappet was already damaged after approximately 8 to 10 dispensing cycles.

Figure 22: Microscopy images of the tappet rod tip.

To confirm whether the leaking was caused by the damaged tappet, a new tappet and nozzle were assembled. The dispenser continued leaking.

Regarding the fact that most dispenser components were replaced with new components, except for the valve, it could be possible that the lever or piezo are causing the leaking. But this was not possible to check within the time scale of this thesis work.

Altogether, it is not possible to give one unambiguous cause for the leaking dispenser. Presumably, the leaking is caused by a combination of several factors such as the high density of LBE and the sensitivity of the dispenser at high temperatures. Since the differences in viscosity between the applied temperatures are insignificant, the viscosity of LBE is not considered as contributor to the leakage. To confirm whether the valve is causing the leakage, the valve should be sent back to the company for further research.

To conclude, we were unable to solve the cause of the dispenser leakage in the time frame of this thesis work. However, we managed to device a procedure that reduced the leakage sufficiently to allow performing the high-speed camera experiments and PSD measurements, presented in the next sections.

5.3 High-speed camera results of liquid impingement

Because leaking appeared, it was not possible to reproduce the preconceived parametrical study in section 3.2, nor the conditions as applied in all previous experiments in 5.1. During previous experiments, a cartridge temperature of 160 °C and a fluid box body temperature of 170 °C were applied, while lower temperatures were used during this high-speed camera study. For the current experiments in this section, it was attempted to decrease the leaking frequency during the experiments by creating an under pressure. It was therefore not possible to reproduce the predefined droplet sizes, since no under pressure was created then. Deviations from the experimental survey can thus be explained by the technical difficulties that appeared during the current experiments compared to the parametric study.

5.3.1 WEBER NUMBERS AND IMPACT VELOCITIES

Table 13 and Table 14 list the results of the liquid impingement study, for a 1000 µm (Table 13) and a 150 µm nozzle (Table 14), analyzed with a high-speed camera.

Liquid impingement was first studied with LBE droplets using a 1000 µm micro dispenser nozzle, colliding onto two surfaces. To generate the droplets, the same parameter-set was used for all, namely 5 ms RT, 1 ms FT, 5 ms OT, 70 % needle lift, one single pulse, ± 140 °C cartridge temperature (varying), ± 145 °C fluid box temperature (varying). This parameter-set is estimated to generate an LBE droplet of 1.54 mm diameter, based on section 5.1. Every droplet in Table 13 is provided with an ID number (experiment number - nozzle, surface), illustrated in column 1. In column 2, the impacting velocity is given, while in column 3-5, the diameter of each drop is shown. The velocity and diameter are derived by MATLAB processing of the high-speed recordings. Because not all droplets were spherical, the droplet size could not be determined precisely with MATLAB. Therefore, a droplet diameter range was calculated instead. The Weber number is calculated through equation (2) and noted in column 6. Additionally, a screenshot of the impact is added in the last column with a short description. The descriptions are based on the video recordings of the high-speed camera. When secondary ejected droplets or clear crown or prompt splash forms were seen, ‘splash’ was noted since secondary ejected droplets indicated splashing. When no visible secondary droplets were observed on the video recordings, or when a clear spread-out droplet was observed, ‘splash’ was added as image-description. The orange bordered images are further discussed in this section and in section 5.3.2.

As can be seen in Table 13, the impact velocity of the droplets impinging the liquid and dry surface using a 1000 µm nozzle is in between 2.45 and 2.53 m/s. The most common velocity is 2.48 m/s. The impact velocities are slightly lower than expected in the experimental parametric survey section 3.2. Droplets with a diameter of 1.5 mm diameter were expected to have a velocity of 2.73 m/s at 40 cm fall height; for a droplet of 3 mm diameter this was 2.74 m/s. The difference between the expected velocity and the actual impact velocities can be explained by the effective travelled distance and by the droplet shape. During the experiments, both the liquid and solid impacting surface were raised to align the camera’s lens with the surface. For this reason, the travel distance of the droplet is lower than the travelled distance used in the equations of the velocity estimations. Moreover, the droplet shape influences the drag between the droplet and the fluid through which the droplet travels. Another explanation for the deviating impacting velocities may be the applied under pressure during these experiments to solve the leaking. This may impact the shape of the dispensed droplets and thus also the drag coefficient.

The first droplet (1-1000L) of Table 13 is determined to have a diameter between 1.38 and 1.90 mm diameter. This droplet 1-1000L is the smallest generated by the parameter-set with an average diameter of 1.64 ± 0.37 mm, compared to the other droplets in Table 13. As already explained, owing to the deviating droplet shapes, no accurate droplet size could be determined.

Table 13: High-speed camera results using the dispenser with a 1000 µm nozzle. The orange bordered images indicate tests that will be further discussed.

ID	v_{impact} (m/s)	d_{min} (mm)	d_{max} (mm)	$d_{average}$ ± stdev (mm)	Weber ± stdev	Impact image and description (splash or spread: type)
Liquid surface impingement						
1-1000L	2.48	1.38	1.90	1.64 ± 0.37	260 ± 58	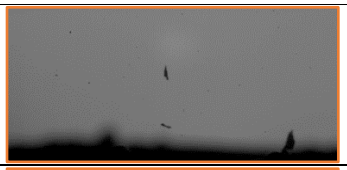 Splash: unclear
2-1000L	2.48	2.73	3.59	3.16 ± 0.61	499 ± 98	 Splash: crown
3-1000L	2.48	2.82	2.82	2.82 ± 0.00	445 ± 11	 Splash: crown
4-1000L	2.49	2.68	3.02	2.85 ± 0.24	454 ± 41	 Splash: crown
5-1000L	2.50	2.56	2.69	2.62 ± 0.10	424 ± 19	 Splash: crown
6-1000L	2.48	2.34	2.53	2.44 ± 0.14	386 ± 24	 Splash: crown
7-1000L	2.45	2.52	2.99	2.75 ± 0.33	425 ± 53	 Splash: crown
Dry solid surface impingement						
8-1000D	2.53	2.36	2.36	2.36 ± 0.00	389 ± 10	 Spread: lamella
9-1000D	2.53	2.48	2.71	2.60 ± 0.16	429 ± 28	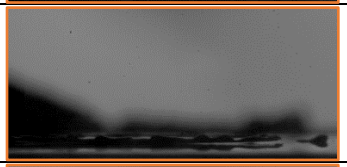 Spread: lamella
10-1000D	2.53	2.49	2.62	2.56 ± 0.99	423 ± 19	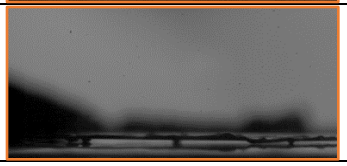 Spread: lamella

The falling droplets were not spherical and the MATLAB code was not able to correct for this deviation. Some falling droplets showed ‘’arms’’ while others are spherical, as shown in Figure 23. Furthermore, it may also be that for some drops the ‘’arm’’ was visible at the back of the drop in relation to the camera. The ‘’arm’’ was in this case not visible on the recordings and therefore not included in the count. In this case, the calculated size will deviate from the real drop size.

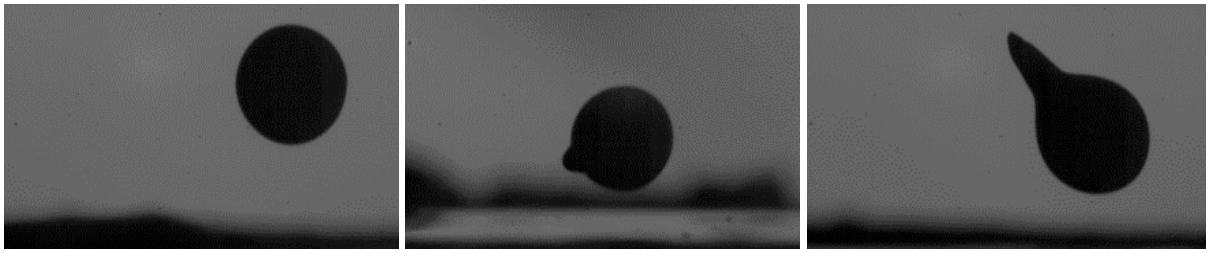

Figure 23: Images of specific falling droplets with deviating drop shapes.

The calculated diameters of the droplets obtained in the SPLAT setup differ from the ones obtained by weighing the droplets (section 5.1) ex-situ when using the same parameter-sets. This is related to the troubles with leakages that had to be dealt in the SPLAT setup, as described in section 5.2.3.

The first droplet with diameter 1.64 ± 0.37 mm has a similar impact velocity as the other droplets, but as it has the smallest diameter this also leads to the smallest Weber number as calculated with equation (2):

$$We = \frac{\rho\, v^2 d}{\sigma}$$

$$\leftrightarrow We = \frac{10.55 \pm 0.01 \frac{g}{cm^3} .\ 2.48^2\ m/s\ .\ 1.64 \pm 0.37\ mm}{0.41 \pm 0.01\ N/m} = 260 \pm 58$$

The uncertainty is calculated with:

$$\delta_{We} = 260 \sqrt{(\frac{0.01}{10.55})^2 + (\frac{0.37}{1.64})^2 + (\frac{0.01}{0.41})^2} = 58$$

Because the Weber number of the 1-1000L droplet is lower than the other Weber numbers in Table 13, this droplet is expected to show less splashing than others. The other droplets in Table 13 showed higher Weber numbers from 386 up to 499. The second droplet 2-1000L with diameter 3.16 ± 0.61 mm shows a high Weber number of 499 ± 98, but had a similar impact velocity as droplet 1-1000L.

The impact images illustrate that the first 1-1000L drop generates secondary ejected droplets but is not clear whether prompt of crown splash occurs. Droplet 2-1000L till 7-1000L all generate splashing and more specific crown-splash. Because droplets 1-1000L and 2-1000L are outliners (i.e. the smallest droplet and the largest droplet of Table 13), these high-speed camera images are discussed further and are therefore marked with a dashed line. Recording 4-1000L will also be further discussed as ‘intermediate’ to compare with.

The three last rows of Table 13 illustrate the results of dry solid surface impingement with a 1000 µm nozzle. During these tests, the same parameters were used and therefore no changes in Weber number are expected. As can be seen in Table 13, the Weber numbers of the LBE droplets indeed also lie around 389 up to 429. According to the parametric survey (5.1), the Weber numbers of LBE droplets with 2.5 mm diameter were expected to be between 255 when falling with a speed of 2 m/s and 573 when falling with a speed of 3 m/s. The Weber number of the impinging droplets are thus within expectations.

The droplets impacting the dry solid surface show spreading instead of splashing. Droplets 8-1000D shows a hollow-formed lamella, while 9-1000D and 10-1000D show flat lamellae. The high-speed camera video recordings showed that lamella 9-1000D and 10-1000D separated from the surface. All 3 dry solid surface droplet impact images are bordered as they will be discussed in section 5.3.2.

Table 14 illustrates similar high-speed camera results as Table 13 but using a 150 µm nozzle instead of a 1000 µm nozzle. All droplets are generated with the same dispenser parameter-set; 1 ms RT, 0.6 ms FT, 1 ms OT, one single pulses, 138 °C cartridge temperature (varying), 144 °C fluid box (varying), 70 % needle lift. The velocity, diameter and Weber number are calculated analogue as those of Table 13.

Table 14: High-speed camera results, using the dispenser with a 150 µm nozzle. The orange bordered images indicate tests that will be further discussed.

ID	v_{impact} (m/s)	d_{min} (mm)	d_{max} (mm)	$d_{average}$ ± stdev (mm)	Weber ± stdev	Impact image and description (splash or spread: type)
Liquid surface impingement						
1-150L	2.44	0.96	1.08	1.02 ± 0.09	156 ± 14	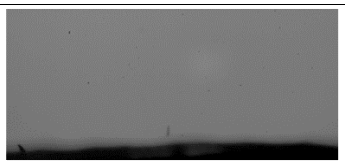 Splash: unclear
2-150L	2.44	0.88	0.94	0.91 ± 0.04	139 ± 7	No splash
3-150L	2.43	0.93	1.72	1.32 ± 0.56	201 ± 85	 Splash: unclear
4-150L	2.46	0.92	0.96	0.94 ± 0.03	146 ± 6	 Splash: unclear
5-150L	2.41	0.94	1.48	1.21 ± 0.38	181 ± 58	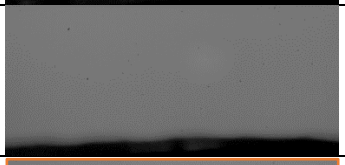 Splash: unclear
6-150L	2.44	0.84	1.15	1.00 ± 0.22	152 ± 34	 Splash: unclear
7-150L	2.41	0.81	1.00	0.91 ± 0.13	135 ± 20	No splash
8-150L	2.40	0.85	1.10	0.98 ± 0.18	144 ± 27	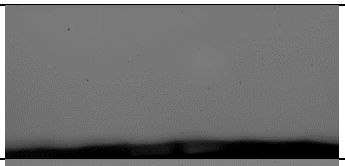 Splash: unclear
9-150L	2.38	0.81	0.78	0.79 ± 0.02	115 ± 4	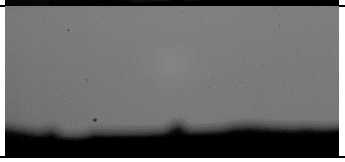 Splash: unclear
10-150L	2.43	0.84	1.39	1.12 ± 0.39	170 ± 60	No splash
11-150L	2.39	0.82	1.10	0.96 ± 0.20	140 ± 29	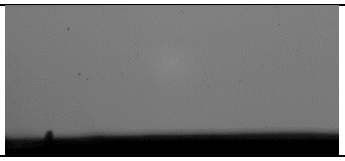 Splash: unclear

ID	v_{impact} (m/s)	d_{min} (mm)	d_{max} (mm)	$d_{average}$ ± stdev (mm)	Weber ± stdev	Impact image and description (splash or spread: type)
12-150L	2.42	0.95	1.12	1.03 ± 0.12	156 ± 18	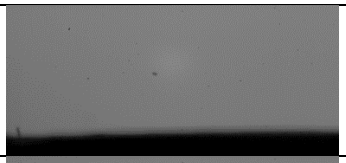 Splash: unclear
13-150L	2.41	0.83	1.08	0.95 ± 0.17	142 ± 26	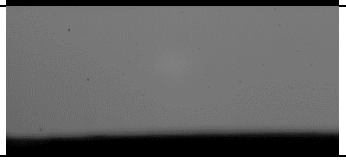 Splash: unclear
Dry solid impacting surface						
1-150D	2.49	1.35	1.71	1.53 ± 0.25	244 ± 40	 Leakage built-up
2-150D	2.52	1.13	1.20	1.17 ± 0.05	189 ± 9	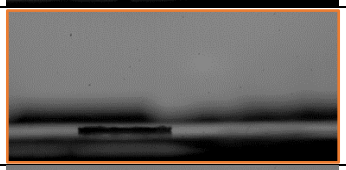 Spread: lamella
3-150D	2.00	1.29	1.61	1.45 ± 0.23	150 ± 24	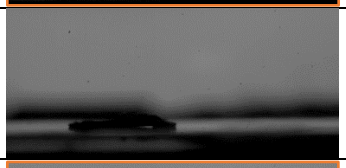 Spread: lamella
4-150D	2.44	1.21	1.60	1.41 ± 0.28	216 ± 43	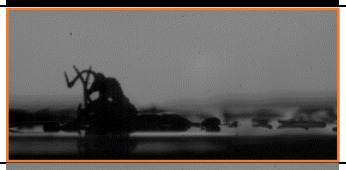 Leakage built-up
5-150D	1.82	1.07	1.08	1.08 ± 0.00	91 ± 2	 Leakage built-up

13 liquid impingements on a liquid surface and 5 on a dry solid surface were performed and measured in the SPLAT when using the 150 µm dispenser's nozzle. The impact velocity of the droplets should be quite similar for the liquid and dry solid surface collisions, since only the surface has changed. The impact velocity of the droplets of Table 14, which are dispensed with 1 ms RT, 0.6 ms FT and 1 ms OT using a 150 µm nozzle, vary from 1.82 to 2.52 m/s. The most occurring velocity is 2.44 m/s. According to the parametric survey (section 3.1), LBE droplet of 0.5 mm diameter falling from 40 cm height were expected to have impact velocities of 2.65 m/s and 2.73 m/s for droplets of 1.5 mm diameter. The impact velocities are again less than expected. This can also be explained by deviations of the spherical shape - induced by conditions under which the droplets are released from the dispenser – and of the effective travel distance – which is related to the alignment of the camera and the impact surface.

Section 5.2.3 illustrated that the created under pressure in the cartridge was not reached from the beginning but was reached over time, when the cartridge was only ± 30 % full. During the high-speed camera experiments of Table 14, the dry solid surface results were recorded first (i.e. droplet 1-150D – 5-150D). The droplet diameters for the dry solid surface are higher than the droplet diameters of the latter liquid surface experiments (1-150L-13-150L). During the experiments, one LBE cartridge was sufficient to do all the measurements. Thus, when the experiments started, the cartridge was full. Over time, the cartridge emptied because of the dispensing. When replacing the dry solid surface with a liquid surface, the leaking continued. Thus, the cartridge emptied even further.

By the time the liquid surface experiments started, it is presumed that the under pressure was achieved. The difference in droplet diameter between the dry solid and liquid surface can therefore be explained by the under pressure, making it harder for the LBE to flow through the system.

The Weber numbers for the 150 µm LBE drops range from 91 up to 244. According to section 5.1, droplets of 1 mm diameter were expected to have Weber numbers of 102 when falling with an impact velocity of 2 m/s and a Weber of 229 when falling with a velocity of 3 m/s. The experimental Weber numbers thus agree with the expected Weber numbers. Because the Weber numbers of droplets dispensed with a 150 µm nozzle are lower than the Weber numbers of droplets dispensed with a 1000 µm nozzle, less splashing is expected.

The impacting velocities of the droplets is Table 13 (1000 µm nozzle) and Table 14 (150 µm nozzle) are quite similar to each other. This indicates that the differences in parameter-sets used for the 1000 µm nozzle (5 ms RT, 1 ms FT, 5 ms OT) and for the 150 µm nozzle (1 ms RT, 0.6 ms FT and 1 ms OT) do not have great influence on the droplet velocity.

When secondary ejected droplets were seen on the camera's video recordings, 'splash' was noted next to the high-speed camera images in Table 14. The splashing form was not always clear since the surface could not always be seen in sufficient detail. For this reason, some images are described as 'unclear', since the impacting form could not be determined exactly.

Droplet 2-150L, 7-150L and 10-150L showed no visible created secondary droplets. The Weber numbers for droplet 2-150L and 7-150L are both below 140, namely 139 ± 7 and 135 ± 20 and their diameters are 0.91 ± 0.04 mm (2-150L) and 0.91 ± 0.13 mm (7-150L). It was therefore assumed that these droplet parameters could indicate a threshold. But, droplet 9-150L has an even lower Weber number (115 ± 4), lower diameter (0,79 ± 0.02 mm) and lower velocity (2,38 m/s) and did generate secondary droplets. Moreover droplet 10-150L with 2,43 m/s impacting velocity, 1,12 ± 0.39 mm diameter and Weber number 170 ± 60 showed, contrary to the expectations, no splashing or ejected particles. Therefore, it may be assumed that the splashing for some droplets, like 2-150L, 7-150L and 10-150L are not recorded with the high-speed camera, possibly because the liquid surface did not reach the edge of the stainless-steel tray. Droplet 3-150L has the highest Weber number and highest diameter of all droplets of Table 14. This droplet showed the clearest crown-splash form. This points out to the influence of the Weber number on splashing.

The recorded droplets 3-150L and 6-150L are further discussed in section 5.3.2 as droplet 3-150L has the highest Weber number of the droplets in Table 14.

The droplets impacting the dry solid surface showed no visible splashing, nor visible secondary ejected particles. The results of droplet 1-150D, droplet 4-150D and droplet 5-150D are not recorded from dispensed drops but are records from the uncontrolled leaking droplets. 4-150D is further discussed. Drop 2-150D and drop 3-150D show results of dispensed droplets. A spread-out lamella was observed. From these 2, only droplet 2-150D is further discussed.

5.3.2 HIGH-SPEED CAMERA IMPACTING IMAGES

This section elaborates on the high-speed camera images from specific droplets of Table 13 and Table 14. The images are snapshots of the high-speed camera video recordings of the liquid impingement experiments. Section 5.3.2.1 discusses liquid surface and dry solid surface impingement of droplets, dispensed with a 1000 µm nozzle. Section 3.5.2.2. illustrates images of liquid and dry solid surface impingement of droplets generated with a 150 µm nozzle.

5.3.2.1 1000 µm nozzle

5.3.2.1.1 Liquid surface impingement

Figure 24 shows the high-speed camera images of LBE droplet 1-1000L, colliding onto a liquid LBE surface. The cartridge temperature was 140 °C and the fluid box body temperature was 145 °C. The images of the 1-1000L droplet are discussed because the Weber number of the droplet was an outlier compared to the other results of Table 13. The Weber number of the droplet is determined to be 260 ± 58, while other Weber numbers vary from 386 – 499. This small Weber number is due to the 1-1000L droplet's size; the droplet is the smallest of his series, with a diameter of only 1.64 ± 0.37 mm.

Droplet 1-1000L: Ø = 1.64 ± 0.37 mm, v = 2.48 m/s, We = 260 ± 58

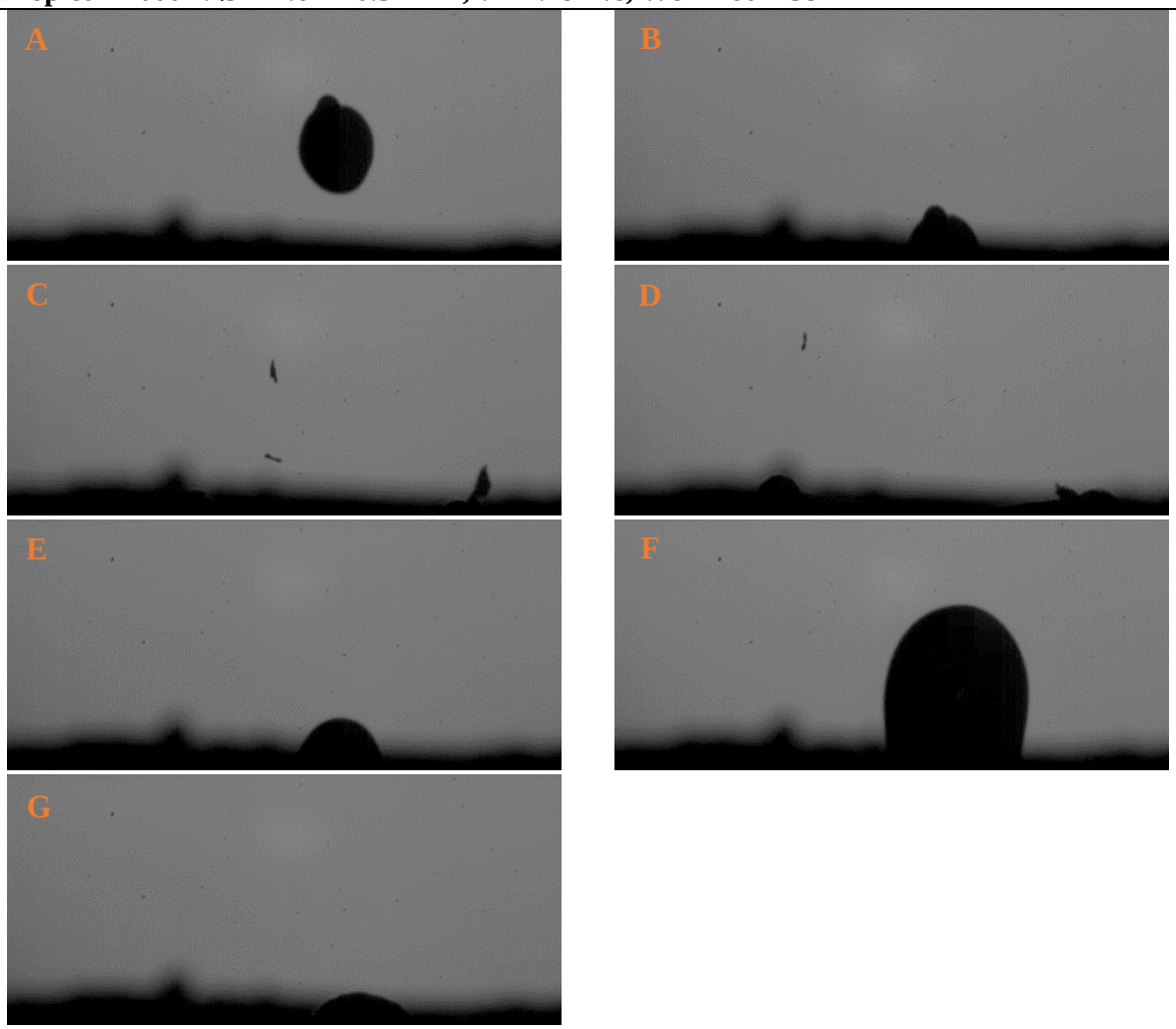

Figure 24: Images A-G illustrate snapshots from the high-speed camera recordings of droplet 1-1000L, impacting a liquid surface.

Figure 24A of falling LBE droplet 1-1000L illustrates that the droplet is not spherical. The droplet impacts the liquid surface during Figure 24B. The impact almost immediately generates secondary particles, as can be seen in Figure 24C. A 'finger' can be observed at the right of the image 24C. This 'finger' can be an arm of a crown-formed splash. Also, a round shape in focus can be seen in the middle of Figure 24D.

It is not clear to say whether crown splash occurs or not, since the camera was not positioned perfectly perpendicular in line with the surface. The liquid surface was not observed. Due to this reason, it is not possible to say whether the Weber number 260 ± 58 could be a threshold for crown splashing for the specific conditions. Figure 24E and 24F show a fluid jet rising from the impacted spot. This phenomenon is called rebound. The rebound rises from the liquid surface. During this rebound motion, no secondary droplets are observed. The rebound exceeds the initial liquid layer, as shown in Figure 24F. At the end, the liquid surface returns to an equilibrium state without rebounding droplets.

Figure 25 (page 57) illustrates droplet 2-1000L impacting a liquid surface. Droplet 2-1000L's large diameter and thus Weber number were outliers compared to the other 1000 µm nozzle results (Table 13).

Falling droplet 2-1000L has a deviating droplet shape, illustrated in Figure 25A. The droplet impinges the liquid LBE surface in Figure 25B. Secondary droplets are almost immediately ejected. Figure 25C-E illustrate the rising liquid column; a clearly formed 'crown' splash. Many secondary droplets are being ejected from the rim of the crown. The crown's fingers become less pronounced and fade (Figure 25E-I). The crown collapses and decreases (25I). When the liquid level of the surface is reached again, a rebound is created at the impact location. The rebound exceeds the original liquid layer and even the height of the crown. Almost no visible secondary droplets are created during the rebound. Eventually, the liquid surface reaches its original shape.

When comparing these results of droplet 2-1000L to the previous results of droplet 1-1000L (Figure 24); the crown of droplet 2-1000L in Figure 25E is clearly visible, while droplet 1-1000L almost showed no crown. Both LBE droplets had the same impact velocity (2.48 m/s). Droplet 1-1000L has a smaller diameter and thus also a lower Weber number (1-1000L: We = 260 ± 58, 2-1000L: We = 499 ± 98) than 2-1000L. More secondary droplets are ejected during the crown splash of droplet 2-1000L.

Figure 26 (page 58) shows LBE droplet 4-1000L impacting a liquid LBE surface. The collision almost immediately generates secondary particles being ejected, which can be seen in Figure 26C-E. Figure 26E shows the formation of a splashing pattern, namely a crown splash which is rising from the impact spot.

Compared to droplet 2-1000L (Figure 25), the crown of droplet 4-1000L (Figure 26) is less pronounced. Also, the crown does not reach the same large height but continues to expand radially during the axial fading of the crown. It could be possible that due to the leaking, the liquid surface was disrupted when droplet 4-1000L impacted. After the crown form fades and the initial liquid layer is reached, a rebound rises from the impacting location. The rebound exceeds the crown's height. After the rebound is faded, in Figure 26I, a second rebound is formed which can be seen in Figure 26K.

Droplet 2-1000L: Ø = 3.16 ± 0.61 mm, v = 2.48 m/s, We = 499 ± 95

Figure 25: Images A-N illustrate snapshots from the high-speed camera recordings of droplet 2-1000L, impacting a liquid surface.

Droplet 4-1000L: Ø = 2.85 ± 0.24, v = 2.49 m/s, We = 454 ± 41

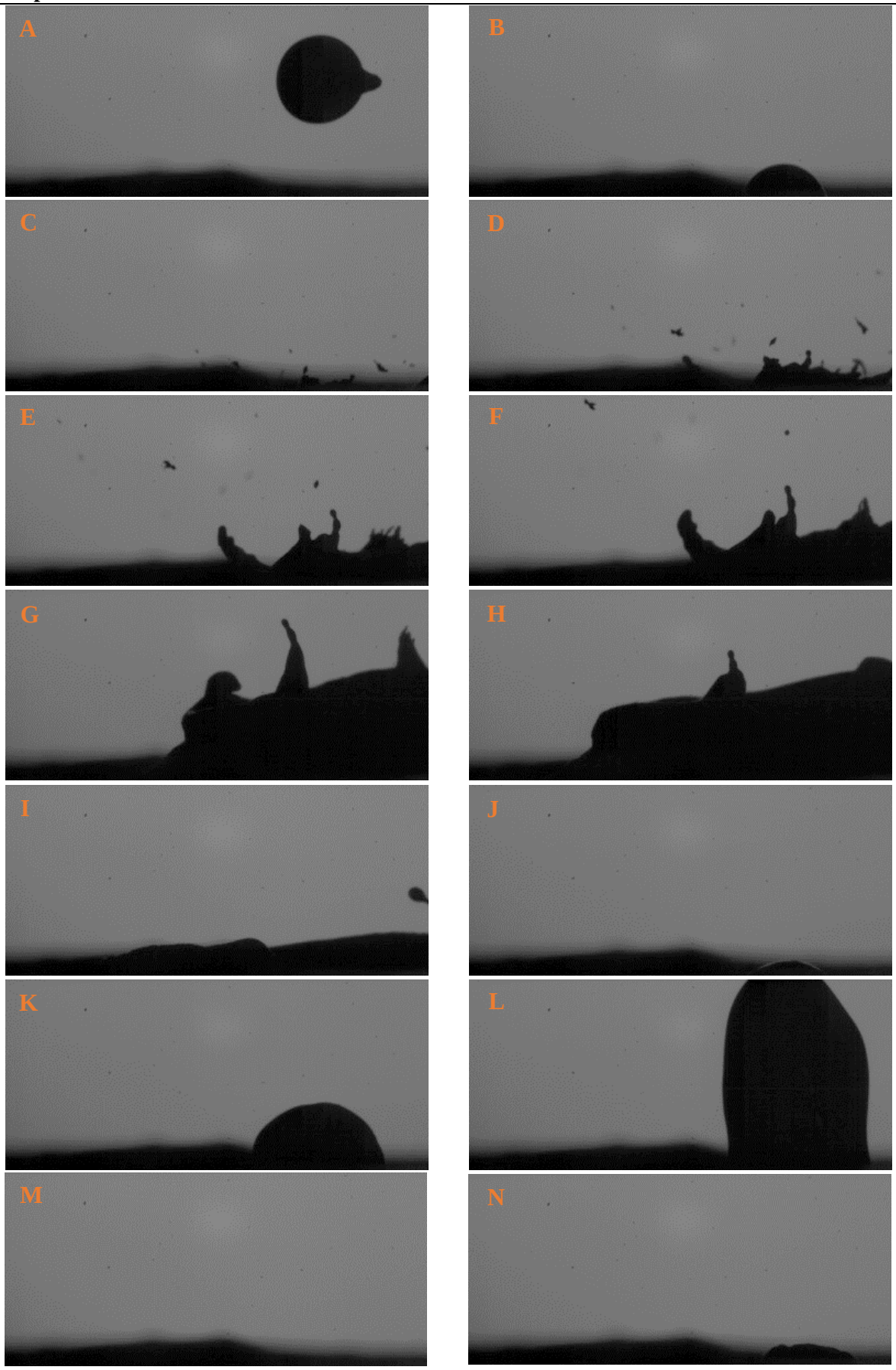

Figure 26: Images A-N illustrate snapshots from the high-speed camera recordings of droplet 4-1000L, impacting a liquid surface.

5.3.2.1.2 Dry solid surface impingement

Following splash recordings in Figure 27 show droplet 8-1000D, impacting a dry smooth surface. Droplet 8-1000D impacts a previously solidified droplet on the dry surface with 2.53 m/s. The droplet diameter is 2.36 mm and the Weber number is 389 ± 10. Droplet 8-1000D seems to have a spherical shape. The droplet impacts an already solidified fallen drop, i.e., a circular shaped lamella. This increases surface roughness, which is expected to increase the occurrence of splashing [22].

Droplet 8-1000D: Ø = 2.36 mm, v = 2.53 m/s, We = 389 ± 10

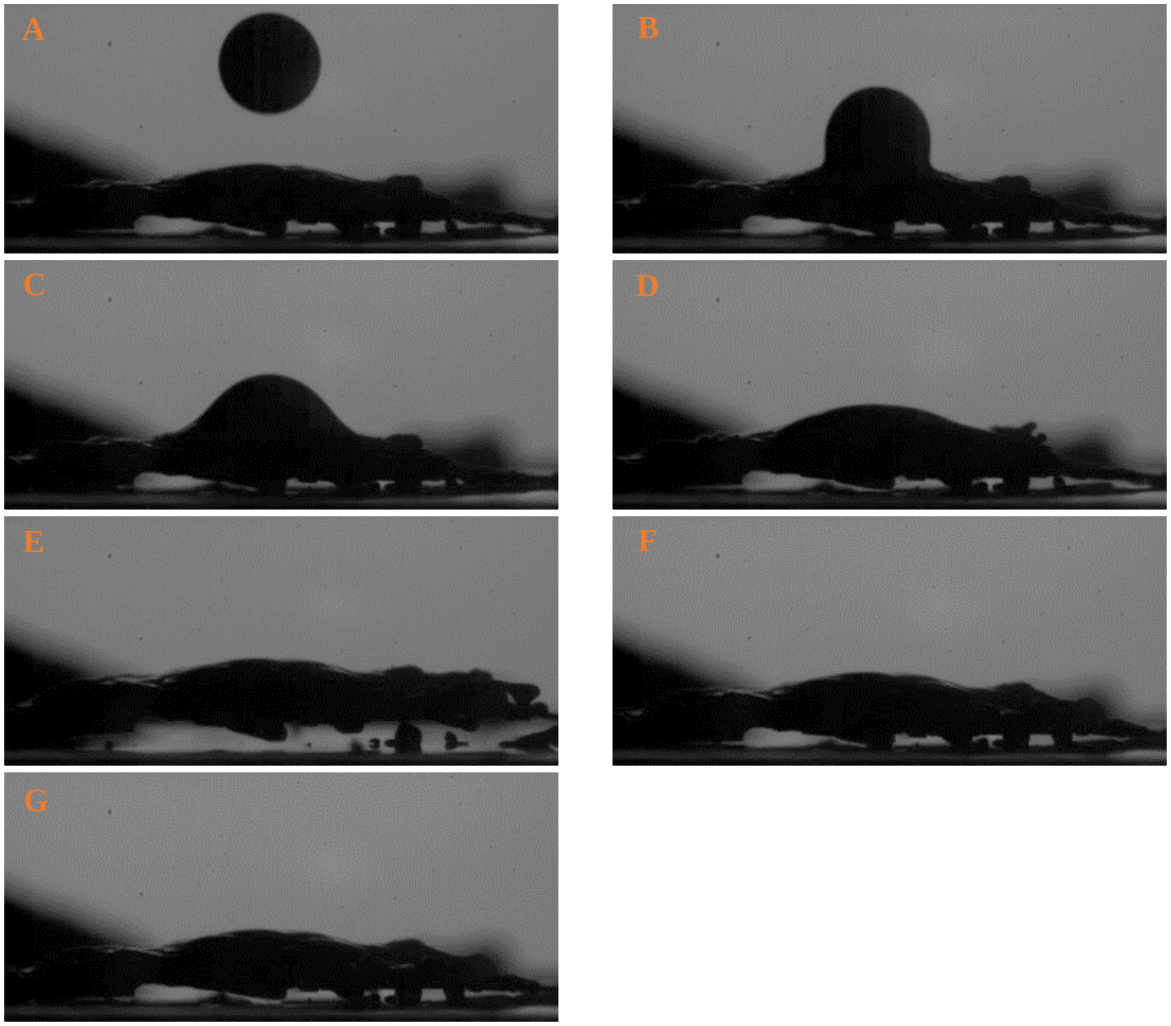

Figure 27: Images A-G illustrate snapshots from the high-speed camera recordings of droplet 8-1000D, impacting a dry solid surface.

The droplet 8-1000D seems to coalesce with the already present lamella in Figure 27C and Figure 27D. The liquid droplet radially expands over the former lamella. No splashing or secondary droplets are observed. This may indicate that the Weber number is not sufficiently large to generate secondary droplets or that the secondary events are too fast to be recorded or to be seen. In Figure 27E, the combination of both lamellae seems to separate from the surface through a lift-off due to the impact of the collision.

When other droplets fell on the lamellae, high stacking shapes were created due to the fast solidification and the aligned impingement, shown in Figure 28. The shapes are easy to remove from cold metal surfaces as the LBE does not wet the surface. The leaking droplets kept falling on top of each other. This way, high piles were formed on the cold solid surface. When the height increased, the shape broke and fell.

Figure 28: Pile of stacked 8-1000D droplets on a dry solid surface.

The right picture of Figure 28 is taken inside the SPLAT chamber. Secondary particles, formed due the collision, can be seen on the dry solid surface around the pile.

Figure 29 shows droplet 9-1000D impacting a dry solid surface.

Droplet 9-1000D: Ø = 2.60 ± 0.16, v = 2.52 m/s, We = 429 ± 28

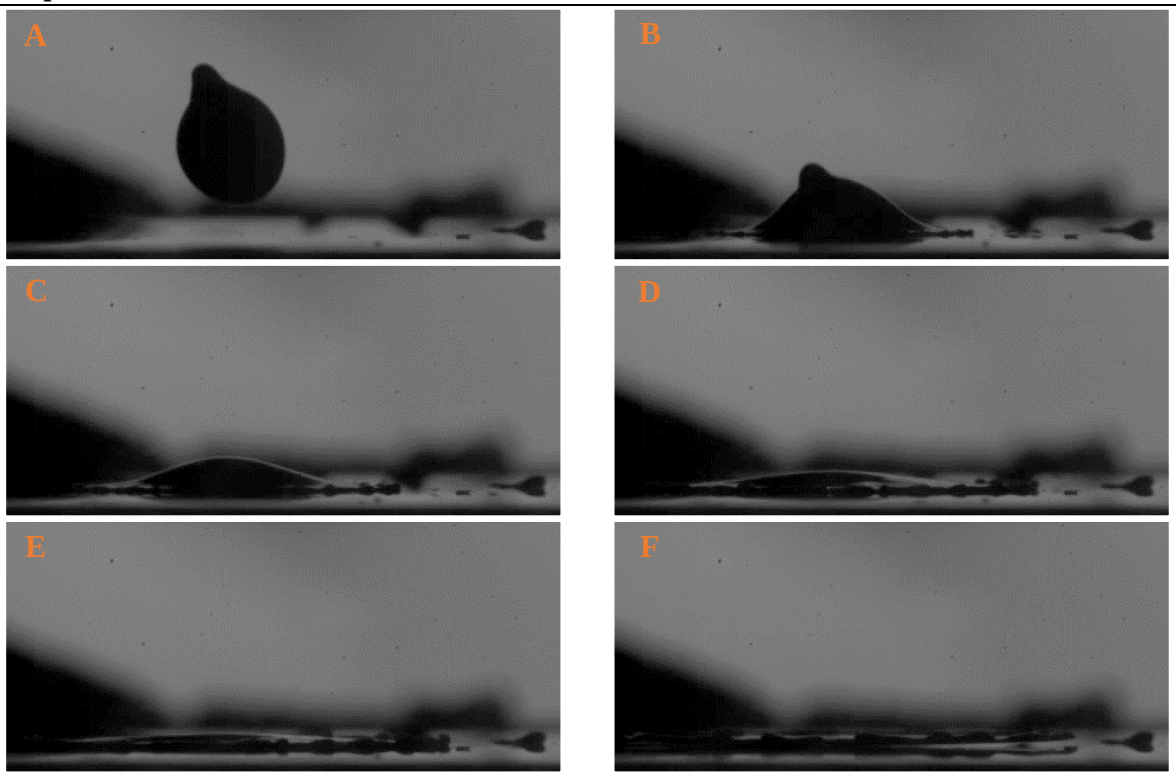

Figure 29: Images A-F illustrate snapshots from the high-speed camera recordings of droplet 9-1000D, impacting a dry solid surface.

The impact of the droplet shows an immediate coalescence in Figure 29B. The contact edge between the drop and the surface radially expands, spreading the liquid out over the surface in Figure 29C and 29D. The spreading liquid film results in the formation of a thin disc-shaped lamella, bordered by a thicker rim (Figure 29E). The lamella has typical finger shapes. This liquid film radially expands due to the kinetic energy and then retracts due to capillary forces. It is not possible to see the expansion and contraction of the droplet on the images, but they were visible on the video recordings of the phenomenon. When the lamella reached its maximum radius, the recordings showed the solidification of the droplet through the fading of the ‘gloss’ of the lamella.

Hereafter, the lamella seemed to separate from the surface. This can be observed in Figure 29F, where the right finger of the lamella rises from the surface. This lift can be due to volume changes due to solidification. Other references state that during the impact, the droplet entraps a small air bubble under its center. During the 'flatting' into the lamella shape, the air bubble breaks and escapes. Due to this escaping air underneath the lamella, it seems like the lamella is 'skating on a film of air' [22]. However, this rather typical for rough surfaces. The liquid impingement of droplet 9-1000D was performed on a smooth solid surface. As already mentioned, the surface was cleaned in between recordings to get rid of solidified leaking droplets. This cleaning was performed by 'pushing' previous solidified droplets away with a tissue. It may be possible that due to this simple cleaning procedure, the surface was not cleaned sufficient and therefore became rougher.

The images in Figure 30 illustrate droplet 10-1000D.

Droplet 10-1000D: Ø = 2.56 ± 0.99, v = 2.53, We = 423 ± 19

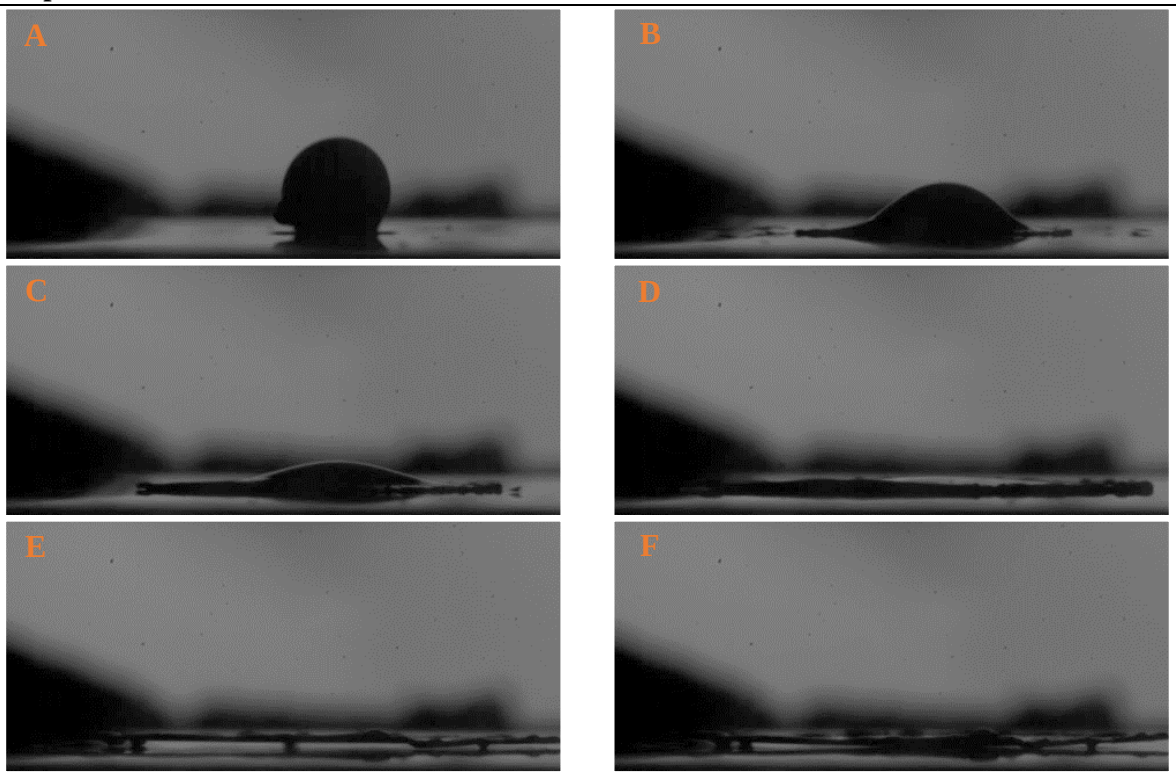

Figure 30: Images A-F illustrate snapshots from the high-speed camera recordings of droplet 10-1000D, impacting a dry solid surface.

Droplet 10-1000D spreads over the dry solid surface after impact. The result is in agreement with the other dry solid surface impacting images of droplet 8-1000D and 9-1000D. The impingement shows no visible secondary ejected droplets but a spread disc-shaped lamella instead. Figure 30E shows the lamella separating from the surface through a lift-off. This is due to volume changes of solidification. When comparing 8-100D, 9-1000D and 10-1000D, the impacting velocity nor the Weber number seem to affect the impingement outcome since all dry solid surface recordings were similar.

Figure 31 illustrates droplet 10-1000D after impact on the dry solid surface inside the SPLAT chamber.

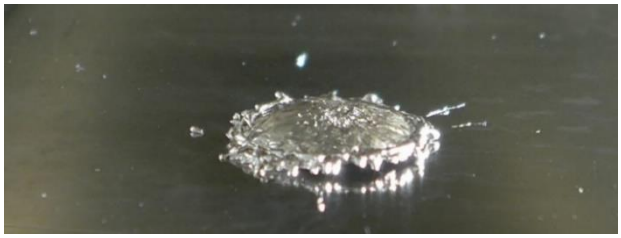

Figure 31: Lamella of droplet 10-1000D on a dry smooth solid surface..

The solidified droplet shows a thin disc-shaped liquid film bordered by a thicker rim with ‘fingers’. The impacting surface, i.e., the metal plate seems clean of LBE secondary droplets around the lamella. The lamella is not completely in contact with the surface but shows a hollow shape. This is due to the volume change of LBE after solidification, which also was the case during the expansion of the solidified droplets inside the cartridge (section 3.3.1).

5.3.2.2 150 µm nozzle

The next images show recordings of impacting LBE droplets, dispensed with a 150 µm nozzle.

5.3.2.2.1 Liquid surface impingement

Figure 32 shows images of droplet 3-150L, impacting a liquid surface. Droplet 3-150L is chosen to discuss since it showed the clearest splashing compared to other droplets in its series. The droplet has a diameter of 1.32 ± 0.56 mm, an impact velocity of 2.43 m/s and a Weber number of 201 ± 85. Droplet 3-150L strongly deviates from the expected spherical shape. As mentioned in section 2.5.2.1, the droplet’s shape is determined by liquid properties, by the initial conditions upon release and by the interaction of the droplet with its surroundings. Moreover, oscillations and the medium through which the droplet falls may affect the droplet shape. Since numerous parameters influence the droplet shape, it is not possible to explain the deviating shape of the droplet.

Droplet 3-150L: Ø = 1.32 ± 0.56, v = 2.43, We = 201 ± 85

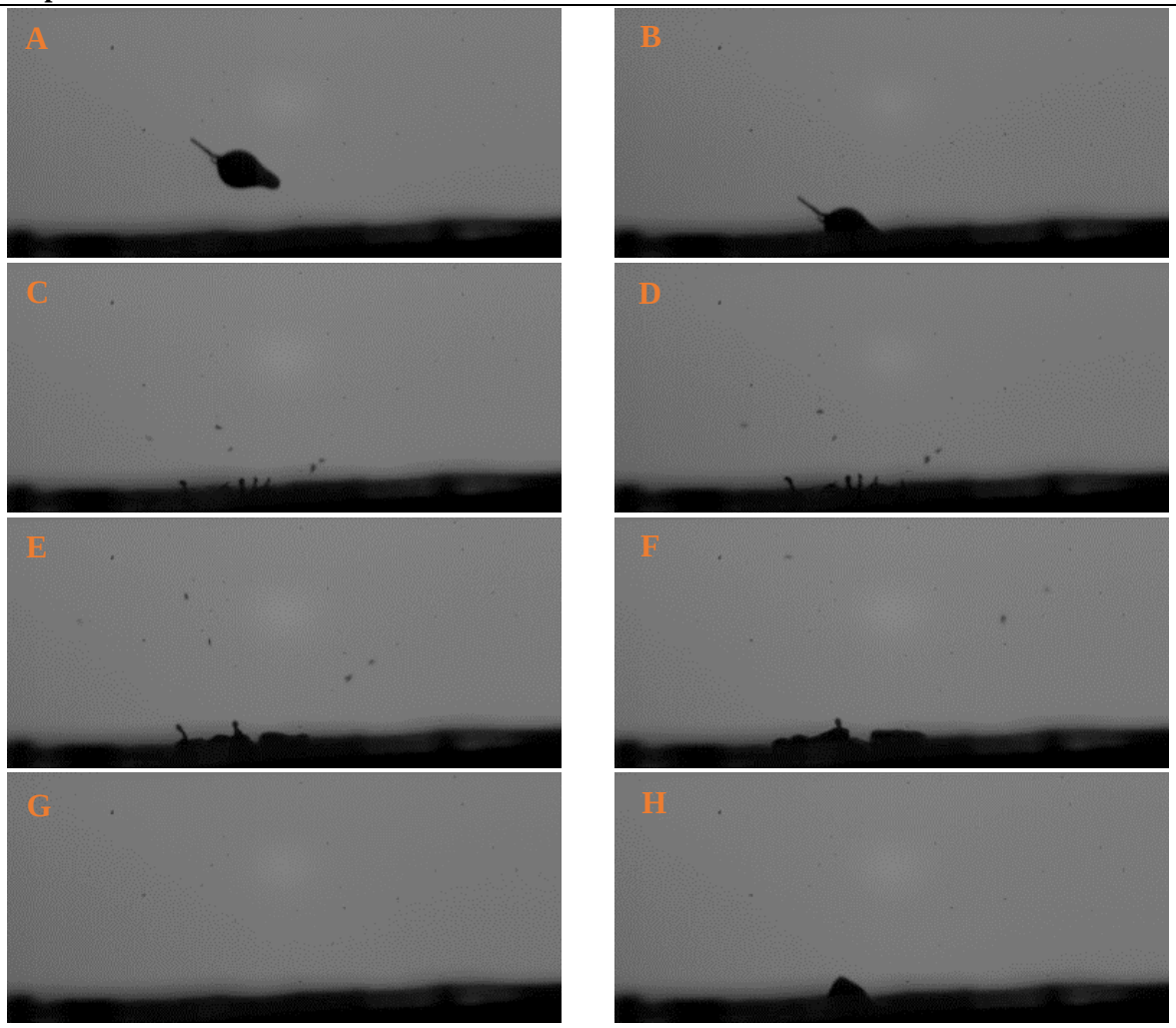

Figure 32: Images A-H illustrate snapshots from the high-speed camera recordings of droplet 3-150L, impacting a liquid surface.

When droplet 3-150L impacts the liquid LBE surface, splashing is immediately observed in Figure 32C and 32D. The crown-shapes of the splashing form seem to be formed above the surface in Figure 32C-E. The crown fades in Figure 32F. Lastly, the initial surface layer is retrieved, followed by the formation of a rebound in Figure 32H. The splashing form is hard to determine since the surface cannot be sufficiently seen. The crown splash is less pronounced and smaller than during impingements with a 1000 µm nozzle. This is line with the assumptions, namely splashing increases with increasing Weber number.

Droplet 6-150L is discussed in Figure 33. Droplet 6-150L shows a very deviating drop shape.

Droplet 6-150L: Ø = 1.00 ± 0.22, v = 2.44, We =152 ± 34

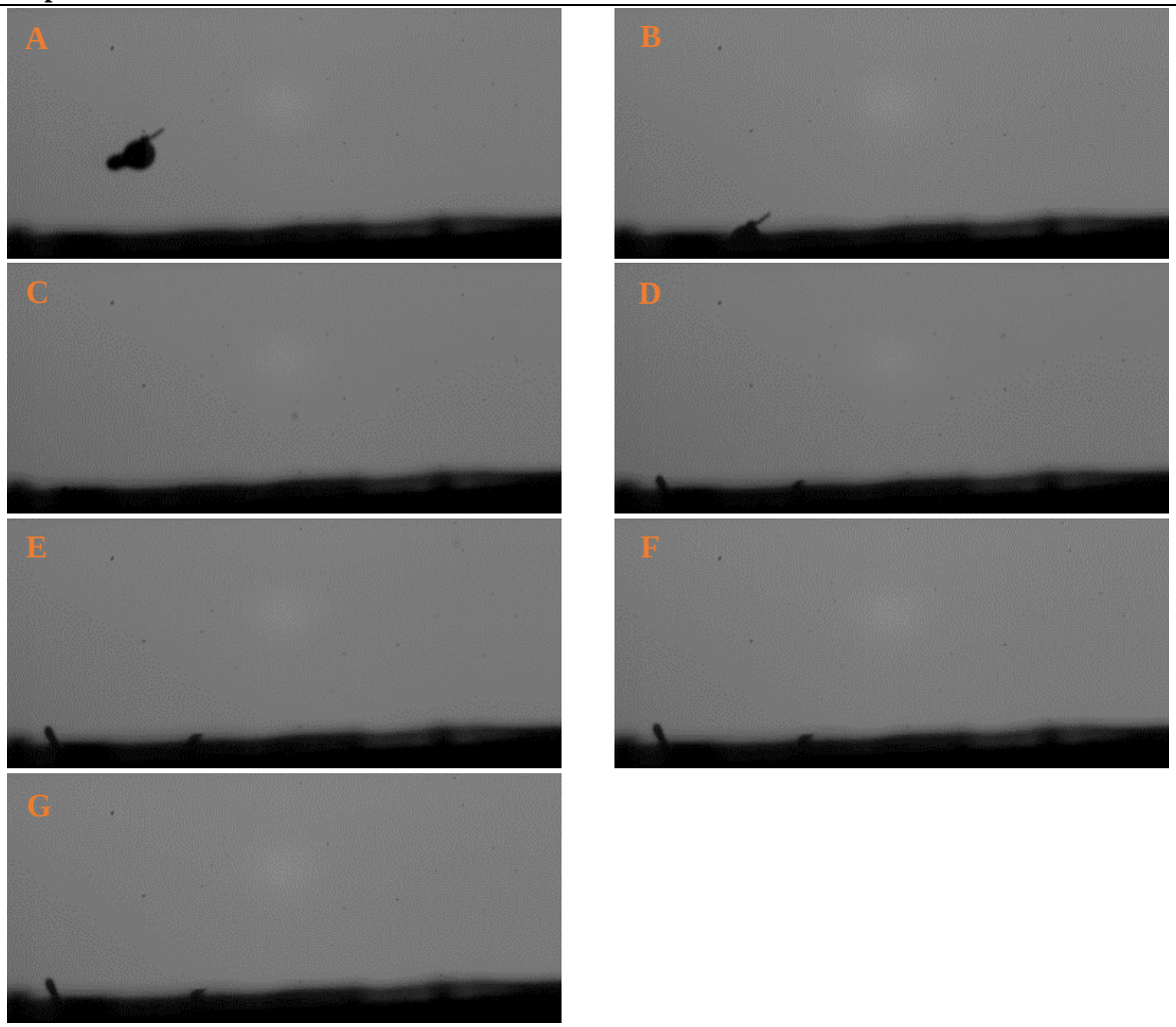

Figure 33: Images A-G illustrate snapshots from the high-speed camera recordings of droplet 6-150L, impacting a liquid surface.

It is not clear to see on the images of Figure 33, but the video recordings of the droplet showed secondary droplets being ejected. In Figure 33D-F, fingers are observed. Because it is not possible to clearly see the surface, it is not clear to say which splashing form occurs. Droplet 6-150L has a diameter of 1.00 ± 0.22 mm and a Weber number of 152 ± 34.

The previous droplet (3-150L) in Figure 32 has a higher Weber number (i.e., 201 ± 85) and is larger (i.e. 1.32 ± 0.56 mm). When comparing the two droplets, both generate splashing instead of spreading. Secondary droplets are ejected in both cases. The ‘crown splash fingers’ of drop 3-150L reach larger heights than those of droplet 6-150L. The splashing is more extensive and more secondary drops are observed. These differences can be explained by the lower Weber number and diameter of droplet 6-150L.

When comparing the previously discussed results of liquid LBE impingement on a liquid surface using a 1000 µm nozzle (5.3.2.1) with the results of this section (150 µm nozzle), it can be noted that more splashing occurred for the larger droplet, ejected from the 1000 µm nozzle. All 1000 µm-nozzle droplets showed splashing and - except for one -, all droplets displayed clear crown splashes. This is contrast to the liquid impingement with the smaller nozzle and thus with smaller droplets, indicating that higher droplet diameters (i.e. higher Weber numbers) have a major impact on splashing.

Increasing the droplet's Weber number favors splashing, in line with the expectations. A higher impact velocity should also benefit splashing. However, in this research study, the differences in velocities are assumed to be too small to observe significant and clear differences in impact outcomes.

5.3.2.2.2 Dry solid surface impingement

Figure 34 shows the pictures of impinging droplet 2-150D onto a dry solid surface.

Droplet 2-150D: Ø = 1.17 ± 0.05, v = 2.52 m/s, We = 189 ± 9

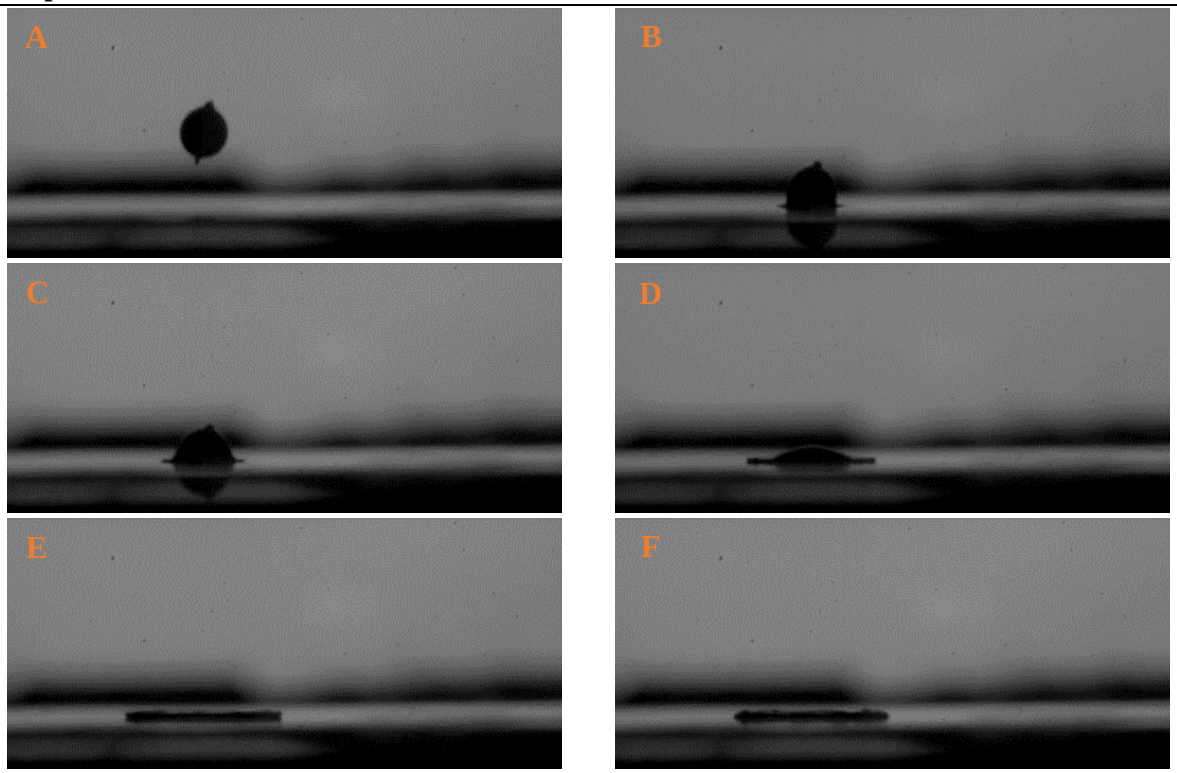

Figure 34: Images A-F illustrate snapshots from the high-speed camera recordings of droplet 2-150D, impacting a dry solid surface.

The droplet spreads out after impacting the smooth solid surface in Figure 34B and C. A circular lamella is formed (Figure 34E-F). The typical lamella finger shapes are not observed. The recordings also showed no expansion and contraction, nor a lift-off of the lamella. When comparing to the 1000 µm nozzle results, almost all lamellae showed lift-off, fingers, contraction and expansion. The difference again can be attributed to the lower Weber number, mainly related to the smaller diameters of the droplets dispensed with the 150µm nozzle.

Figure 35 shows recordings of leaking LBE droplets in succession. No dispenser parameters were installed to obtain these droplets. The droplet is identified as 4-150D.

Leaking droplet 4-150D

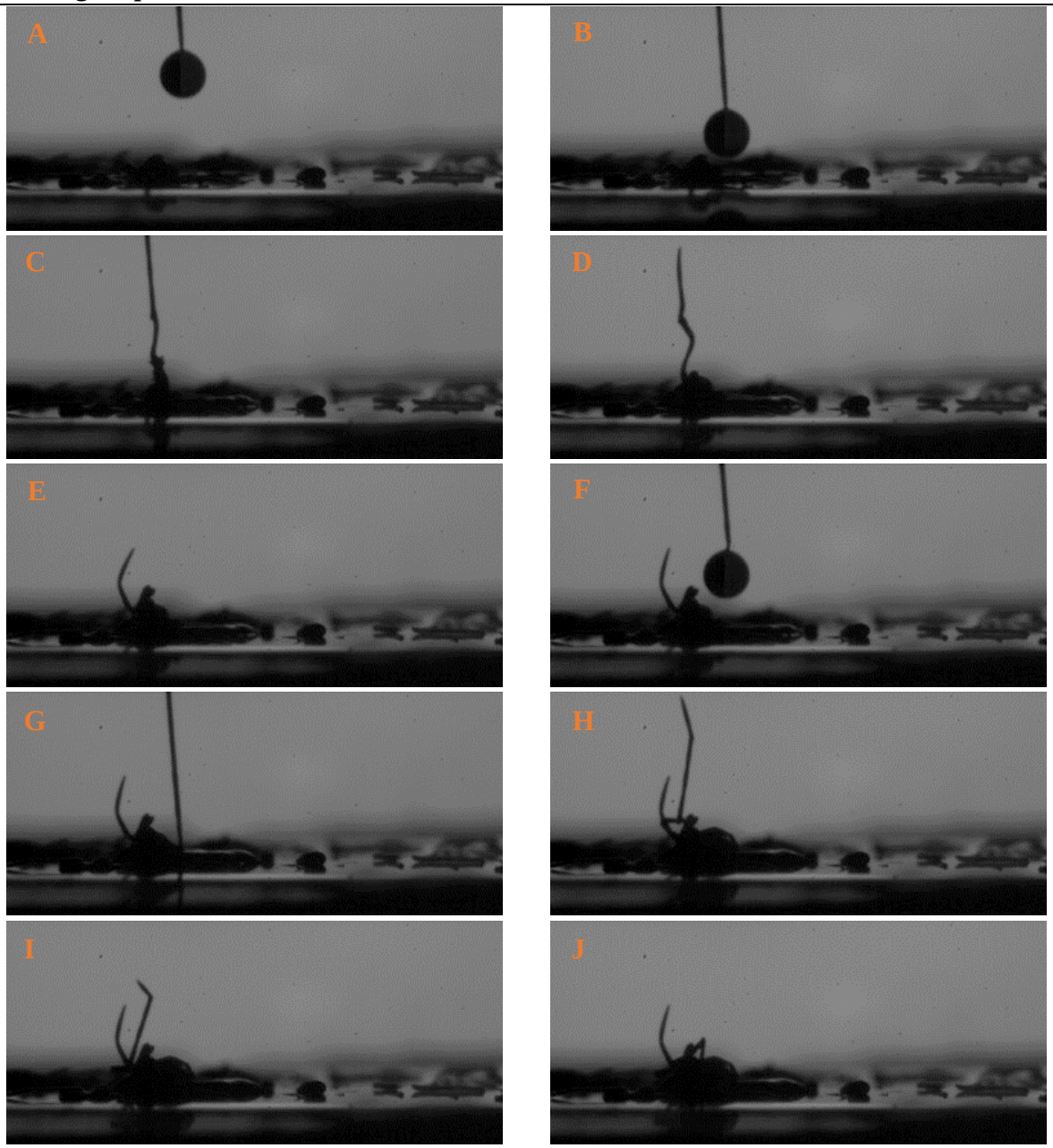

Figure 35: Images A-J illustrate snapshots from the high-speed camera recordings of leaking droplet 4-150D, impacting a dry solid surface.

The images of Figure 35 firstly show why the leaking falling droplets were easy to distinguish from the on demand requested dispensed droplets. The leaking droplets showed a long tail, illustrated in Figure 35A and 35B. This deviating shape can be linked to the immobile state of the tappet. During dispensing, the fluid jet is 'cut' into droplets by the downward movement of the tappet, characterized by the falling time. During the leakage, the drops are not 'cut', since no signal is given to the tappet.

When the leaking drop impacts the surface (Figure 35A), the drop spreads over the surface. The 'tail' of the droplet reaches the surface at a later stage than the droplet itself, this can be derived from Figure 35B till Figure 35E. The lamella is not clear to see on the images since the dry solid surface was not cleaned before the leakage was recorded. But, the lamella formation could be seen during the performance of the experiments. The lamella in Figure 35G shows a tail as well.

This could be due to the delay in which the droplet's 'tail' arrives. When a second leaking droplet impacts onto the previous solidified lamella (Figure 35F), the lamella shows again a sharp tail. During the impingement, no secondary droplets are observed to be created nor ejected. It is possible that the secondary droplets were ejected to fast to be recorded with the high-speed camera. When the leaking continued, a stacking of droplets is created. Because of the droplet's tail, the stack has sharp spines, illustrated in Figure 36.

Figure 36: Pile of stacked leaking LBE droplets on a dry solid surface.

The formation of a pile was already the case for droplets generated with a 1000 µm nozzle, as can be seen in Figure 28. The stack of solidified leaking droplets is sharp since the leaking droplets have 'a tail', in contrast to dispensed droplets. The left image of Figure 36 shows a pile being formed after a previous pile broke off and fell. Since a leak could occur anywhere at any time in MYRRHA, the stacking of these oddly formed LBE droplets (Figure 28 and Figure 36) are in truth real-world realistic and possible outcomes. The sharp pines are expected to cause significant deformation (i.e. splashing) of impacting droplets on the pile.

5.4 Aerosol particle size distribution results

This section discusses the results of the PSD measurements of the formed LBE aerosols.

Because of the leaking dispenser, it was not possible to perform the particle size distribution (PSD) experiments as initially planned. For this reason, the experiments were simplified. The PSD was measured of impacting droplets leaking uncontrollably from the dispenser instead of from droplets generated with parameter-set 5 ms RT, 1 ms FT and 5 ms OT. The leaking frequency altered during the experiments and varied between ± 1 droplet every second to ± 1 droplet every 5 seconds.

Because the characteristics of the leaking droplets are unknown, several leaking droplets were collected and weighted to determine their size. The results can be seen in Table 15.

Table 15: Size of leaking LBE droplets (with a 1000 µm nozzle).

$m_{droplet}$ (g)	$d_{droplet}$ (mm)
0.1228	2.81
0.1372	2.92
0.1359	2.91
0.1371	2.92
0.1421	2.95
Average	2.90 ± 0.02

The leaking droplets with a 1000 µm nozzle opening have an average diameter of 2.90 ± 0.02 mm diameter.

5.4.1 SMPS AND OPC RESULTS

Before liquid impingement was performed, the SPLAT enclosure was flushed with 2.6 l/min argon gas. From this gas flow, the PSD is measured as reference and illustrated in 2D in Figure 37.

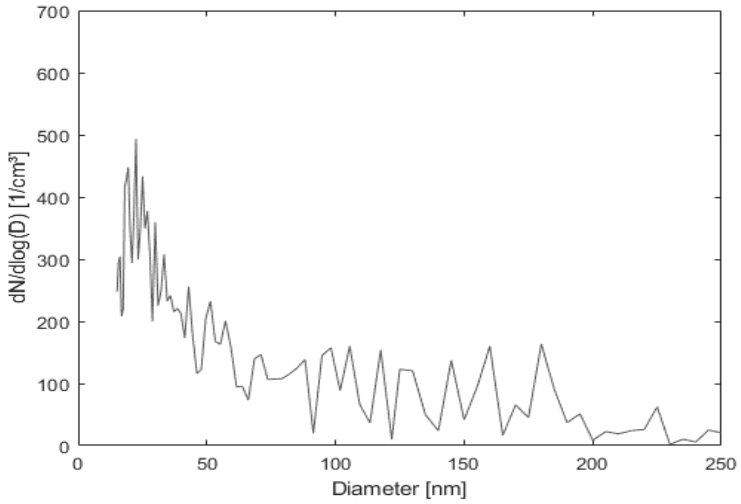

Figure 37: Reference: PSD of argon gas.

Through the results of Figure 37, it can be stated that the measured aerosols in following graphs (Figure 38, 39 and 40) are actual LBE aerosols.

Following Figure 38 and Figure 39 provide a 3D overview of the PSD experiments. Figure 38 shows the PSD of liquid impingement on a dry solid surface and Figure 39 shows the PSD of liquid impingement on a liquid surface, both in 3D. The graphs were obtained by merging the SMPS (< 100 nm) and OPC (> 100 nm) results.

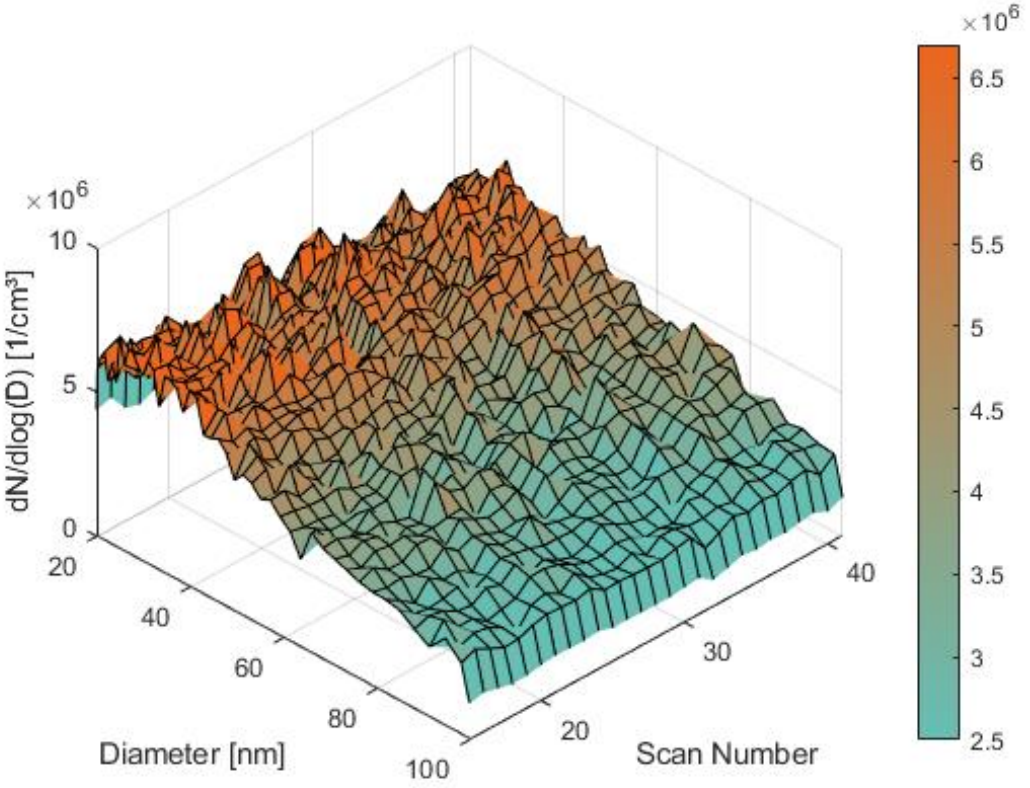

Figure 38: 3D graph of the PSD of dry solid surface impingement.

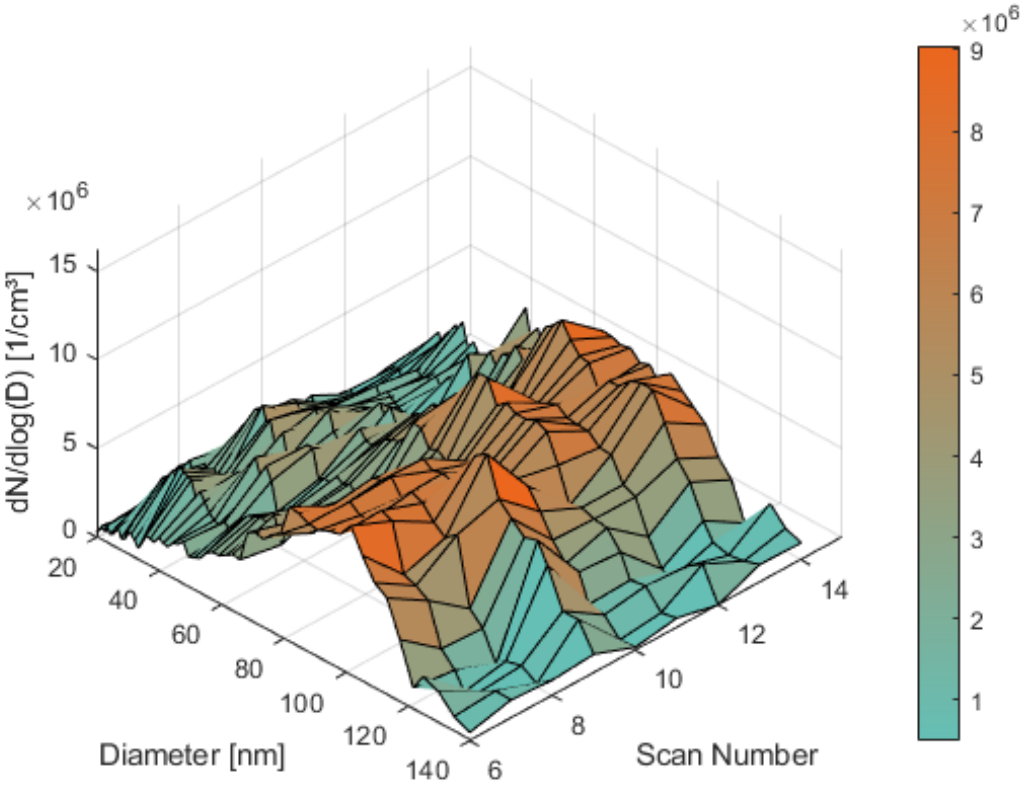

Figure 39: 3D graph of the PSD of liquid surface impingement.

From Figure 38, it can be observed that most generated aerosol particles, due to impingement of LBE droplets on a dry solid surface, are located in the area of the SMPS (i.e. 20 nm < d < 100 nm). The concentration of small particles is higher than the concentration of large particles. The peak concentration of LBE particles is situated near an equivalent particle size of 25 nm. The shape of the curve suggests that a significant amount of particles smaller 20 nm will be present, but these are not visualized on Figure 38 due to the lower particle size limit of the SMPS. Also, it can be observed that similar PSDs are recorded with each scan, i.e. 'a steady state' is reached.

The width of the PSD of the liquid surface (Figure 39) exceeds that of the solid surface (Figure 38). The aerosol particles due to liquid surface impingement have diameters up to 140 nm, with a distribution maximum in the 60-80 nm range.

Figure 40 provides a 2D graph of the PSD of the liquid and solid surface. The graph is obtained by averaging the previous 3D scans (Figure 38 and Figure 39).

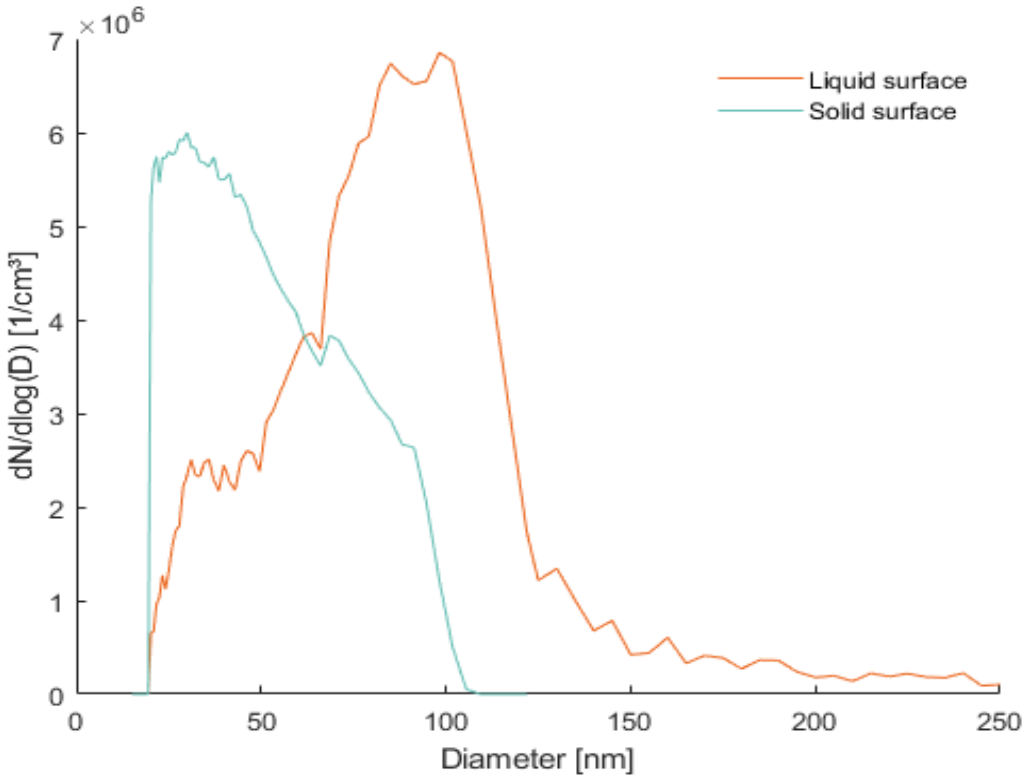

Figure 40: 2D graph of the PSD of dry solid and liquid surface impingement.

Figure 40 indicates that the aerosol particle distribution shifts to larger particle size bins during liquid surface impingement compared to dry solid surface impingement. The impact of LBE droplets in succession with an average diameter of 2.90 ± 0.02 mm on a dry surface, generates aerosol particles between ± 20 and ± 105 nm diameter. The sharp decline in particle concentration near 20 nm is most likely indicating that the SMPS cannot detect particles below this size range. The PSD maximum (i.e. 6.10^6 particles/cm³) is located at ± 28 nm diameter. Hereafter, the particle concentration of the solid surface graph decreases with particle size.

From Figure 40, it can be derived that the aerosol particle sizes from liquid surface impingement range from ± 20 nm till up to 250 nm. The distribution peaks at approximately 100 nm. The concentration at this point is ± $6.9.10^6$ aerosol particles/cm³.

The dry solid surface altered during the experiments, starting with a clean and smooth surface, followed by the formation of a rough surface (pile) and finally even a pseudo-liquid surface (dimple). A pile of stacked droplets was built by the impacting droplets in succession. Because the frequency of the leaking droplets was high, the pile became heated. After some time, a dimple was formed at the top of the pile of stacked droplets, illustrated in Figure 41. In this dimple, the LBE droplets did not solidify immediately but remained liquid.

Figure 41: Pile of stacked solidified droplets with a pseudo-wet dimple at the top.

From the dry solid surface and viewports (Figure 41), it can be seen that significant amounts of secondary droplets were formed by the impact.

6 CONCLUSIONS AND PERSPECTIVES

In this thesis, we have studied the formation of aerosols resulting from the impact of liquid lead-bismuth eutectic droplets on various surfaces. This chapter summarizes the results, from which conclusions are drawn and from which an outlook for further studies is retrieved.

6.1 Experimental parametric survey

This section provides an overview of the theoretical expected differences between liquid impingement with water droplets and with LBE droplets regarding impact velocity, impact energy (characterized by the Weber number) and impact time.

It can be concluded that the 1) Weber numbers for LBE droplets will exceed those for water droplets with an expected factor of ± 1.8 for droplets of the same diameter and impact velocity. 2) Falling LBE droplets will reach higher impact velocities for a given fall height than similar water droplets due to LBE's higher density (10,548 kg/cm³ at 140 °C versus 998 kg/cm³ for water at 20 °C). 3) The impact velocities are observed to increase with fall height and droplet diameter. Since impact velocity is squared in the Weber number equation, it will have a significant affect. The Weber number for an LBE droplet will thus be at least 1.8 times higher than for a same sized water droplet, falling over the same distance.

Overall, LBE is expected to generate significant splashing and thus significant amounts of aerosols. Therefore, from a safety-point of view within the framework of aerosol formation, LBE is less preferred than water since aerosol generation due to liquid impingement is expected to be more extensive.

6.2 Droplet generation with a micro dispenser

6.2.1 CORRELATION OF DISPENSER PARAMETERS AND DISPENSED DROPLET

It was decided to generate LBE droplets with a micro dispensing system, in which droplets are dispensed by a downward moving tappet. The dispensing cycle is characterized by several parameters such as "rising time"," open time", "falling time", "needle lift", "number of pulses", "delay", "supply pressure", "cartridge temperature" and "fluid box temperature". The latter four were kept constant during this parametric study.

Rising time is observed to affect the dispensed volume. Increasing rising time results in increasing dispensed droplet diameter and increasing dispensed volume. Open time shows similar effects. When rising time and open time are increased, the number of dispensed droplets increases since more fluid is sucked in and since more fluid flows through the fluid box during the time in which the valve remains open. The droplet diameter increases as well. Falling time refers to the time in which the tappet moves down and pushes the fluid out the nozzle insert. A high falling time results in generation of multiple droplets since the fluid jet is not 'cut' sufficiently by the tappet. Since all parameters are observed to influence one another, the number of pulses cannot simply be equated to the number of dispensed droplets. When number of pulses is set to 1 but rising time and open time are set to high values, more than one droplet or even a flow may be ejected. When falling time, rising time and open time are set to rather low values to decrease their influence, the number of pulses may be equated to the number of dispensed droplets.

From this study, a parameter-set (RT, OT, FT) was derived that allowed reliable dispensing one droplet per pulse.

6.2.2 DROPLET SIZE DETERMINATION

The dispensing experiments were performed with a 150 µm nozzle and a 1000 µm nozzle to ensure an analysis of a wide range of dispensed LBE droplet diameters. With the 150 µm nozzle, LBE droplets from 0.50 ± 0.10 mm diameter up to 1.48 ± 0.10 mm diameter could be dispensed by varying the RT, OT and FT parameters. With the 1000 µm nozzle, LBE droplets from 1.83 ± 0.03 mm diameter up to 4.57 ± 0.06 mm diameter were obtained.

6.3 Troubleshooting

After moving the dispenser from ex-situ to the top of the SPLAT setup, the dispenser started leaking. It is assumed that the leaking problem is a combination of several factors. While the cause of the leakage could not be established within the time frame of this thesis work, the frequency with which droplets leaked out could be sufficiently lowered by lowering the micro dispensing system temperatures and by creating an under pressure in the dispenser's cartridge.

To perform further studies within the framework of aerosol formation due to liquid impingement, a properly functioning micro dispensing system is required. For this purpose, the dispenser will be sent back to the company to inspect the valve.

6.4 Liquid impingement with high-speed camera

Due to technical difficulties, it was not possible to perform the liquid impingement experiments with the conditions as expected from the parametrical study nor the parameters applied during the previous dispensing experiments.

To diminish the dispenser leakage to an acceptable level, the cartridge temperature and fluid box temperature were lowered as compared to previous applied temperatures and an under pressure was applied to the dispensing system. Therefore, the high-speed camera results deviate from the pre-calculated conditions, showing larger droplet diameters and lower impact velocities, but the Weber numbers derived were in line with the calculated expected values. In addition, many falling droplets showed non-spherical shapes, sometimes with pronounced liquid tails. The applied MATLAB code did not correct for these non-spherical shapes, leading to a second deviating factor on the droplet diameter results.

6.4.1 1000µM NOZZLE

Liquid impingement onto a liquid surface is performed with a 1000 µm nozzle opening. Droplets ranging from 2.44 mm to 3.16 mm diameter were generated. The Weber numbers range from 386 to 499 and the impact velocity from 2.45 m/s to 2.53 m/s, except for one outliner droplet with a diameter of 1.64 ± 0.37 mm diameter and We = 260 ± 58. This outliner droplet generated secondary droplets, being ejecting after impact onto the liquid surface but it was not clear whether prompt or crown splash occurred. All other droplets showed clear crown splash impacting forms. The droplet diameter was observed to influence the splashing.

Dry solid surface impingement was performed with a 1000 µm nozzle as well. Droplets of 2.36 mm to 2.60 mm diameter, with Weber numbers from 389 to 429 and with 2.53 m/s impact velocity were dispensed. The impingement on the dry solid surface of the LBE droplets provoked no splashing. A spreading lamella was observed, which solidified in time. When droplets in succession impacted on each other, a pile of stacked solidified droplets was created on the dry solid surface. The stack of solidified droplets in succession can easily be cleaned since LBE shows no adhesion to metallic surfaces. This stack is a realistic outcome of when a leakage inside the MYRRHA reactor would occur. The Weber number and droplet size do not affect the outcome of impingement with dry solid surfaces, since all dry solid surfaces showed the formation of a lamella and a lift-off. It is possible that the Weber number can be correlated to the radius of the lamella or the lift-off, but these were not measured.

6.4.2 150 µM NOZZLE

The liquid impingement with the smaller nozzle, and thus smaller LBE drops, showed similar results as with the 1000 µm nozzle. Droplets with a diameter between 0.79 mm and 1.32 mm, a Weber number between 135 and 201 and an impact velocity between 2.38 m/s and 2.46 m/s were generated. Most impingements onto the liquid LBE surface formed splashing. It was not possible to determine which splashing (crown or prompt) occurred, since the surface did not came clear into view. The high-speed camera recordings of droplet 2-150L (v: 2.44 m/s; Ø: 0.91 ± 0.04 mm; Weber: 139 ± 7), droplet 7-150L (v: 2.41 m/s; Ø: 0.91 ± 0.13 mm; Weber: 135 ± 20) and droplet 10-150L (v: 2.43 m/s; Ø: 1.12 ± 0.39 mm; Weber: 170 ± 60) showed no generation of visible secondary droplets.

However, other droplets with smaller Weber numbers and diameters did show splashing. A possible explanation is that the splashing of the three mentioned droplets was not captured because the liquid surface was out of the field of view of the camera.

When comparing the liquid surface impingement results of the 150 µm nozzle with the results of the 1000 µm nozzle, it can be concluded that crown splashing is more pronounced for larger droplets. Therefore, it can be concluded that larger droplets generate higher Weber numbers and more splashing. The results are in line with the literature and the expectations.

Dry surface liquid impingement performed with the 150 µm nozzle did not provoke visible splashing. The impact resulted in the formation of a lamella. In contrast to the previous dry solid surface collision performed with the 1000 µm-nozzle, the fingers of the lamella nor the lift-off are visible at the 150 µm nozzle recordings. This may be due to the smaller Weber number. Furthermore, recordings of the leaking droplets in succession with the 150 µm nozzle onto a dry smooth surface, show the buildup of the solidified drops, resulting in a stack. The stack is more needle-like when compared to the previous 1000 µm stack, owing to the 'tail'-shapes of the leaking drops. This stack is a realistic outcome of when a leakage inside the MYRRHA reactor would occur.

In order to be able to make precise claims about liquid LBE impingement, more influencing parameters should be considered. As mentioned, the influence of the gas flow, of the roughness of the dry solid surface, of the temperatures of the surfaces, of the fall height, etc. are not considered in this study. In addition, to see a significant influence of the velocity (and Weber) on splashing, it is necessary to look at a wider range, i.e. larger fall heights. For the short travelled distance of 40 cm as applied in this thesis, the impact energy (and thus Weber number) of the LBE droplets is mainly determined by the mass of the droplets.

To be able to make a matrix for predictions about splashing forms based on Weber numbers, as is available for water, more data and more droplet diameters need to be studied to achieve uniform threshold values for splashing. Furthermore, for subsequent studies, a properly functioning dispenser is required. In addition, the applied Photron SA3 fastcam resolution and frame rate were sufficient to determine these 'first' results of LBE within the framework of liquid impingement and aerosol formation. However, for further studies, a high-speed camera with higher resolution would be preferred to generate more detailed images. Also, the impacting would have been easier to describe if the high-speed camera was tilted or if the surface layer of the liquid and the dry solid surface came better into view. Lastly, regarding the non-spherical shape of the falling droplets, a MATLAB code or processing software which is able to correct for this deviation, may be required for further investigation.

6.5 Aerosol particle size distribution

Using a wide range aerosol detection system, the amount and size of aerosol particles, resulting from impinging LBE droplets, could be determined for the first time.

The PSD results of impingement on a liquid surface generates particles with diameters between 20 – 250 nm. The PSD peaks with $6.9.10^6$ particles/cm³ at 100 nm diameter. Impingement of LBE droplets on a dry solid surface generates aerosol particles up to 100 nm. A PSD maximum (6.10^6 particles/cm³) is located at 28 nm diameter. The shape of the PSD curve suggests that a significant amount of particles smaller than 20 nm will be present, but these cannot be recorded due to the lower particle size limit of the SMPS.

The results indicate that the PSD shifts to larger particle size bins during liquid impingent on a liquid surface as compared to impingement on a dry solid surface. However, both types of impingement lead to the formation of significant amounts of sub µm particles, which can pose a hazard as they are difficult to filter out and may mitigate deep into the human body.

To be able to make precise statements about the particle size distribution of LBE aerosols formed by liquid impingement, more PSD measurements are required. Additionally, a properly functioning dispenser is required so that precise well-known LBE droplets can be used as starting point.

7 LIST OF REFERENCES

[1] "Mission & vision | SCK CEN." https://www.sckcen.be/en/about-sck-cen/mission-vision (accessed Oct. 17, 2020).

[2] "Nuclear Energy Agency (NEA) - State-Of-the-Art Report (SOAR) on Nuclear Aerosols (NARSOAR)." https://www.oecd-nea.org/jcms/pl_18750 (accessed Oct. 17, 2020).

[3] A. J. Ghajar, "Entrainment," in *SpringerBriefs in Applied Sciences and Technology*, Springer, 2020, pp. 95–101.

[4] "NEA 2015 Edition Handbook on Lead-bismuth Eutectic Alloy and Lead Properties, Materials Compatibility, Thermal-hydraulics and Technologies," 2015. Accessed: Oct. 15, 2020. [Online]. Available: www.oecd.org/publishing/corrigenda.

[5] N. Chae, M. H. Lee, S. Choi, B. G. Park, and J. S. Song, "Aerodynamic diameter and radioactivity distributions of radioactive aerosols from activated metals cutting for nuclear power plant decommissioning," *Journal of Hazardous Materials*, vol. 369. Elsevier B.V., pp. 727–745, May 05, 2019, doi: 10.1016/j.jhazmat.2019.02.093.

[6] "NUREG/CR-7008, 'MELCOR Best Practices as Applied in the State-of-the-Art Reactor Consequence Analyses (SOARCA) Project'." Accessed: Nov. 22, 2020. [Online]. Available: http://www.nrc.gov/reading-rm.html.

[7] D. A. Powers, B. Clément, R. Denning, S. Ohno, and R. Zeyen, "Advanced Sodium Fast Reactor Accident Source Terms: Research Needs," 2010. Accessed: Nov. 22, 2020. [Online]. Available: http://www.ntis.gov/help/ordermethods.asp?loc=7-4-0#online.

[8] S. M. Goldberg and R. Rosner, "Nuclear Reactors: Generation to Generation."

[9] "Infrastructure | SCK CEN." https://www.sckcen.be/en/about-sck-cen/corporate-information/infrastructure (accessed Nov. 13, 2020).

[10] "GIF Portal - Technology Roadmap." https://www.gen-4.org/gif/jcms/c_40481/technology-roadmap (accessed Nov. 16, 2020).

[11] H. Aït Abderrahim, P. Baeten, D. De Bruyn, and R. Fernandez, "MYRRHA - A multi-purpose fast spectrum research reactor," in *Energy Conversion and Management*, Nov. 2012, vol. 63, pp. 4–10, doi: 10.1016/j.enconman.2012.02.025.

[12] "MYRRHA | MYRRHA Project." https://myrrha.be/myrrha-project/ (accessed Oct. 15, 2020).

[13] "Nieuwe reactoren en splijtstoffen | SCK CEN." https://www.sckcen.be/nl/expertises/technologie/nieuwe-reactoren-en-splijtstoffen (accessed Nov. 12, 2020).

[14] P. K. Nema, "Application of accelerators for nuclear systems: Accelerator driven system (ADS)," in *Energy Procedia*, Jan. 2011, vol. 7, pp. 597–608, doi: 10.1016/j.egypro.2011.06.080.

[15] K. Gladinez, K. Rosseel, J. Lim, A. Marino, G. Heynderickx, and A. Aerts, "Nucleation and growth of lead oxide particles in liquid lead-bismuth eutectic," *Phys. Chem. Chem. Phys.*, vol. 19, no. 40, pp. 27593–27602, 2017, doi: 10.1039/c7cp05068b.

[16] K. H. Kim, E. Kabir, and S. Kabir, "A review on the human health impact of airborne particulate matter," *Environment International*, vol. 74. Elsevier Ltd, pp. 136–143, Jan. 01, 2015, doi: 10.1016/j.envint.2014.10.005.

[17] "Review of adult lead models evaluation of models for assessing human health risks associated with lead exposures at non-residential areas of superfund and other hazardous waste sites," 2001.

[18] C. Berna, A. Escrivá, J. L. Muñoz-Cobo, and L. E. Herranz, "Review of droplet entrainment in annular flow: Interfacial waves and onset of entrainment," *Progress in Nuclear Energy*, vol. 74.

Pergamon, pp. 14–43, Jul. 01, 2014, doi: 10.1016/j.pnucene.2014.01.018.

[19] "(2) (PDF) A New Empirical Correlation for Entrained Droplet Fraction Prediction in Co- current Gas–Liquid Annular Two-phase Flow in Large Diameter Pipes." https://www.researchgate.net/publication/283152968_A_New_Empirical_Correlation_for_Entrained_Droplet_Fraction_Prediction_in_Co-_current_Gas-Liquid_Annular_Two-phase_Flow_in_Large_Diameter_Pipes (accessed Nov. 23, 2020).

[20] X. Yu, H. Gu, W. Yin, and Q. Sun, "Surface of a Liquid Pool with an Aerosol," 2020, doi: 10.1155/2020/8829074.

[21] G. Charalampous and Y. Hardalupas, "Collisions of droplets on spherical particles," *Phys. Fluids*, vol. 29, p. 103305, 2017, doi: 10.1063/1.5005124.

[22] C. Josserand, S. Thoroddsen, C. Josserand, S. T. Drop, S. Annual, and F. Mechanics, "Drop Impact on a Solid Surface To cite this version : HAL Id : hal-01398138 Drop Impact on a Solid," vol. 48, no. 1, pp. 365–391, 2017, doi: 10.1146/)).

[23] M. Rein, "Phenomena of liquid drop impact on solid and liquid surfaces," *Fluid Dyn. Res.*, vol. 12, no. 2, pp. 61–93, Aug. 1993, doi: 10.1016/0169-5983(93)90106-K.

[24] H. Yang, M. Fan, A. Liu, and L. Dong, "General formulas for drag coefficient and settling velocity of sphere based on theoretical law," *Int. J. Min. Sci. Technol.*, vol. 25, no. 2, pp. 219–223, 2015, doi: 10.1016/j.ijmst.2015.02.009.

[25] E. S. R. Negeed, S. Hidaka, M. Kohno, and Y. Takata, "High speed camera investigation of the impingement of single water droplets on oxidized high temperature surfaces," *Int. J. Therm. Sci.*, vol. 63, pp. 1–14, Jan. 2013, doi: 10.1016/j.ijthermalsci.2012.07.014.

[26] H. Chen, M. Marengo, and A. Amirfazli, "Drop impact onto semi-infinite solid surfaces with different wettabilities," *Phys. Rev. Fluids*, vol. 4, no. 8, Aug. 2019, doi: 10.1103/PhysRevFluids.4.083601.

[27] S. Chandra and C. T. Avedisian, "On the collision of a droplet with a solid surface," *Proc. R. Soc. London. Ser. A Math. Phys. Sci.*, vol. 432, no. 1884, pp. 13–41, Jan. 1991, doi: 10.1098/rspa.1991.0002.

[28] B. Ching, M. W. Golay, and T. J. Johnson, "Droplet impacts upon liquid surfaces," *Science (80-.).*, vol. 226, no. 4674, pp. 535–537, 1984, doi: 10.1126/science.226.4674.535.

[29] F. Rodriguez and R. Mesler, "Some drops don't splash," *J. Colloid Interface Sci.*, vol. 106, no. 2, pp. 347–352, Aug. 1985, doi: 10.1016/S0021-9797(85)80008-4.

[30] D. Richard, C. Clanet, and D. Quéré, "Surface phenomena: Contact time of a bouncing drop," *Nature*, vol. 417, no. 6891, p. 811, 2002, doi: 10.1038/417811a.

[31] S. L. Manzello and J. C. Yang, "An experimental study of high Weber number impact of methoxy-nonafluorobutane C 4 F 9 OCH 3 (HFE-7100) and n-heptane droplets on a heated solid surface q." Accessed: Nov. 13, 2020. [Online]. Available: www.elsevier.com/locate/ijhmt.

[32] D. Richard, C. Clanet, and D. Quéré, "Surface phenomena: Contact time of a bouncing drop," *Nature*, vol. 417, no. 6891, p. 811, Jun. 2002, doi: 10.1038/417811a.

[33] K. Weber, A. Vogel, C. Fischer, G. van Haren, and T. Pohl, "Airborne measurements of the Eyjafjallajökull volcanic ash plume over northwestern Germany with a light aircraft and an optical particle counter: first results," in *Lidar Technologies, Techniques, and Measurements for Atmospheric Remote Sensing VI*, Oct. 2010, vol. 7832, p. 78320P, doi: 10.1117/12.869629.

[34] V. Sobolev, "SCK • CEN - BLG - 1014 MYRRHA ADS DATABASE : Part I . Thermophysical properties of molten lead-bismuth eutectic," no. May, 2014.

[35] C. Motzkus, F. Gensdarmes, and E. Géhin, "Parameter study of microdroplet formation by impact of millimetre-size droplets onto a liquid film," *J. Aerosol Sci.*, vol. 40, no. 8, pp. 680–

692, Aug. 2009, doi: 10.1016/j.jaerosci.2009.04.001.

[36] I. H. Torremans, “inleiding procestechnische berekeningen,” in *Inleiding procestechnische berekeningen*, Overberg: Delta Press, 2006, pp. 57–77.

[37] “ISO-K/ISO-F flange.” https://www.pfeiffer-vacuum.com/en/know-how/mechanical-components-in-vacuum/connections/detachable-flange-connections/iso-k-iso-f-flange/ (accessed Nov. 21, 2020).

[38] “determine exactly the dispensing fluid :: VERMES Microdispensing GmbH.” https://www.vermes.com/en/applications/ (accessed Oct. 18, 2020).

[39] “VTK-TR-BA-080e-B Quick Reference Guide Hot Melt Dispensing with MDS 3280 1,” pp. 1–20.

[40] “VERMES Microdispensing Additional Training Documents.”

[41] U. Manual, “Microdispensing System MDS 3280,” 2020.

[42] “High-Speed Piezoelectric Jet Valves: New Modular Dispensing Solutions - Power Transmission World.” http://www.powertransmissionworld.com/high-speed-piezoelectric-jet-valves-new-modular-dispensing-solutions/ (accessed Oct. 18, 2020).

[43] “The Appeal of Piezo Jet Valve Dispensing | 2020-01-09 | ASSEMBLY.” https://www.assemblymag.com/articles/95392-the-appeal-of-piezo-jet-valve-dispensing (accessed Oct. 18, 2020).

[44] “Introduction to Image Sensors | LUCID Vision Labs.” https://thinklucid.com/tech-briefs/understanding-digital-image-sensors/ (accessed Nov. 30, 2020).

[45] “How Does A Camera Work?” https://www.creativelive.com/photography-guides/how-does-a-camera-work (accessed Nov. 25, 2020).

[46] “(No Title).” https://www.highspeedimaging.com/media/photron_manuals/FASTCAM_SA3_HW_Manual.pdf (accessed Nov. 25, 2020).

[47] H. Z. Xing, Q. B. Zhang, C. H. Braithwaite, B. Pan, and J. Zhao, “High-Speed Photography and Digital Optical Measurement Techniques for Geomaterials: Fundamentals and Applications,” *Rock Mechanics and Rock Engineering*, vol. 50, no. 6. Springer-Verlag Wien, pp. 1611–1659, Jun. 01, 2017, doi: 10.1007/s00603-016-1164-0.

[48] Q. Xu, I. Peters, S. Wilken, E. Brown, and H. Jaeger, “Fast imaging technique to study drop impact dynamics of non-newtonian fluids,” *J. Vis. Exp.*, no. 85, p. 51249, Mar. 2014, doi: 10.3791/51249.

[49] “How High-speed Photography Works | HowStuffWorks.” https://electronics.howstuffworks.com/high-speed-photography.htm (accessed Nov. 25, 2020).

[50] “Factors to Consider When Purchasing a High-Speed Camera – Photron.” https://photron.com/factors-consider-purchasing-high-speed-camera/ (accessed Nov. 22, 2020).

[51] “5416-based.” https://www.grimm-aerosol.com/products-en/nano-particle-measurement/smps-c/5416-based/ (accessed Nov. 23, 2020).

[52] P. H. Ryan, S. Y. Son, C. Wolfe, J. Lockey, C. Brokamp, and G. Lemasters, “A field application of a personal sensor for ultrafine particle exposure in children,” 2015, doi: 10.1016/j.scitotenv.2014.11.061.

[53] P. Sizers, “Scanning Mobility Particle Sizer ™,” vol. 48, no. 4, pp. 239–253, 2007, [Online]. Available: http://www.tsi.com/uploadedFiles/_Site_Root/Products/Literature/Bibliography/SMPS_Emissions_SMPS_Bib.pdf.

[54] “Particle Detectors FUNDAMENTALS OF CONDENSATION PARTICLE COUNTERS (CPC) AND SCANNING MOBILITY PARTICLE SIZER™ (SMPS™) SPECTROMETERS.”

[55] “8.9: Characterization of Bionanoparticles by Electrospray-Differential Mobility Analysis - Chemistry LibreTexts.” https://chem.libretexts.org/Bookshelves/Analytical_Chemistry/Book%3A_Physical_Methods_in_Chemistry_and_Nano_Science_(Barron)/08%3A_Structure_at_the_Nano_Scale/8.09%3A_Characterization_of_Bionanoparticles_by_Electrospray-Differential_Mobility_Analysis (accessed Jan. 19, 2021).

[56] G. C. Roberts and A. Nenes, “A continuous-flow streamwise thermal-gradient CCN chamber for atmospheric measurements,” *Aerosol Sci. Technol.*, vol. 39, no. 3, pp. 206–221, Mar. 2005, doi: 10.1080/027868290913988.

[57] “Scanning Mobility Particle Sizer (Centre for Atmospheric Science - The University of Manchester).” http://www.cas.manchester.ac.uk/restools/instruments/aerosol/scanning/ (accessed Oct. 18, 2020).

[58] T. Olenius, T. Yli-Juuti, J. Elm, J. Kontkanen, and I. Riipinen, “New Particle Formation and Growth: Creating a New Atmospheric Phase Interface,” in *Physical Chemistry of Gas-Liquid Interfaces*, Elsevier, 2018, pp. 315–352.

[59] D. H. Brouwer, G. Lidén, C. Asbach, M. G. M. Berges, and M. van Tongeren, “Monitoring and Sampling Strategy for (Manufactured) Nano Objects, Agglomerates and Aggregates (NOAA): Potential Added Value of the NANODEVICE Project,” in *Handbook of Nanosafety: Measurement, Exposure and Toxicology*, Elsevier Inc., 2014, pp. 173–206.

[60] “CPC.” https://www.grimm-aerosol.com/products-en/nano-particle-measurement/cpc/ (accessed Nov. 22, 2020).

[61] “(2) (PDF) Formation, Ageing and Thermal Properties of Secondary Organic Aerosol.” https://www.researchgate.net/publication/275890364_Formation_Ageing_and_Thermal_Properties_of_Secondary_Organic_Aerosol/Figures?lo=1 (accessed Nov. 23, 2020).

[62] “Product data sheet Palas® Promo® 2000 Applications • Emission monitoring of installations • Control of grinding and classification processes • Monitoring of production processes in the food, pharmaceuticals and chemicals industries • Testing of complete fiplters, inertial and wet separators or electrostatic precipitators.” Accessed: Dec. 13, 2020. [Online]. Available: www.parteq.net.

[63] “Optical Particle Counter » Section 1.” https://aerosol.ees.ufl.edu/opc/section01.html (accessed Dec. 13, 2020).

[64] A. Walser, D. Sauer, A. Spanu, J. Gasteiger, and B. Weinzierl, “On the parametrization of optical particle counter response including instrument-induced broadening of size spectra and a self-consistent evaluation of calibration measurements,” *Atmos. Meas. Tech*, vol. 10, pp. 4341–4361, 2017, doi: 10.5194/amt-10-4341-2017.

[65] Skoog Douglas A., West Donald M., Holler James, and Crouch Stanley R., “Fundamentals of Analytical Chemistry - Douglas A. Skoog, Donald M. West, F. James Holler, Stanley R. Crouch - Google Boeken,” in *fundamentals of analytical chemistry* , Second., Simpson Chris, Kiselica Sandra, Landsberg Alicia, and Schwartz Berardy Rebecca, Eds. Mary Finch, 2014, pp. 92–115.